Ternary and Quaternary Aluminum Oxynitrides
–
TeQuAlON

Inauguraldissertation

zur
Erlangung der Würde einer Doktorin der Philosophie
vorgelegt der
Philosophisch-Naturwissenschaftlichen Fakultät
der Universität Basel
von

Maria Ruth Fischer
aus Stetten (AG), Schweiz

2019

Genehmigt von der Philosophisch-Naturwissenschaftlichen Fakultät
auf Antrag von:

Prof. Dr. Hans J. Hug
Prof. Dr. Ernst Meyer

Basel, den 23. April 2019

Prof. Dr. Martin Spiess, Dekan

Preface

This project has been carried out 2014-2019 at Empa, the Swiss Federal Laboratories for Materials Testing and Research in Dübendorf, at the Laboratory 203 for Nanoscale Materials Science, headed by Prof. Dr. Hans J. Hug.

Some analyses were carried out at other institutes and laboratories.
Rutherford Backscattering (RBS), Elastic Recoil Detection Analysis (ERDA) and Helium Elastic Recoil Detection (He-ERD) were performed at the Swiss Federal Institute of Technology in Zürich (ETHZ), at the Laboratory of Ion Beam Physics (LIP). The measurements and evaluations were supervised and mostly carried out by Max Döbeli and his team, while Maria Fischer assisted on several occasions.
Ab initio Density Functional Theory (*ai*DFT) calculations were performed by Dr. Daniele Scopece, Dr. Carlo A. Pignedoli and Dr. Daniele Passerone at the Empa Laboratory 205, nanotech@surfaces, headed by Prof. Dr. Roman Fasel.
Nanoindendation was performed by Maria Fischer at the Empa Laboratory 206 for Mechanics of Materials and Nanostructures in Thun, headed by Dr. Johann Michler.
Ellipsometry was performed by Dr. Erwin Hack at the Empa Laboratory 405, Transport at Nanoscale Interfaces, headed by Prof. Dr. Michel Calame.

The financial support for this project was provided by the Swiss National Science Foundation (SNF) (project Nr. 200021-150095), by the Competence Centre for Materials Science and Technology (CCMX) and by Empa.

Look deep into nature, and then you will understand everything better.
Albert Einstein (1879-1955)

Science is not only a disciple of reason but, also, one of romance and passion.
Stephen Hawking (1942-2018)

Abstract

Aluminum (silicon) oxynitride, Al-(Si-)O-N, is a material that can be fabricated as transparent, hard coatings applicable to protect objects against wear, impact and corrosion. In the project presented here, thin films of Al-(Si-)O-N were deposited by reactive unbalanced closed field direct current magnetron sputtering (R-UCFDC-MS) and investigated for their chemical, microstructural and mechanical properties.

The R-UCFDC-MS process applied for the deposition of Al-(Si-)O-N is a Physical Vapor Deposition (PVD) process that was conducted with elemental Al and Si targets and the reactive gases O_2 and N_2. Working with O_2 is not trivial due to the high reactivity of this gas. To maintain process control, the sputter setup used was therefore modified. Two separate gas inlets were installed for the two reactive gases, such that N_2 was introduced directly at the targets and O_2 remote from the latter at the substrate. This promoted nitration and avoided oxidation of the targets and allowed the stable and reproducible deposition of transparent Al-(Si-)O-N films with adjustable compositions. The O content in the films was varied through the O_2 flow fed into the process and the Si content was varied through the power applied to the Si target.

A number of analytical techniques were applied to assess the properties of the Al-(Si-)O-N coatings deposited typically onto Si(100) wafers and glass. The chemical compositions of the coatings were determined by Rutherford Backscattering Spectrometry (RBS), Elastic Recoil Detection Analysis (ERDA) and Helium Elastic Recoil Detection (He-ERD). Thin films of AlN, of Al-O-N containing up to 60% O and of Al-Si-O-N containing up to 65% O and 20% Si were obtained.
The micro- and nanostructure of the coatings were characterized by X-Ray Diffrac-

tion (XRD) to determine the crystallinity, by Transmission Electron Microscopy (TEM) and Scanning Electron Microscopy (SEM) for images of film cross sections and by X-Ray Photoelectron Spectroscopy (XPS) for information on chemical states of the coatings. Combining the results of these analytical methods led to the determination of a microstructural evolution with changing chemical composition in the films.
Al-O-N coatings in the regime 0-8% O were found to consist of a crystalline solid solution made up of (002) fiber textured wurtzite crystallites, into which O incorporates in anionic lattice positions substituting N. In this regime, the wurtzite crystal lattice was observed to shrink with increasing O content, which was attributed to V(Al) vacancies generated by extra e^- from O(N) replacements. Simultaneously, a decrease in the crystallite size (CS) was observed, as O hinders crystallite growth because its valence electron (e^-) configuration mismatches the crystalline structure of wurtzite. In the range 8-30%, Al-O-N coatings exhibit nanocomposite formation, during which the O-saturated wurtzite crystallites are progressively encapsulated in an amorphous Al_2O_3 matrix. While nanocomposites in the regime with 8-16% O maintain (002) wurtzite fiber texture, those in the regime with 16-30% O only have a preferred texture. With increasing O content, the crystalline fraction reduces with a concurrent CS reduction and the amorphous fraction increases. Al-O-N coatings with more than 30% O form an X-ray amorphous solid solution. An equivalent evolution has previously been found in the Al-Si-N system upon increasing Si content[121,122,123,124,125], driven also by an additional e^- from Si replacing Al[129]. Al-Si-O-N represents the quaternary combination of the two ternary systems Al-O-N and Al-Si-N and was found to exhibit a more complex structural evolution.

The performance of the coatings was assessed by determining the optical properties by ellipsometry, the hardness (HD) and Young's modulus (E) by nanoindentation and the residual stress state (σ) from curvatures of thin coated substrates. The adhesion of the films to the substrates during the tests was strong, such that delamination was never observed. It was found that the transparent Al-(Si-)O-N coatings exhibit a linear decrease of the refractive index n from 2.1 to 1.6 with increasing O content from 0 to 65% independent of the Si content. In the same

O content range, HD of the coatings decreases from 26 to 8 GPa and E from 330 to 150 GPa, and $|\sigma|$ remains below 1 GPa. Al-O-N coatings exhibit a dip in HD due to hydrogen (H) incorporation exclusively in the fiber textured nanocomposite regime containing 8-16% O.

The V(Al) vacancies found experimentally through the crystal lattice shrinkage in crystallites were supported by *ab initio* Density Functional Theory (*ai*DFT) calculations. In a supercell of 192 atoms, O(N) substitutions and V(Al) were positioned in different concentrations and configurations. The lattice parameters calculated upon these cell modifications are in good agreement with those measured experimentally.
The enthalpy H additionally obtained from *ai*DFT was combined with the entropy S obtained from a combinatorial calculation of the possible microstates to yield the Gibbs free energy G of the coatings. This result was complimented with high temperature experiments, for which Al-O-N films were equilibrated at temperatures up to 1600°C. It was found that coatings containing crystalline wurtzite solid solutions including O are metastable, forming because the conditions in a R-UCFDC-MS process are far from thermodynamic equilibrium.

The Al-(Si-)O-N coatings were tested in several protective and functional applications. It was found that the films protect substrates such as Si(100) and glass against influences such as weathering and force impact. Due to the variability of the refractive index n with the O content in the films, protective coatings with reduced interference coloration could be fabricated. Additionally, the films could be used as a transparent matrix for the inclusion of gold (Au) nanoparticles, which resulted in decorative red, purple and blue films.

Zusammenfassung

Aluminium-(Silizium-)Oxynitrid, Al-(Si-)O-N, ist ein Material, mit welchem sich transparente, harte Beschichtungen herstellen lassen. Diese eignen sich zum Schutz von Objekten gegen Abrieb, Krafteinwirkung und Korrosion. Im Zuge des hier präsentierten Projektes wurden dünne Filme aus Al-(Si-)O-N hergestellt durch einen reaktiven Sputter Prozess genannt "reactive unbalanced closed field direct current magnetron sputtering" (R-UCFDC-MS), und untersucht auf ihre chemischen, mikrostrukturellen und mechanischen Eigenschaften.

Das für die Deposition von Al-(Si-)O-N verwendete R-UCFDC-MS - Verfahren ist ein physikalischer Verdampfungsprozess (Physical Vapor Deposition (PVD) process), welcher mit elementaren Al und Si Tagets und den Reaktivgasen O_2 and N_2 durchgeführt wurde. Das Arbeiten mit O_2 ist wegen der hohen Reaktivität des Gases nicht trivial. Um Prozesskontrolle zu behalten, wurde das Sputter-Setup modifiziert. Für die beiden Reaktivgase wurden zwei separate Gas-Inlets installiert, sodass N_2 direkt an den Targets und O_2 entfernt von letzteren am Substrat einströmten. Dies förderte die Nitridierung und verhinderte die Oxidation der Targets und ermöglichte die stabile und reproduzierbare Deposition von transparenten Al-(Si-)O-N Filmen mit veränderbaren Zusammensetzungen. Der O-Gehalt in den Filmen wurde durch den O_2-Fluss in den Prozess und der Si-Gehalt durch die Energie auf dem Si-target variiert.

Eine Auswahl von analytischen Techniken wurde genutzt, um die Eigenschaften von typischerweise auf Si(100) und Glas abgeschiedenen Al-(Si-)O-N Beschichtungen zu untersuchen. Die chemischen Kompositionen der Schichten wurden bestimmt mit Rutherford Backscattering Spectrometry (RBS), Elastic Recoil Detection Analysis (ERDA) und Helium Elastic Recoil Detection (He-ERD). Dünne

Filme aus AlN, aus Al-O-N mit bis zu 60% O und aus Al-Si-O-N mit bis zu 65% O und 20% Si wurden erhalten. Die Mikro- und Nanostruktur der Beschichtungen wurden charakterisiert mit X-Ray Diffraction (XRD) zur Bestimmung der Kristallinität, mit Transmission Electron Microscopy (TEM) und Scanning Electron Microscopy (SEM) für Bilder von Film-Querschnitten und mit X-Ray Photoelectron Spectroscopy (XPS) für Information zu den chemischen Zuständen in den Schichten.

Es wurde gefunden, dass Al-O-N Schichten mit 0-8% O aus einer kristallinen festen Lösung bestehen. Diese wird gebildet durch (002) Fiber-texturierte Wurtzit-Kristallite, in welche O durch die Substitution von N auf anionischen Gitterplätzen inkorporiert. Für dieses Regime wurde beobachtet, dass das Kristallgitter mit zunehmendem O-Gehalt schrumpft. Dies wurde zurückgeführt auf V(Al)-Vakanzen auf kationischen Gitterplätzen, generiert durch zusätzliche e^- von O(N)-Substitutionen. Gleichzeitig wurde eine Abnahme der Kristallitgrösse (crystallite size, CS) mit zunehmendem O-Gehalt beobachtet, da O das Kristallitwachstum stört, weil seine Valenzelektronenkonfiguration nicht mit der kristallinen Struktur von Wurtzit übereinpasst. Im Regime mit 8-30% O weisen Al-O-N Schichten die Bildung von Nanokompositen auf, in welchen die O-gesättigten Wurtzitkristallite progressiv von einer amorphen Al_2O_3 Matrix eingekapselt werden. Während Nanokomposite mit 8-16% O (002) Wurtzit-Fiber-Textur behalten, haben solche mit 16-30% O lediglich eine Vorzugsorientierung. Mit zunehmendem O-Gehalt reduziert sich die kristalline Fraktion mit einhergehender Kistallitgrössenreduktion, und die amorphe Fraktion nimmt zu. Al-O-N Beschichtungen mit mehr als 30% O bestehen aus einer röntgenstrahl-amorphen festen Lösung.
Eine ähnliche Evolution wurde zuvor für das Al-Si-N - System mit zunehmendem Si-Gehalt gefunden[121,122,123,124,125], ebenfalls erzeugt durch zusätzliche e^- von Si, welches Al ersetzt[129]. Al-Si-O-N stellt die quaternäre Kombination von den beiden ternären Systemen dar, und weist eine komplexere strukturelle Evolution auf.

Die Leistungsfähigkeit der Beschichtungen wurde beurteilt durch die Bestimmung der optischen Eingenschaften mit Ellipsometrie, der Härte (HD) und des Young's modulus (E) mit Nanoindentation und des Stresszustandes (σ) über die

Krümmung von beschichteten dünnen Substraten. Die Adhäsion der Filme zu den Substraten während der Tests war stark, sodass Delamination nie beobachtet wurde. Es wurde gefunden, dass transparente Al-(Si-)O-N Schichten eine lineare Abnahme des Brechungsindexes n von 2.1 zu 1.6 mit zunehmenden O-Gehalt von 0 bis 65% und unabhängig vom Si-Gehalt aufweisen. Im selben Bereich des O-Gehalts nehmen HD von 26 zu 8 GPa und E von 330 zu 150 GPa ab, und $|\sigma|$ bleibt unter 1 GPa. Al-O-N Schichten mit 8-16% O haben eine Senkung in HD, erzeugt durch die Inkorporation von Wasserstoff (H) ausschliesslich in Fiber-texturierten Nanokompositen.

Die im schrumpfenden Kristallgitter experimentell gefundenen V(Al)-Vakanzen wurden untermauert durch Rechnungen mit *ab initio* Dichtefunktionaltheorie (*ai*DFT). In einer Superzelle von 192 Atomen wurden O(N)-Substitutionen und V(Al) in verschiedenen Konzentrationen und Konfigurationen positioniert. Die nach diesen Modifikationen berechneten Gitterkonstanten stimmen gut mit den experimentell gemessenen Daten überein.
Die zusätzlich aus den *ai*DFT-Rechnungen resultiertende Enthalpie H wurde kombiniert mit der Entropie S, welche durch die kominatorische Berechnung der möglichen Mikrozustände abgeschätzt wurde. Dies ergab die Gibbs Freie Energie G in den Schichten. Dieses Resultat wurde ergänzt mit Hochtemperatur-Experimenten, für welche Al-O-N Filme bei Temperaturen von bis zu 1600°C equilibriert wurden. Es wurde gefunden, dass Schichten mit kristallinen festen Lösungen aus Wurtzit metastabil sind und sich bilden, weil die Bedingungen in einem R-UCFDC-MS Prozess weit weg vom thermodynamischen Gleichgewicht ablaufen.

Die Al-(Si-)O-N Beschichtungn wurden in mehreren protektiven und funktionellen Anwendungen getestet. Es stellte sich heraus, dass die Filme Substrate wie Si(100) und Glas gegen Einwirkungen wie Witterung und Kraftstösse schützen. Dank der Variabilität des Refraktionsindexes n mit dem O-Gehalt der Filme konnten Schutzschichten mit reduzierter Interferenz-Färbung hergestellt werden. Zusätzlich liessen sich die Filme als transparente Matrix zum Einschluss von Nanopartikeln aus Gold (Au) verwenden, was zu dekorativen roten, violetten und blauen Schichten führte.

Contents

1 Introduction

1.1 Coatings - omnipresent in our world

Coatings are, and have always been, a widely applied concept - in the modern world as well as in nature. Fruits consist of pulp sheathed by skin, and their seeds are built the same way. The trunk of a tree is surrounded by bark and so are its roots. Conifers build a waxy coating on their needles to regulate water evaporation, and lotus flowers produce a superhydrophobic polytetrafluoroethylene (PTFE) film that renders the lotus leaves self-cleaning[7].
In the copper, bronze and iron ages, people learned to mine and process metals. In contrast to formerly used brittle and bulky stone, metals could be processed and shaped flexibly. This allowed the first artfully produced coatings. Metal sheets could be formed and used to overlay objects, and yet more sophisticated coating techniques like gilding were invented[43]. The application of precious gold (Au) made it crucial to use amounts as tiny as possible per area, which meant the emergence of thin coatings. Au beating was skillfully optimized, so that Au sheets of only 300 nm thickness were already produced by Egyptians 5000 years ago[114]. Objects coated with these sheets were both protected and ornamented.
During the millennia that have since passed, the bulk materials used to produce objects as well as the techniques to form them have been developed and explored widely. Different metals have been combined to alloys and intermetallic phases, and non-metals have been added to create compounds with novel properties and functions. Oxidizing metals to form oxides, nitrides and carbides has lead to a variety of ceramic materials. Molding and casting have been complemented with shaping techniques such as Computerized Numerical Control (CNC) cutting and additive manufacturing through 3D printing.
The development of coatings has allowed advantageous bulk properties, such as

low price or low weight, to be combined with desirable functional surface properties such as high hardness, oxidation resistance, as well as low friction and wear. A prominent example that illustrates the importance and the widespread use of coatings is found in the automotive industry. Hard and wear resistant coatings, *e.g.* based on diamond-like carbon (DLC), are applied in fuel delivery and engine components[63]. The tools used in the vehicle production process are also often coated, *e.g.* by superhard titanium nitride (TiN), to protect them against wear and overheating[191], and to have a sustainable precision during high-throughput machining. In addition to functional improvements, coatings provide decoration. The car finish, for example, protects the steel framework against corrosion and simultaneously embellishes the car with color and gloss. Polymer coatings on car windows block UV light and tint the glass in variable shades. Chromium (Cr) coatings are used on plastics instead of bulk metal parts to reduce the car weight, and to decorate interior parts with a metallic look[85].

Galvanizing and other electrochemical wet processes, dip coating into melts and solutions, spraying and evaporation techniques are now used as a matter of routine[54] to fabricate coatings. Evaporations, distinguishable into chemical (Chemical Vapor Deposition, CVD) and physical (Physical Vapor Deposition, PVD) procedures, allow the advantage of ultrathin films down to (sub-)atomic monolayers to be realized.

For this thesis, the PVD method "Reactive Unbalanced Closed Field Direct Current Magnetron Sputtering" (R-UCFDC-MS) was applied to fabricate transparent thin films of ternary aluminum oxynitride (Al-O-N) and quaternary aluminum silicon oxynitride (Al-Si-O-N) (designated as Al-(Si-)O-N in further sections). R-UCFDC-MS has the advantage that metallic starting materials, also called "targets", can be used, while oxygen (O) and nitrogen (N) can be added in arbitrary amounts through the reactive gases O_2 and N_2. A wide stoichiometric range within the material systems can thus be assessed. The chemical and physical characteristics of the thin films vary through the stoichiometry and become tunable. The distinctive properties that thin films of Al-(Si-)O-N can provide are hardness and transparency. Coatings in the Al-(Si-)O-N system exhibit hardness (HD) values higher than sapphire (α-Al_2O_3). This renders them optimal candidates for protective coatings, particularly in applications, in which transparency is crucial.

1.2 The "Reactive Unbalanced Closed Field Direct Current Magnetron Sputtering" deposition process broken down

Sputter deposition is a PVD process that was first discussed 200 years ago[55]. Numerous books[19,182,117], reviews and articles[139,31] describe the process in all its variants and with its typical phenomena such as collision cascades and hystereses. Here, a short overview is given, along with some specifications of the sputter device used and the processes applied for the work discussed in this thesis.

The deposition chamber, an AJA ATC 1500 F (AJA International, Inc., Scituate MA, USA) is cylindrical, with an inner volume of approximately 35 l. Fig. 1.1 shows the system. Solid stainless steel walls, glass view ports and a turbo pump provide the vacuum that is needed to generate the plasma for a sputter deposition process. Four guns (visible in the inset on the bottom right of fig. 1.1), each of which can be equipped with a round target of 5 cm in diameter, are installed at the chamber bottom. The targets deliver the starting material for the coating procedure. Almost any vacuum compatible, solid substance can be used; relevant for this work were mainly Al and Si and occasionally Au. A chimney is built up on every gun. This

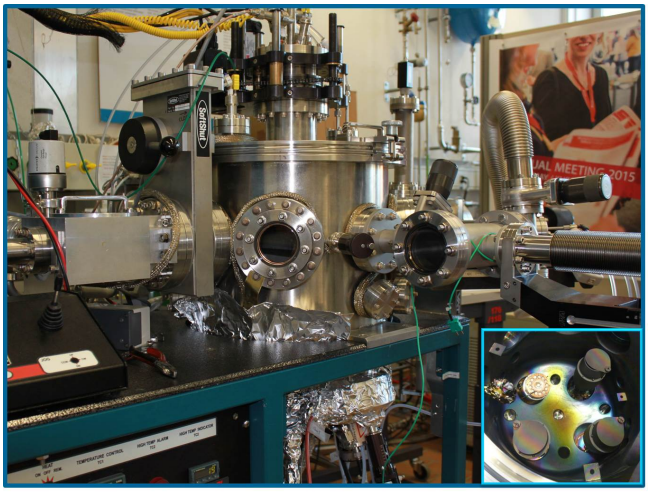

Figure 1.1: Photographs of the deposition chamber used. Large: Side view with main chamber in the middle, load locks to the left and to the right, electronic connections for substrate holder and heater on top and guns and their wiring at the bottom. Small inset: Top view onto the open chamber. The guns are under maintenance and tilted upright. Three have their chimneys mounted; one is exposed and shows the magnetic array installed under each target.

acts as the grounded electrode, channels the material flux and is topped by a shutter that can stop the flux of sputtered material from reaching the substrate while the gun is operated. If the shutter is open, material is eroded from the targets inside the guns and resublimates on substrates to be coated. In the case of the deposition chamber used in this project, the sputtering direction is bottom-up; *i.e.* the substrates are clamped onto a holder and hang down from the chamber lid. The substrates can be heated from behind through radiation from halogen lamps. The guns can be tilted and arranged confocally, so that they point towards the substrates and contribute to the material flux towards them. Underneath the targets, a ring of magnets with a center of opposite magnetization is installed, which is the reason that the entity of the gun is called a "magnetron". In fig. 1.1, the magnets are exposed on one gun shown in the top view.

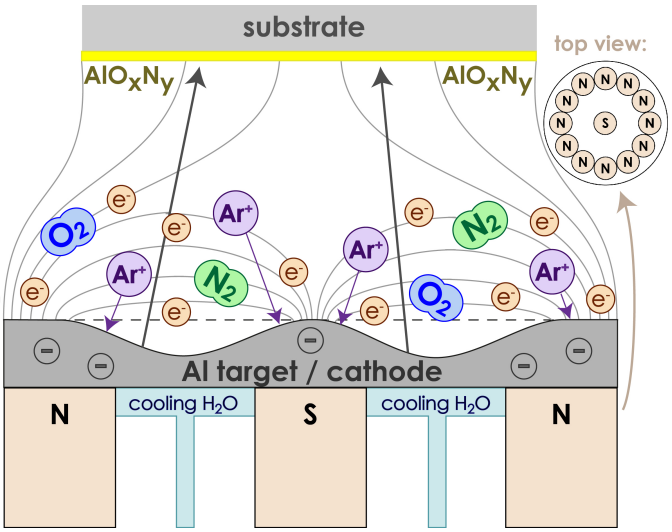

Figure 1.2: Schematic cross-sectional view of an unbalanced magnetron under discharge. A plasma with its typical components of ions and electrons (e^-) floats above the target. Magnetic field lines connect the outer to the central magnets, as they are of opposite polarization, and extend towards the substrate. A top view on the magnet array underneath the Al target is inset in the top right corner. Initially the target surface is flat (as indicated by a dashed line). After prolonged sputtering the material removed from the target causes a ring-like depression in the target, the so-called racetrack.

Fig. 1.2 shows the schematic buildup of one gun in action and its magnetic

array in top view (top right). The magnets in the outer ring are oriented with their north pole (N) towards the top of the gun, while the magnet in the center is contrariwise oriented with its south pole (S) upwards. The outer ring consists of several magnets, while the center consists of only one of equal strength as each of the outer ones. Therefore, this arrangement is called "unbalanced", and the magnetic field extends further into the outside space. Close to the target, the magnets generate a doughnut shaped magnetic field, which is able to confine electrons (e^-) close to the gun. This allows a lower sputter pressure of typically $\leq$1 Pa compared to processes conducted without magnets ($\geq$4 Pa)[182,p.52], as well as a higher sputter and thus deposition rate. A lower pressure is beneficial, since the free path that sputtered particles can fly without collision is larger. It is thus less probable that they are diverted and arrive at the substrate with more energy. If two guns are used confocally, they are often chosen to be of opposite magnetization, *i.e.* north polarization on the ring and south polarization in the center on one gun and vice versa on the other. In this way, the magnetic fields of the two guns can couple to a "closed field" and form a plasma arch extending towards the substrate. This increases the material flux and the bombardment of the film growing on the substrate with energetic particles, which can be beneficial for stress control and film quality[172]. The deposition process is initiated by introducing a small flow of an inert process gas, *e.g.* argon (Ar), and by applying a negative "direct current" voltage to the guns. This ignites a plasma, as Ar atoms are transformed to Ar ions (Ar^+; mostly singly, occasionally multiply charged) and free e^-. The latter are partially captured by the magnetic field near the target and then contribute to a sustained ionization process which enhances the plasma density. The positive ions are accelerated towards the targets due to the negative target potential. Upon impinging, the Ar^+ induce a collision cascade. Target material particles such as atoms, ions, molecules or clusters, and secondary e^- are ejected. Additional e^- are released due to collisions between particles. Some of these e^- in turn ionize further gas atoms, leading to an increased plasma density until the setpoint of the electrical power of the magnetron power supply is reached. With this a constant (target) particle flux towards the substrate is obtained. The sputter process used for this thesis was conducted in reactive mode to generate transparent oxynitrides. In addition to inert Ar, the reactive gases O_2 and N_2 were fed into the chamber.

Reactive sputtering is more complex than the non-reactive process, as discussed in specific literature[32,31,9,157,159,156]. More details on the control of the reactive sputtering processes used for the deposition of the thin film systems studied in this thesis are given in chapter 2.

1.3 Al-(Si-)O-N: A material system for transparent hard coatings

The four elements Al, Si, O and N can be combined in various ways in coatings. Al, a main group III metal, and Si, a main group IV semi-metal, both exist *per se* or as an Al-Si alloy in the solid state under standard conditions. O_2 and N_2, on the other hand, are gaseous, and will only reside stably in a solid if they are chemically bound to elements of it. Reactions between these solid and gaseous components happen readily, if they are exothermic and lead to thermodynamically stable compounds. Both Al and Si react with O_2 under atmospheric conditions with Al being more reactive than Si. This is the reason why Al foil is intrinsically covered with an inert layer of Al_2O_3 and can be used to wrap and protect comestibles. Si constitutes around $\frac{1}{4}$ of the earth crust as SiO_2 in the form of sand and granite. Reactions between Al or Si and N_2, on the other hand, do not take place spontaneously in the atmosphere. The triple bond in N_2 renders it an inert molecule, so that a higher activation energy is needed to dissociate the two N atoms and render them accessible for the reactants Al and Si. The plasma in R-UCFDC-MS provides this energy, and nitrides can be deposited although they are rarely found in nature.

The focus of this thesis is on transparent and hard coatings. In the Al-(Si-)O-N system, transparency requires that all Al and/or Si is fully oxidized and/or nitrided[14]. This defines the stoichiometry of these coatings as described in section 1.3.4. In the field of ceramic thin films, it became established to name such maximally oxidized/nitrided films as "stoichiometric" (while in general, "stoichiometry" simply signifies the given ratio of elements in a compound). Since Al and Si exist as solid, un-oxidized metals, "substoichiometric" films can in principle be fabricated by a sputtering process[13,14,15]. Such substoichiometric films are not fully transparent because of their metallic fractions and are not addressed in this

thesis, but have been investigated in other studies[13,14,15]. As O and N exist in the gaseous molecular forms O_2 and N_2 under standard conditions and typically are fully reacted in solids, "overstoichiometric" compositions are thermodynamically instable and only form in rare cases[136].
Amongst stoichiometric films, various compositions can be fabricated from Al, Si, O and N: Binary Al_2O_3, AlN, SiO_2 and Si_3N_4 exist in these fixed stoichiometries, while the fully stoichiometric ternary film compositions Al-Si-N, Al-O-N, Al-Si-O and Si-O-N with arbitrary Al/Si and O/N ratios can also be fabricated. Their variable composition is denoted with "-" between elements in order to distinguish them from absolute chemical compositions. In addition, the quaternary combination Al-Si-O-N can be fabricated.

This thesis is devoted to ternary Al-O-N and quaternary Al-Si-O-N. In order to explore the mechanisms governing Al-O-N film properties, the evolution of the latter with increasing concentrations of O added to binary AlN, until obtaining pure binary Al_2O_3, is studied. Similar work has already been done by our group for the Al-Si-N system, in which the Si content was increased[122,121,123,124,125]. The new results obtained on the Al-O-N system in this thesis are related to our older studies on the Al-Si-N system, and finally used in a quasi-binary approach to obtain a deeper understanding of the quaternary Al-Si-O-N system. Fig. 1.3 summarizes possible compounds and relates them to binary systems. Systems studied in this theses are highlighted as bold.

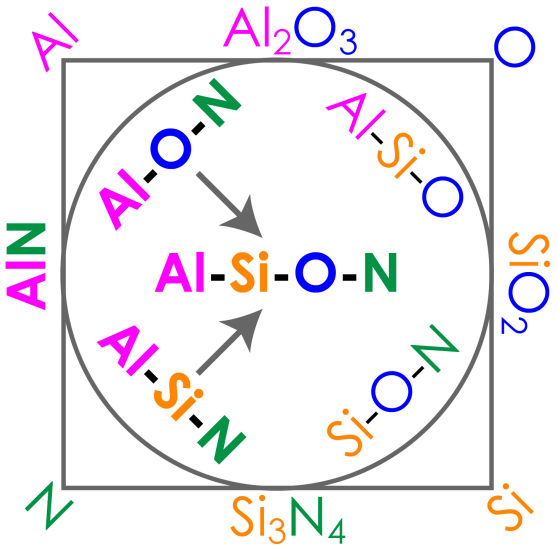

Figure 1.3: Elements involved in Al-(Si-)O-N and the feasible binary, ternary and quaternary stoichiometric combinations. The materials most relevant for this thesis are emphasized as bold.

1.3.1 The relevant binary and ternary systems

For Al-O-N, the relevant binary compositions are AlN and Al_2O_3. Commonalities for all materials discussed in this section are that they are colorless, transparent and electrically insulating. **AlN** exhibits a high hardness (HD) of around 23 GPa (value found for AlN films deposited for this thesis as well as reported in some literature[122,109,81]; other literature values scatter from 12 GPa[66] to 20 GPa[105]). Its stable state under standard conditions is the crystalline wurtzite structure (w-AlN). For a broad range of synthesis conditions, including those applied for this thesis, this phase is adopted. Wurzite belongs to the hexagonal crystal system and has the peculiarity that it is non-centrosymmetric. This renders the material piezoelectric, a manifoldly useful quality for *e.g.* SAW (surface acoustic wave) filters for mobile phone applications, spark generators or mechanical force sensors. The most stable form of $\mathbf{Al_2O_3}$ under atmospheric conditions is α-Al_2O_3, also known as corundum or sapphire, which has a HD of 21-23 GPa[66,150]. α-Al_2O_3 belongs to the trigonal crystal system. In synthesis, it is difficult to obtain Al_2O_3 in its α-modification, as well as any other crystalline phase it can adopt. Harsh conditions such as high temperatures or pressures are needed to provide the activation energy to bring the system to this thermodynamic minimum. Most procedures, also R-UCFDC-MS used in this thesis, yield amorphous Al_2O_3 (a-Al_2O_3). Amorphous Al_2O_3 films are reported to be softer than sapphire with a HD of 11.5 GPa[81] (films deposited in this project and close to the stoichiometry of Al_2O_3 had similar values of around 13 GPa). $\mathbf{SiO_2}$ (HD 6-8 GPa[8,23]) exists in crystalline as well as amorphous solids. Quartz is the modification belonging to the trigonal crystal system and occurring in large quantities on earth in granite. As an amorphous solid, SiO_2 constitutes the major component in sand and glass. $\mathbf{Si_3N_4}$ (HD 17 GPa[66]) exists in a number of crystalline phases, *e.g.* α-, β- and γ-Si_3N_4. However, it readily adopts an amorphous state (a-Si_3N_4). Both SiO_2 and Si_3N_4 are deposited amorphously under the R-UCFDC-MS conditions used here.

Al-O-N is the ternary system characterized in this thesis. There is little prior work on this system and most of that addresses the bulk materials[188]. The first work addressing the phase diagram was reported in 1964[89]. Based on this, Al-O-N with the expected density and transparency could be fabricated[104,78]. Several

crystalline phases, amongst them cubic spinels, were found[162,163,164]. Thin films of Al-O-N thus represent an attractive research field. While a limited number of prior work exists[29,70,60,22,71,187,154,48,73,17,180], only a small number of those describe Al-O-N deposited by R-UCFDC-MS. Quaternary **Al-Si-O-N** is rarely described in literature[49,101], either as a bulk material or as thin film.

1.3.2 The anatomy of thin films

The anatomy of thin films is defined by their physicochemical composition and microstructure as shown in fig. 1.4.

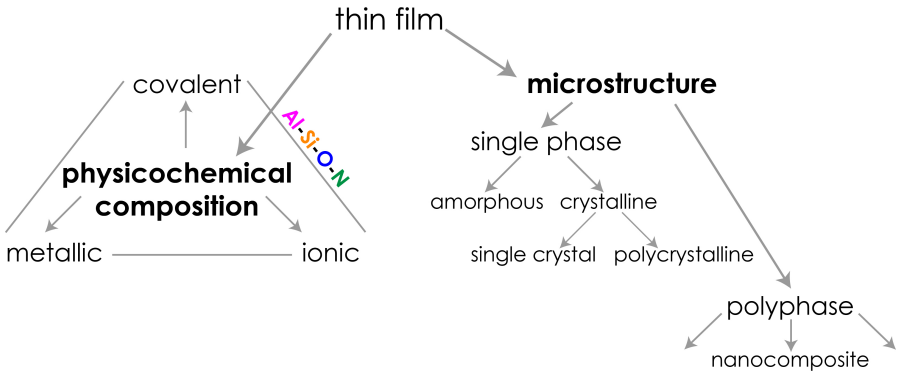

Figure 1.4: Schematics of the relevant parameters defining the anatomy of thin films.

The physicochemical composition

The physicochemical composition can be classified by the nature of the interatomic bonds present in a thin film. Materials of the first group form through **metallic** bonds. Valence e^- of their constituent elements form a delocalized "e^- gas" around the atom cores (nuclei plus core e^-), rendering such materials electrically conductive. As the e^- are not localized in orbitals with a well-defined geometry and a significantly lowered energetic state, typical metallic bonds are of rather low energy, *e.g.* 2.1 eV for Cu-Cu and 2.3 eV for Au-Au[99], which provides a rather low hardness to metallic materials. In a metallic crystal lattice, the positions are

not distinguished into cationic and anionic sub-lattices, which means that a metal atom can move to any directly neighboring lattice position. This flexibility in atom mobility in combination with the low bond energies renders metals ductile. Metallic and alloy films belong to this group.

A second group can be defined by systems forming ionic bonds. These occur between e^- donors of low electronegativity (χ) and acceptors of high χ. When $\Delta\chi$ between e^- donors and acceptors is high, typically >2.0[183,p.233,251–279], a transfer of one or several e^- from the former to the latter occurs. As the transferred e^- are localized and energetically stabilized in orbitals of the acceptor, the material is electrically insulating and often named a "wide band gap semiconductor". For a sufficiciently wide band gaps these materials are transparent, and for smaller bandgaps a coloration is observed. Between the cationic donor and the anionic acceptor, a chemical bond described by the electrostatic attraction forms. The energy of such a bond is high, *e.g.* 5.5 eV for Ca-F and 4.3 eV for Na-Cl[99]. Together with the high coordination numbers occurring in such salts, the high bonding energies render ionic materials energetically highly stable and thus hard. In contrast to a metallic crystal lattice, an ionic lattice is divided into cationic and anionic sub-lattices. A cation or anion can therefore not move to and reside in a neighboring position, as this would lead to a strong electrostatic repulsion. If such a dislocation takes place, however, *e.g.* due to an impact, the ionic lattice breaks apart. This is what renders ionic materials brittle. Films containing halogenides (fluorides, chlorides, bromides, and iodides) as well as oxides and sulfides belong in this group.

The third group of materials is characterized by covalent bonds. These occur when $\Delta\chi$ between two non-metallic, typically main-group elements, is <2.0[183,p.233,251–279]. The e^- are then not completely transferred from one species to the other, but the e^- from both bonding species are stabilized in a shared molecular orbital. The distribution of the charge between the bonding partners is classified as polar for $0.5< \Delta\chi <2.0$, where a clear distinction between e^- donor and acceptor still exists, or non-polar for two species with $\Delta\chi <0.5$, or symmetric for bonds between equal species. Between two species, molecular orbitals for single, double or triple bonds can form. As the e^- in these orbitals are energetically stabilized, such materials are usually insulating. The covalent bonds are typically of lower energy than ionic

ones, *e.g.* 3.6 eV for C-C and 3.3 eV for Si. As dislocations do not lead to strong electrostatic repulsion as in ionic substances, materials with covalent bonds are less brittle and are characterized by a high toughness. Ceramic nitride and polymer films belong in this group.

The categorization of specific materials according to these criteria is discussed extensively in literature[66,52,119,111,177,176,192], and material design aims at combining qualities of the three physicochemical material groups. Adding carbon (C) to alloys, for example, imparts a covalent component to metallic materials. An example of a material in which properties of all three physicochemical groups are combined is TiN with a 1:1 stoichiometry. Three Ti e^- are bonded to N in a mixed ionic-covalent system, while one e^- remains metallic. TiN has a very high HD up to 45 GPa[116], yet keeps electric and thermal conductivity and is of metallic, golden color[191].

The materials investigated in this project within the Al-Si-O-N system exhibit a mixed ionic-covalent character. Nitrides tend towards covalent bonding, whereas oxides tend to be ionic.

The microstructure

A thin film is a three dimensional object with large extension in the plane and a considerably smaller extension perpendicular to the film plane, typically in the range of a nanometer to a few micrometers. The physicochemical composition of the film-forming species as well as the growth conditions, *e.g.* the temperature or the energies of the film-forming particles, determine the film structure[167,6,128,4,127,172] (see also section 7.6).

Films, as shown in fig. 1.4, can either consist of a single phase or be polyphased. A film consisting of a single crystal can either be perfect or contain 1D, 2D or 3D defects. When 2D and 3D defects are of significant size, the crystalline film is split into separate crystal grains. As long as the misalignment of these grains with respect to each other is low and a coherency remains, this condition is termed "mosaicity", and when the misalignment is significant and the grains are clearly separated from each other by grain boundaries, the condition is categorized as polycrystallinity. When the single grains in a polycrystalline film maintain the

same orientation perpendicular to the plane, *i.e.* when they all point with the same crystal direction (xyz) towards the film surface, but loose their in-plane orientation, the resulting structure is named a "fiber texture". When the orientation perpendicular to the plane is also lost, a film with preferred orientation or random crystallite orientation results. Nanocomposites represent a particular case of polyphased material.

Nanocomposites

As the name implies, nanocomposite thin films consist of at least two different phases with nanometer-scale geometric extensions, for example crystallites with 5-100 nm diameter embedded in an amorphous grain boundary phase. In crystals of such small sizes, dislocations are energetically not favorable. This enhances the hardness of the grains, because dislocations cannot exist and consequently dislocation motion, and connected to it a grain deformation, does not occur. At the grain boundary, the matrix material acts like a glue connecting the hard grains. Due to the absence of dislocations inside the grains, nanocomposites can only deform via grain boundary sliding. If the matrix material is hard itself, and bonds strongly to the grains, grain boundary sliding is suppressed and the nanocomposite exhibits a hardness surpassing that of the crystallites and that of the grain boundary phase separately. In a nanocomposite coating, the latter can also act as a diffusion barrier increasing the oxidation resistance of the substrate.
The Al-(Si-)O-N films investigated for this project show a distinctive microstructural evolution, as will be described in section 3.4. Nanocomposites were obtained within a defined compositional region.

1.3.3 Techniques used to investigate the composition and structure of coatings

As discussed above, the chemical composition is one of key ingredients leading to specific material properties and thus needs to be analyzed with great precision. Here, Rutherford Backscattering Spectrometry (RBS) and Elastic Recoil Detection Analysis (ERDA) were used to determine the elemental composition and with that the film stoichiometry. In these techniques, the sample is bombarded by high energy ions of ^{4}He for RBS and of heavy ^{127}I for ERDA. These projectile ions interact elastically with the sample nuclei. In RBS, the energy of the back-scattered beam He particles are analyzed, whereas in ERDA, forward recoiling sample atoms are analyzed. This allows the determination of the atomic numbers of the species in a coating as well as their concentration and their depth distribution inside the film. While RBS has a higher accuracy when determining stoichiometries, ERDA has a higher sensitivity for light elements. Thus the e^- donor(s) in the Al-(Si-)O-N films, *i.e.* Al and Si, and the major e^- acceptor, *i.e.* O or N, were measured by RBS; the minor e^- acceptor was refined via O/N ratio measured by ERDA. All RBS/ERDA measurements and evaluations were performed at the Laboratory of Ion Beam Physics (LIP) at the Swiss Federal Institute of Technology, Zürich (ETHZ)[82,112,35,76]. The combination of these two techniques was chosen for the compositional analysis in this project for two reasons. Firstly, RBS/ERDA provide a high accuracy in the obtained stoichiometries. Secondly, the depth profiling allows the evaluation of the bulk of a film excluding the film surface, which often oxidizes post-depositionally upon exposure to atmosphere. RBS/ERDA are thus superior in determining chemical compositions compared to other techniques such as X-Ray Photoelectron Spectroscopy (XPS), which has a lower accuracy for stoichiometries and can only probe the surface of a film down to a few nanometers, typically $\leq$20 nm. To assess the bulk of a film by XPS, the oxidized surface has to be sputter-removed prior to analysis. Sputtering may however preferentially remove one element in respect such that the composition changed by the sputter process itself is analyzed. Moreover, the reactive sample surface may re-oxidize even in the reasonably good vacuum of the XPS chamber. XPS is thus not ideal for a compositional analysis of Al-(Si-)O-N films, and particularly not well suited

for a determination of the O content. XPS was however used to probe the chemical states of the species in the films through the binding energies (BE) of core e^-. Depending on the bonding interactions in a material, the species involved in the bonds are partially oxidized or reduced which rises or lowers, respectively, the BE of their core e^-. XPS determines these BEs by irradiating a sample with X-rays to excite core e^- and by measuring the energies of the photoelectrons (photo e^-) emitted by the relaxation of the core e^- [178,181,147,134,146].

With the chemical composition and the bonding states of the film measured, one part of the anatomy of the films (fig. 1.4) is determined. Now the microstructure and morphology of the samples need to be studied. Crystallinity was assessed by X-Ray Diffraction (XRD). In this technique, the e^- shells of the species in a sample interact elastically with X-rays. For the case of a crystalline sample, the X-rays are diffracted under well-defined angles defined by the Bragg condition. With θ being the angle between X-ray beam and sample and 2θ between beam and detector, symmetric θ-2θ scans provide information about crystal planes parallel to the sample surface and thus orthogonal to the film growth direction (z). While the position of the peaks in diffractograms relates to the distance between the crystal planes, a line profile analysis (LPA) according to Birkholz[11 p.85–101] is used to obtain the c-axis lattice parameter, the crystallite size (CS) and the microstrain (MS) of crystallites in coatings. The full width at half maximum (FWHM) of rocking curves (RCs) on the peaks in θ-2θ diffractograms yields a measure for the angular distribution of crystallite plane tilts away from z. Pole figures (PFs) scan for a specific diffraction signal while continuously tilting a sample by the angle ψ and rotating it by ϕ around its central surface normal. This reveals the texture of a coating. In-plane θ-2θ scans provide information on crystal planes perpendicular to the sample surface, and asymmetric θ-2θ scans explore crystal planes aslope to the latter. High temperature *in situ* X-Ray Diffraction (HT*is*XRD) tests the stability and inertness of the crystalline structure of films upon heating[102,11,141,87,88,28,83].

The cross sectional structure of the coatings was investigated by electron microscopy. Scanning Electron Microscopy (SEM) was used to image cross-sections on film fractures, and Transmission Electron Microscopy (TEM) was applied to take bright field (BF) and dark field (DF) images, electron diffraction (ED) patterns and high resolution (HR) images on 20-30 nm thin regions of a cross sectional

wedge.
An important quality of transparent thin films is their visual appearance. The Al-(Si-)O-N coatings were thus checked by eye, in some cases magnified through an optical microscope, for artifacts such as inclusions, tarnishings or colorations and cracks. For a coating in which cracks occurred, a typical crack was imaged by a Gallium Focused Ion Beam Scanning Electron Microscope (GaFIB-SEM). Further optical properties such as the refractive index (n) and the absorption coefficient (k) were determined by ellipsometry. This technique probes samples with an elliptically polarized beam of visible light and extracts n and k from amplitude changes and phase shifts detected in the reflected beam.
The Al-(Si-)O-N coatings exhibit a post-depositional residual stress (σ), which causes thin substrates to bend. σ was quantified by measuring the curvatures of bent samples and film thicknesses using a profilometer, and by feeding these values into the new Stoney equation[75].
Important properties of the Al-(Si-)O-N deposited in this project are the hardness (HD) and Young's Modulus (E), as these qualities determine the applicability of the material in protective coatings. HD and E of the Al-(Si-)O-N films were assessed by nanoindentation, which presses a diamond tip into the film surface and records the indentation depth with changing loading force[118].
All details and measurement parameters applied for this work are given in appendix A in chapter 8.

1.3.4 Stoichiometry in Al-(Si-)O-N

Al-(Si-)O-N films are transparent when all Al and/or Si are fully oxidized and/or nitrided. Al and Si are (semi)metallic electropositive e^- donors, while O and N are electronegative e^- acceptors. While both the donation as well as the acceptance of e^- require energy, the subsequent interaction between donors and acceptors results in stabilized bonding orbitals when covalent bonds form and to electrostatic attraction in the case of ions, and thus a release of more energy than invested for e^- donation and acceptance. Because the Pauling electronegativities χ of the donors, χ_{Al}=1.5 and χ_{Si}=1.8, are 1.2-2.0 lower than those of the acceptors with χ_O=3.5 and χ_N=3.0, the bonding in Al-(Si-)O-N is of mixed ionic-covalent nature and the material forms a fully occupied valence and an empty conduction band. This provides transparency and electrical insulation.

All of the elements involved in Al-(Si-)O-N are main group elements. These strive to obtain "noble gas configuration", *i.e.* a valence shell filled with 8 e^-, s^2p^6, which is called the "octet rule". The number of bonding interactions each main group element participates in to fulfill the octet rule is referred to as "valency".
Al has the valence e^- configuration $3s^2p^1$ and thus a valency of 3 and 3 valence e^- to donate to acceptors . Si has the configuration $3s^2p^2$, meaning there are 4 valence e^- to donate. With O and N as bonding partners, neither Al nor Si with their low χ accept e^-, as this would require more energy than donating e^- to O and N which have a high χ. O has a valence e^- configuration of $2s^2p^4$, meaning that there are 6 valence e^-. Accepting 2 e^- required to fill the outer orbitals to achieve the configuration $2s^2p^6$ requires less energy than donating 6 e^-. This tendency to accept rather than donate e^- is also valid for N, which has a configuration of $2s^2p^3$ and thus can take up 3 more e^-.
Stoichiometric Al-(Si-)O-N therefore has a uniquely defined, non-transgressable element composition in which the amounts of two elements can be chosen freely and the other two are fixed functions of those. To determine the correct elemental composition, the e^- donated have to be balanced by those accepted. In the case of AlN, Al has 3 e^- to give and N can accept 3 e^-, hence the resulting stoichiometry is Al_1N_1. Stoichiometric coefficients of "1" are omitted, giving AlN.

To find the stoichiometry of Al-O-N, that of AlN can be used as the starting point. The addition of O requires the simultaneous reduction of N according to the following composition:

$$\mathrm{AlO}_b\mathrm{N}_{1-a} \tag{1.1}$$

For the e^- balance, the following has to hold:

$$\underbrace{3*1}_{\text{e}^-\text{donated by Al}} = \underbrace{2*b}_{\text{e}^-\text{accepted by O}} + \underbrace{3*(1-a)}_{\text{e}^-\text{accepted by N}} \tag{1.2}$$

Hence $b = 1.5a$, and the stoichiometry can be given as:

$$\mathrm{AlO}_{1.5a}\mathrm{N}_{1-a} \quad \text{or} \quad \mathrm{AlO}_{1.5(1-z)}\mathrm{N}_z \ , \tag{1.3}$$

where $1-a$ of the former has been substituted by z in the latter.

For stoichiometric quaternary Al-Si-O-N, the *Ansatz*

$$\mathrm{AlSi}_x\mathrm{O}_y\mathrm{N}_z \tag{1.4}$$

is used. The e^- balance for this is:

$$\underbrace{3*1}_{\text{e}^-\text{donated by Al}} + \underbrace{4*x}_{\text{e}^-\text{donated by Si}} = \underbrace{2*y}_{\text{e}^-\text{accepted by O}} + \underbrace{3*z}_{\text{e}^-\text{accepted by N}} \tag{1.5}$$

This allows the determination of y as a function of x and z:

$$\mathrm{AlSi}_x\mathrm{O}_{1.5+2x-1.5z}\mathrm{N}_z \tag{1.6}$$

The valencies of Al (3) and Si (4) limit the maximum value of z to:

$$z_{max} = 1 + \tfrac{4}{3}x \ . \tag{1.7}$$

If $z = z_{max}$, the O content $y = 1.5 + 2x - 1.5z$ becomes zero.

1.4 The structure of this thesis

This thesis is structured into eight chapters. Two of them give the basic background and context, *i.e.* the "Introduction" in chapter 1 and the "Conclusions and outlook" in chapter 6.

Chapter 2 is a verbatim copy of the paper by M. Fischer *et al.*, entitled "A setup for arc-free reactive DC sputter deposition of Al-O-N". It describes how the experimental sputter deposition system used in this project was be adapted to allow the deposition of oxynitrides. Starting with a conventional preparation chamber, hardware additions as well as process adaptions were implemented. This was necessary, as working with the reactive gas O_2 is significantly more demanding than working with N_2 alone and requires a greater degree of process control.
Chapter 3 is a verbatim copy of a manuscript by M. Fischer *et al.*, submitted, entitled "Understanding the microstructural evolution and mechanical properties of transparent Al-(Si-)(O-)N films". It describes the properties of the Al-(Si-)O-N thin films deposited with the methods discussed in chapter 2. Over 300 thin film deposition runs were performed, and various analytical techniques were applied to characterize the coatings. Finally, a model describing the evolution of the Al-O-N and Al-Si-N films with increasing O and Si content, respectively, could be established.

Chapter 4, "Al vacancies in Al-O-N investigated by *ab initio* Density Functional Theory", presents a model and supporting *ab initio* Density Functional Theory (*ai*DFT) calculations that explain the material evolution upon adding O/Si into coatings of crystalline wurtzite. Low O/Si contents can be incorporated into wurtzite in the form of a solid solution via two different kinds of substitution, both inducing a mismatch between the stoichiometry and the electronic structure of the crystal. The model shows how this imbalance can be resolved through vacancies in the Al sub-lattice. Subsequently, the thermodynamic stability of the coatings is assessed through the Gibbs free energy (G) by combining the enthalpy (H) and the entropy (S) of the films. The hypothesis that entropy stabilizes the solid solution phase in a certain concentration range is tested.

Chapter 5, "Applications", inquires the applicability of the hard, transparent Al-(Si-)O-N coatings for protective, optical and decorative purposes.

Chapter 7 and 8 comprise appendices containing additional experimental data on Al-(Si-)O-N and experimental details for this project.

2 A setup for arc-free reactive DC sputter deposition of Al-O-N

The text and figures of the following chapter are a verbatim copy of the paper published (online since 1st February 2019) in
Surface & Coatings Technology, 362: 220-224, 2019, doi: 10.1016/j.surfcoat.2019.01.082.

Authors

Maria Fischer[a,*], Mathis Trant[a], Kerstin Thorwarth[a], Jörg Patscheider[b,1], Hans Josef Hug[a,c]

[a] Empa, Swiss Federal Laboratories for Materials Science and Technology, Überlandstrasse 129, 8600 Dübendorf, Switzerland
[b] Evatec AG, Hauptstrasse 1a, 9477 Trübbach, Switzerland
[c] Department of Physics, University of Basel, Klingelbergstrasse 82, 4056 Basel, Switzerland
[1] Empa, Swiss Federal Laboratories for Materials Science and Technology, Überlandstrasse 129, 8600 Dübendorf, Switzerland (until 31.10.2017)
[*] Corresponding author.

Keywords
reactive sputtering, transparent hard coatings, thin films, aluminum oxynitride, Al-O-N

Abstract

Aluminum oxynitride (Al-O-N) is a material suitable for hard, transparent thin films. Its physical properties and structure can be adjusted through the O-to-N ratio.
Reactive Direct Current Magnetron Sputtering (R-DCMS) is a practical, widespread technique for the deposition of coatings. However, it proves to be challenging in the case of Al-O-N. The reason for this is the high reactivity of O_2. Poisoning of Al targets by O_2 causes formation of insulating oxide islands and consequently leads to target destruction and a failure of the deposition process.
Here we show that with two separate gas inlets for the two reactive gases, a good process stability can be achieved over the entire range of O-to-N ratios.

2.1 Introduction

Aluminum oxynitride (Al-O-N) is of high interest for transparent, insulating protective coatings. The highest transparency is obtained if no Al is left in its metallic state (fully reacted). In the binary case this can be achieved either by fabricating pure AlN or Al_2O_3 thin films. While sputter-deposited AlN films are polycrystalline with grains of wurtzite structure[13], the Al_2O_3 films remain amorphous for deposition temperatures below 500°C[115].
In the ternary Al-O-N system, physical properties such as the refraction index can be adjusted between the binary systems through the O-to-N ratio[29,80,81]. A higher O content also leads to a refinement of the grain size and finally to amorphization[128]. With the latter, diffusion processes along grain boundaries can be suppressed. This is for example useful, if the material is applied as the dielectric of a capacitor. It has been shown that for amorphous Al-O-N, leakage currents are substantially reduced, and a higher breakdown field is obtained compared to polycrystalline AlN[17]. Another application of Al-O-N are thin film coatings for oxidation protection. The amorphization obtained at a higher O content changes the stress of the coating on the substrate towards compressive[185] and substantially reduces the O_2 penetration through the thin film. Moreover, Al-O-N coatings with high O contents are inert towards further oxidation[71].

Reactive Direct Current Magnetron Sputtering (R-DCMS) has been successfully used for the deposition of AlN, but remained difficult to apply for Al_2O_3. The causes for this have been addressed previously[3,9,139,144,157,159]. R-DCMS for AlN or Al_2O_3 deposition is typically performed with Ar as inert process gas and N_2 or O_2 as reactive gas. While N_2 does not affect the stability of the sputter process, the addition of O_2 renders process control difficult because of its high reactivity with the target material. Consequently, the fabrication of oxide films requires more elaborate sputtering methods such as radiofrequency (RF) or pulsed direct current sputtering[157,159,139]. Maintaining a reasonable deposition rate requires control of the reactive gas partial pressure[157,159]. This is achievable by keeping a suitable mass spectrometer intensity[158] or plasma emission intensity[142,64] or the plasma impedance[3,174] constant. However, these methods require sophisticated and costly hardware. A different approach suitable for reactive DC sputter deposition of pure oxides was already described in the 1980s: The target was enclosed in a box to shield it from O_2. The latter was introduced close to the substrate[100,140,41].
Here, we report a new design of a DC magnetron sputtering system for the deposition of Al-O-N thin films that avoids the necessity to encase the substrate. Instead, two separate gas inlets were installed for the two reactive gases (separated inlets setup). N_2 was fed in adjacent to the target while O_2 was fed in near the substrate in order to promote target poisoning by N_2 and to prevent poisoning by O_2. This separated gas inlet configuration allows the deposition of Al-O-N in a stable and reproducible process without the need for expensive hardware and is implementable in any standard coating system. For comparison, sputter process stability was also studied for a more conventional gas inlet setup (combined inlet setup).

2.2 Experimental

This work was carried out in an AJA ATC 1500 F sputtering system (AJA International, Inc.) of cylindrical shape with a height of 33 cm and a diameter of 37 cm. The chamber is equipped with a TMU 261 turbo pump with a capacity of 210 l/s (Pfeiffer Vacuum). Further details on the chamber design and implemented modifications are described below (see section 2.3). R-DCMS deposition processes of Al-O-N were performed with two unbalanced magnetrons arranged in a closed field configuration about 12 cm below the substrates. The latter were heated to 200°C through radiation from lamps installed behind the substrate holder. Metallic Al targets of 5 cm diameter and 99.999% purity grade (Hauner Metallische Werkstoffe) were used. The power on the targets was kept constant at 200 W, resulting in a nominal power density of 10 Wcm^{-2}. Before each deposition process, the targets were cleaned to their metallic state by sputtering for 3 min in pure Ar introduced through a gas inlet at the chamber bottom (see fig. 2.1) with a flow of 16 sccm. This Ar flow was kept for all depositions to provide a constant process gas background.
With the separated gas inlet setup (see fig. 2.1b)), a poisoning step of 2 min with closed chimney shutters and 12 sccm N_2 through the N_2 gas inlet followed. This flow rate was sufficient to bring the targets into the fully AlN poisoned mode, as was checked recording the voltage in hysteresis experiments. The AlN coverage served to protected the target before admitting O_2 into the chamber.

During the subsequent 3 h film deposition process, the flow of 12 sccm N_2 at the targets was kept. 0-10 sccm of an O_2/N_2 mixture with O_2 contents of 1% or 10% were introduced to the substrate through the central gas inlet, which yielded a net O_2 flow up to 1 sccm. The total reactive gas flow at the target and the substrate was thus increased for processes with a higher O_2 flow. A gas mixture instead of pure O_2 was chosen at the central inlet in order to keep the O_2 flow low enough for meaningful stoichiometries in between AlN and Al_2O_3. Working with a gas mixture at the central inlet implies that in addition to the 12 sccm N_2 at the target, N_2 also flows to the substrate. Alternatively, the installation of a mass flow controller for lower flows of pure O_2 could be considered or the use of compound gases such as N_2O[17].

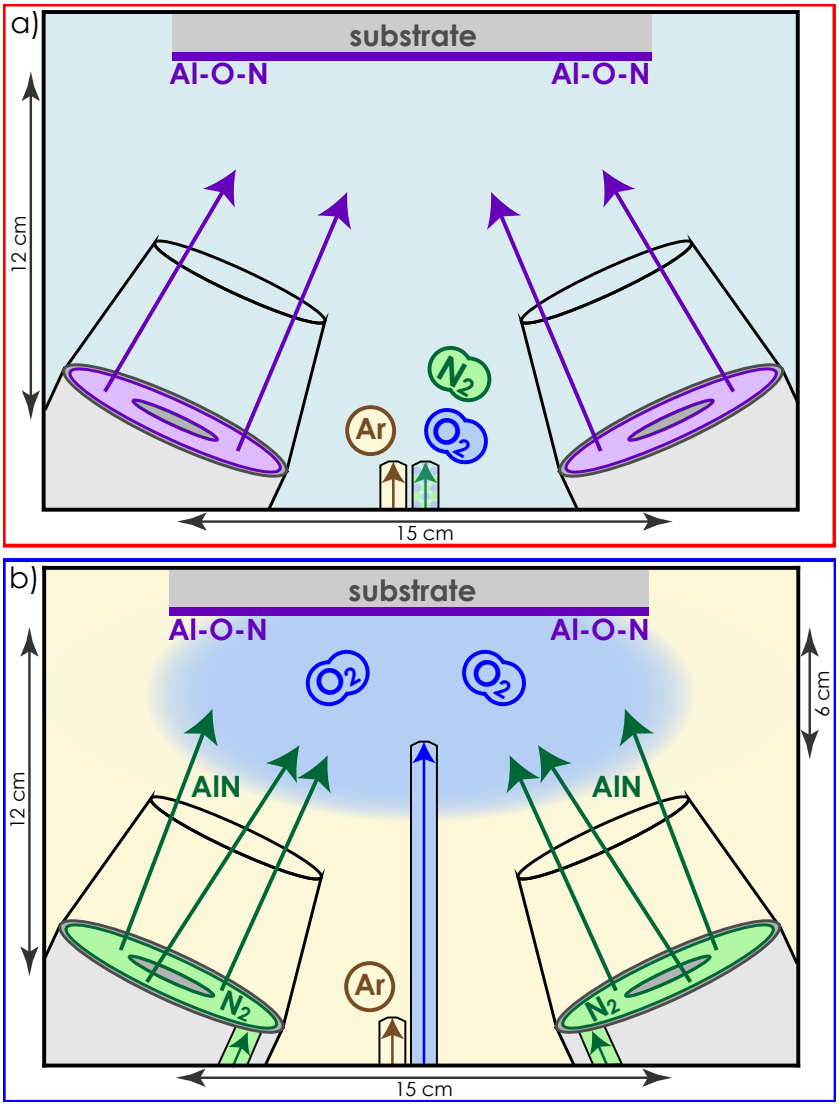

Figure 2.1: Combined O_2/N_2 gas inlet setup a) and separated inlets setup b). In both, Ar had its own inlet at the chamber bottom center and its flow was kept constant at 16 sccm. Photographs of the combined inlet setup *in operando* are published in ref[172]. In the combined inlet setup a), the two reactive gases O_2 and N_2 entered via the same inlet placed at the same position as the Ar inlet. Their total reactive gas flow amounted to 12 sccm. The O content within was varied between 0-10% to obtain samples of different stoichiometries. In the separated inlets setup b), each reactive gas was introduced via its own independent gas line to a specific chamber position. N_2 was fed to the targets at a constant flow of 12 sccm. O_2 was piped past the sputter guns into the proximity of the substrate at an additional flow of 0-1 sccm.

With the combined reactive gas inlet setup (see fig. 2.1a)), a 3 h deposition followed directly after the target cleaning (without an intermediate poisoning step) and was carried out with a total reactive gas flow of 12 sccm at a certain O_2/N_2 ratio. This ratio was changed from run to run to achieve O_2 contents between 0-10% in the reactive gas. The total reactive gas flow was thus the same for all processes carried out in the combined inlet setup irrespective of the absolute O_2 flow.

Voltage versus time traces were logged in steps of 5 s during all deposition processes. After each process in either setup, the Al targets were again cleaned to their metallic state by sputtering for 3 min in pure Ar. Modeling[9] and experiments[5] showed that during the simultaneous use of two reactive gases, care has to be taken to avoid a trapping of the target in the poisoned mode. Such a trapping was not observed. Ar was of 6.0 quality grade, N_2 and O_2/N_2 mixtures were of 5.0 quality grade (Messer Schweiz AG). All gases were purified over small Alphagaz Purifiers (H_2O free for the O_2/N_2 mixture and O_2 free for the N_2 and Ar lines) (Air Liquide Deutschland GmbH). The working pressure during deposition and poisoning processes amounted to 0.2-0.4 Pa (depending on the amount of reactive gas required for a specific deposition) and was achieved at full pumping speed. For cleaning steps, the pumping power was reduced to yield Ar pressures of 1.5 Pa. The base pressure of the chamber remained below $2{\cdot}10^{-5}$ Pa.

Simultaneous to the target preparation steps prior to a process, the substrates were cleaned with an RF bias of 75 V for 10 min. Polished Si(100) wafers (Silicon Materials (Si-Mat)) and microscope glass slides (Menzel-Gläser) were used as substrates. Deposition rates were calculated from film thicknesses measured with a Dektak XT profiler (Bruker).

Transparency of the obtained films was checked by eye for the coated glass substrates and confirmed by ellipsometry done on the coated Si(100) substrates. Film compositions were determined by RBS and heavy ion ERDA. RBS and ERDA measurements and evaluations were performed at the Laboratory of Ion Beam Physics (LIP) at the Swiss Federal Institute of Technology, Zürich (ETHZ). For RBS, samples were irradiated by 2 and/or 4 and/or 5 MeV ^{4}He. The backscattered beam was analyzed by a Si PIN diode detector placed under 168°. For ERDA, the samples were bombarded by 13 MeV ^{127}I under 18° incidence angle,

and recoiling ions were analyzed in an ERDA detector telescope developed at LIP. It consists of a time-of-flight (ToF) system coupled to a gas ionization chamber (CIG)[82]. The compositional contents of Al and the major e^- acceptor - either O or N - were determined by RBS. The minor e^- acceptor content was then refined via N/O ratio obtained from ERDA. This procedure was chosen, since ERDA has a higher sensitivity for light elements, while RBS has a better absolute accuracy for stoichiometry determination. For RBS, the algorithm RUMP[35] was applied to simulate the obtained spectra. For ERDA, custom made analysis software has been used to determine elemental ratios.

2.3 Results

Al-O-N thin films were deposited with two setups, differing only in their reactive gas inlets. The process gas Ar was introduced at the center of the chamber bottom at a constant flowrate of 16 sccm for all experiments.

Fig. 2.1a) shows the (more conventional) combined inlet setup. The two reactive gases O_2 and N_2 were introduced at the same position as the process gas Ar, distant from the targets. The total flow of the reactive gases was kept constant at 12 sccm. To obtain different Al-O-N stoichiometries, the O_2 content in the total reactive gas flow was varied from 0-10%.
Fig. 2.1b) illustrates the (modified) separated inlets setup. Two separate gas inlets were used for O_2 and N_2, alongside the unchanged Ar inlet. N_2 was introduced directly at the targets with a constant flow rate of 12 sccm to ensure their fully nitrided state. O_2 was introduced away from the targets through a central gas inlet to close proximity of the substrate. Different stoichiometries were achieved by varying the O_2 flow between 0-1 sccm.

With the combined inlet setup (fig. 2.1a)), even small O_2 flow rates resulted in an unstable deposition process. Arcs, indicated by a visible flickering of the plasma, were detected by the arc-supression electronics of the power supply. The red curve in fig. 2.2a) shows a typical voltage versus time trace with repeated

voltage break-downs indicative for frequent arcing. In fig. 2.2b), the dependence of the measured deposition rates on the O_2 flow is plotted as red rhombi.

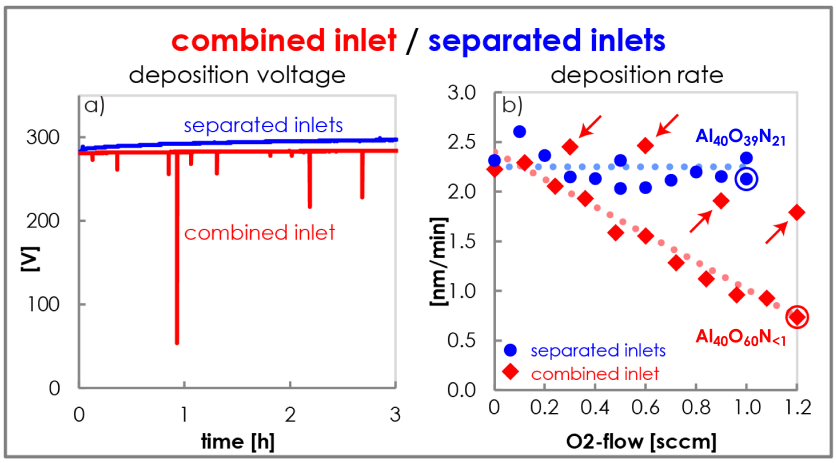

Figure 2.2: Deposition voltages over time a), logged in time steps of 5 s, and deposition rates versus O_2 flows b). Red data traces and rhombi were obtained working with the combined inlet setup, blue data traces and dots with the separated inlets setup. For the typical deposition voltage trace a) recorded in the combined inlet setup, 12 sccm of reactive gas containing 3% O_2 were flowing. For that in the separated inlets setup, 12 sccm N_2 were fed to the targets and 0.4 sccm O_2 to the substrate via the central inlet. The O_2 flow rates were thus at the same level for both cases. Altering the flow rates within the range applied for this work did not influence the nature of the voltage traces in either case. For the deposition rates b), different O_2 contents were applied. Eye guides are added as dotted lines and significant stoichiometries are given for encircled data points.

The graph indicates a linear decrease of the deposition rate with increasing O_2 flow rate (dashed eye guide). However, the deposition rates were found to be irreproducible (red arrows). For example, a film prepared with 1.2 sccm O_2 in 10.8 sccm N_2 is encircled in red in fig. 2.2b). N_2 constitutes 90% of the reactive gas, but N is almost absent in the final film having the composition $Al_{40}O_{60}N_{<1}$ determined by RBS/ERDA. An inspection of the target after repeated deposition, depicted in fig. 2.3a), reveals that the surface is covered by black spots (hillocks). RBS/ERDA show that these consist of substoichiometric Al-O-N containing variable O and N amounts. The magnified area illustrates the roughened surface.

With the separated gas inlet setup (fig. 2.1b)), stable deposition processes were obtained for all O_2 flows. The blue sputter voltage versus time trace in fig. 2.2a) remains constant during the entire process, and a stable plasma is observed visually. No arcs were detected. The deposition rate, plotted as blue dots in fig. 2.2b), stays at the level obtained for an O_2-free AlN deposition and is reproducible within the applied O_2 flow range. A film sputtered with 12 sccm N_2 at the targets and 1 sccm O_2 at the central inlet, encircled in blue in fig. 2.2b), has the chemical composition $Al_{40}O_{39}N_{21}$. A target used in this setup, shown in fig. 2.3b), remains smooth and clean.

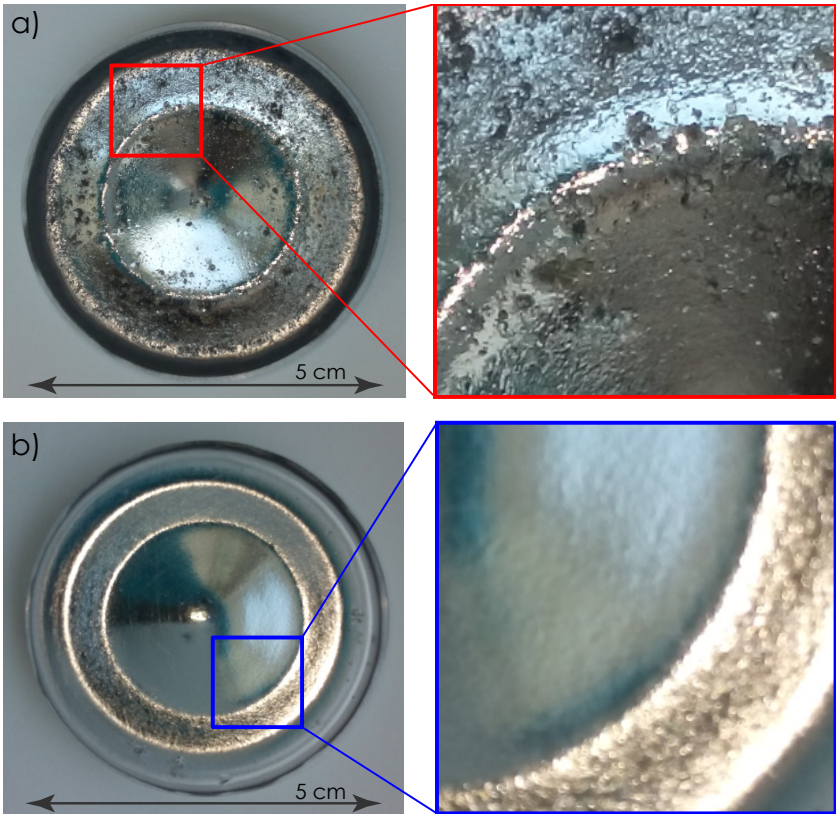

Figure 2.3: Photographs with magnified areas of targets used in the combined gas inlet setup a) and in the separated inlets setup b). The target used in the combined inlet setup has a rough surface covered by black spots (hillocks), while the target applied in the separated inlets setup stays smooth and artifact-free.

For the work reported here, films with stoichiometries between AlN and Al_2O_3

were prepared. ERDA/RBS and optical transparency confirmed that all films were fully nitrided and/or oxidized with no metallic Al left.

2.4 Discussion

In R-DCMS, the reaction processes relevant for film formation take place at the substrate and at the target. Here, two reactive gases (O_2 and N_2) with different bond dissociation energies (BDEs) and different reactivities towards Al are used (see table 2.1). Our experiments revealed that the sputtering process was unstable for the combined inlet setup, where both reactive gases are introduced near the target. The inspection of the latter revealed a partially oxidized surface. Prior experimental and simulation work showed that sputtering from an O poisoned target is problematic[3,157,159,139,9]. Because of the lower BDE of O_2 (498 kJ·mol^{-1}) compared to that of N_2 (944 kJ·mol^{-1})[99,27], the high sticking coefficient (α) of O_2 in plasma towards Al (0.1[32,90]) and the high formation enthalpy ($\triangle H_f^o$) of Al_2O_3 (838 kJ·mol^{-1} for $AlO_{1.5}$ units[20]), the oxidation of Al can occur even outside the plasma at the substrate. A corresponding reaction of N_2 with Al requires a substantial energy input, for example provided by a plasma. Hence it is predominantly O_2 that reacts with the growing film outside the dense plasma created by the magnetron. At the Al target, however, inside the dense plasma located there, both gases will react with the Al surface. Because the sputter rate is approximately inversely proportional to the thermodynamic stability of the local target surface[182, p. 6], the sputter yield from a nitrided part ($\triangle H_f^o = 318$ kJ·mol^{-1} for AlN units[20]) is higher than that from an oxidized one. As a consequence, oxide islands will form, and rapidly grow in area and thickness, until the whole target surface is predominantly oxidized. Due to the low thermal conductivity (λ) of Al_2O_3 (35 W·K^{-1}·m^{-1} [18]) regions and their large thickness, the deposition process leads to a rise of the temperature on these islands, because heat arising from sputtering cannot be deduced into the target. The additional thermal energy further facilitates the growth of Al_2O_3 islands in area and thickness.

Because Al_2O_3-covered areas of the sputter target are electrically insulating, these areas become positively charged with respect to the negative cathode po-

Table 2.1: Characteristic quantities for gases and solids relevant in Al-O-N sputter deposition. α^{Al}: Sticking coefficient of a gas towards Al. BDE: Bond dissociation energy given in [kJ·mol^{-1}]. $\triangle H_f^o$: Standard enthalpy of formation given in [kJ·mol^{-1}]. λ: Thermal conductivity given in [W·K^{-1}·m^{-1}]. 35 W·K^{-1}·m^{-1} is for monocrystalline α-Al_2O_3 (sapphire). 319 W·K^{-1}·m^{-1} is for for monocrystalline AlN wurtzite. γ: Secondary electron emission coefficient.

gases	$\mathbf{O_2}$	N_2	
α^{Al} in plasma	$0.1^{32,90}$	not reported	
BDE [kJ·mol^{-1}]	$494^{99,27}$	$942^{99,27}$	
solids	$AlO_{1.5}$	AlN	Al
$\triangle H_f^o$ [kJ·mol^{-1}]	838^{20}	318^{20}	0
λ [W·K^{-1}·m^{-1}]	35^{18}	$319^{153,151}$	237^{171}
γ	$0.19^{30,31}$	$0.22^{30,31}$	$0.09^{30,31}$

tential on the remaining metallic target surface. Once the electric field is strong enough, a discharge takes place in the form of an arc. The arc provides the electrical contact to generate a short between cathode and ground, and the voltage set to the target breaks down (fig. 2.2a)). Continuous arcing destroys the target, and a rough surface with black spots (hillocks) and valleys in the mm range forms (fig. 2.3a)). An avalanche effect sets in, as the growth of hillocks and the arcing mutually reinforce each other. Consequently the sputter rate becomes unstable and generally smaller.

With the separated gas inlet setup, the O_2 gas reacts only at the substrate surface, but not at the target. The gettering effect of the film growing on the substrate reduces the O_2 partial pressure near the target. The higher N_2 concentration at the target then leads to the formation of an AlN layer at the target surface (N_2 poisoning). Because of the lower $\triangle H_f^o$ of AlN and its good λ (319 W·K^{-1}·m^{-1} [153,151]), the AlN coverage remains thin and no hotspots occur. This provides stable sputtering conditions, as discussed in prior work[3,157,159,139,9].

A comparison of films fabricated with the same O_2 flow rates using the separated inlets and the combined inlet revealed compositions of $Al_{40}O_{39}N_{21}$ and $Al_{40}O_{60}N_{<1}$, respectively. The higher O content of the latter film arises from a stronger target oxidation and from negatively charged O species such as O^- and O_2^-, which form in the combined inlet setup close to the target and are accelerated by the cathode

sheath towards the substrate. Such O species hit the substrate with high energy and can cause sputter damage in the growing film[110,136,120 182, p.101/227], which was however not observed in the coatings reported here. Note that the secondary electron emission coefficients (γ) of AlN (0.22) and Al_2O_3 (0.19) are similar and considerably higher than that of metallic Al (0.09). The sputter voltage can thus serve as a proxy to distinguish between metallic and poisoned target state, but not between nitrided or oxidized target.

2.5 Conclusion

Al-O-N thin films were fabricated with two different reactive gas (N_2, O_2) inlet configurations in an R-DCMS system. No costly hardware installations were needed. The composition of the films was varied between AlN and Al_2O_3 using different flow ratios of the reactive gases. All films were fully transparent, indicating that no metallic Al is incorporated in the films.
Stable sputtering conditions without loss in the deposition rate could only be obtained when using separate gas inlets for the two reactive gases (at the target for N_2 and near the substrate for O_2). With a combined inlet, stable sputtering conditions could not be obtained, and the surface of the Al target roughened and was finally covered by black hillocks.
Our work demonstrates that reactive sputtering with highly reactive gases such as O_2 can be performed by conventional R-DCMS, provided that the gas inlet system is designed to obtain well-controlled target poisoning.

Acknowledgments

The Swiss National Science Foundation [project Nr. 200021_150095] and Empa are gratefully acknowledged for the financial support. Cordial thanks go to Max Döbeli and his team from the LIP at ETHZ for RBS and ERDA analyses, and to Erwin Hack from the Laboratory for Transport at Nanoscale Interfaces at Empa Dübendorf for ellipsometry analyses.
Declarations of interest: None.

3 Understanding the microstructural evolution and mechanical properties of transparent Al-(Si-)(O-)N films

The text and figures of the following chapter are verbatim copy of a manuscript submitted (on 1st April 2019) to
Science & Technology of Advanced Materials.

Authors

Maria Fischer[a,*)], Mathis Trant[a)], Kerstin Thorwarth[a)], Rowena Crockett[a)], Jörg Patscheider[b,1)], Hans Josef Hug[a,c)]

[a)] Empa, Swiss Federal Laboratories for Materials Science and Technology, Überlandstrasse 129, 8600 Dübendorf, Switzerland

[b)] Evatec AG, Hauptstrasse 1a, 9477 Trübbach, Switzerland

[c)] Department of Physics, University of Basel, Klingelbergstrasse 82, 4056 Basel, Switzerland

[1)] Empa, Swiss Federal Laboratories for Materials Science and Technology, Überlandstrasse 129, 8600 Dübendorf, Switzerland (until 31.10.2017)

[*)] Corresponding author.

Keywords

aluminum oxynitride, Al-O-N, aluminum silicon oxynitride, Al-Si-O-N, coatings, thin films, transparent, hard, microstructure, reactive sputtering

Abstract

Optically transparent, colorless Al-O-N with O contents between 0 and 60%, and Al-Si-O-N coatings with selected Si and O contents were fabricated by reactive direct current magnetron sputtering (R-DCMS) from elemental Al and Si targets and O_2 and N_2 reactive gases. The Si/Al content was adjusted through the electrical power on the Si and Al targets, while the O/N content was controlled through the O_2 flow piped to the substrate in addition to the N_2 flow at the targets.
The structure and morphology of the coatings were studied by X-Ray Diffraction (XRD) and Transmission Electron Microscopy (TEM), while the elemental composition was obtained from Rutherford Backscattering Spectrometry (RBS) and heavy ion Elastic Recoil Detection Analysis (ERDA). The chemical states of the elements in the coatings were analyzed by X-Ray Photoelectron Spectroscopy (XPS). Based on these analytical results, a model describing the microstructural evolution of the Al-O-N and also previously studied Al-Si-N [122,123,125,129] coatings with O and Si content, respectively, is established. The universality of the microstructural evolution of these coatings with the concentration of the added element is attributed to the extra valence electron (e^-) that must be incorporated into the AlN wurtzite host lattice. In the case of Al-O-N, the additional valence charge arises from the e^- acceptor O replacing N in the AlN wurtzite lattice, while the e^- donor Si substituting Al fulfills that role in the Al-Si-N system.
In view of future applications of ternary Al-O-N and quaternary Al-Si-O-N transparent protective coatings, their mechanical properties such as residual stress (σ), hardness (HD) and Young's modulus (E) were obtained from the curvature of films deposited onto thin substrates and by nanoindentation, respectively. Moderate compressive stress levels between -0.2 and -0.5 GPa, which suppress crack formation and film-substrate delamination, could be obtained together with HD values around 25 GPa.

3.1 Introduction

Protective coatings are of critical importance for obtaining a performance enhancement of machinery and equipment or to protect the latter when used in harsh environments[192]. The properties and lifetime of a coating depend on its microstructure and physical and chemical properties. The chemical composition of the coating and the local chemical environment of its constituents must be controlled by the fabrication process and tuned to obtain optimized properties for specific applications. For example, the stress state of the coating must be optimized to prevent delamination and also to obtain closed boundaries between individual grains for a high inertness in corrosive environments.

Here, we are interested in protective coatings that are optically transparent, for example to protect optical devices or tools. A candidate material for transparent hard coatings is AlN, a group III nitride that forms as a polycrystalline wurtzite film when deposited by reactive direct current magnetron sputtering (R-DCMS). It has been observed that a microstructural film evolution can be induced by doping group IV and VI elements (Si, Ge, Sn and O) into AlN. Al-Ge-N[93], Al-Sn-N[92] and Al-Ge-O-N[77] are however not totally transparent but show colors ranging from yellow to red and brown, as the bandgap decreases from that of AlN with increasing contents of Ge and Sn. In our previous work[122,123,125], we have shown that Al-Si-N fabricated by R-DCMS is optically transparent and colorless for the complete range of Si contents tested.

For Si contents up to 6%, the films show a polycrystalline (002) oriented wurtzite structure with crystallites decreasing in size and a c-axis lattice parameter shrinking linearly for increasing Si concentration. We concluded that the lattice shrinking arises from Si incorporated in the wurtzite crystals in the form of a crystalline solid solution. For Si concentrations between 6-12%, the c lattice parameter remains constant. We concluded that an additional amorphous Si_3N_4 phase encapsulating the wurtzite grains, *i.e.* a nanocomposite, formed in this Si concentration range. A hardness (HD) maximum is obtained for about 10% of Si. For higher amounts of Si, a gradual loss of crystallinity is observed, and coatings with more than 25% Si were found to be fully X-ray amorphous[122,123,125]. In our previous work, the microstructure and properties of the films were modified by changing

the content of the group IV element Si in the Al-Si-N films. Si with its low Pauling Electronegativity χ_{Si}=1.8 replaces the electron (e^-) donor Al with χ_{Al}=1.5 in the Al-N compound.
In this study, we use O, an electronegative group VI element, to obtain a specific film microstructure and with it modified physical properties of the resulting Al-O-N films. Here, however, O with its high χ_O=3.5 replaces the e^- acceptor N with χ_N=3.0[183] in wurtzite.
In addition to Al-O-N, we investigate quaternary Al-Si-O-N films fabricated by the simultaneous increase of Si and O during the R-DCMS process. For both coating materials, Al-O-N and Al-Si-O-N, we report the changes in hardness (HD), elastic modulus (E) and residual stress (σ) that occur with changing microstructure.

3.2 Al-O-N thin film preparation and chemical analysis

Al-O-N coatings were deposited onto Si(100) wafers and glass by R-DCMS from metallic Al targets using O_2 and N_2 as reactive gases. Instabilities typically occurring in reactive sputter processes with O_2 could be avoided by our modified sputter system setup described in ref.[44]. The chemical compositions of the films were determined by RBS/ERDA.
Fully reacted, optically transparent Al-O-N films have a well-defined stoichiometry given by $AlO_{1.5(1-z)}N_z$ with $z_{max} = 1$ (AlN with 0% O) and $z_{min} = 0$ (Al_2O_3 with 60% O), as can be derived from the valences of the chemical elements of the films. The O content in the coatings was varied from 0-60% through the O_2 flow in the deposition process. Coatings in the range of 8-16% were found to contain up to 3% H.
Further experimental details are given in ref.[44] and in the supplementary material.

3.3 Analytical results obtained from Al-O-N films of different O content

3.3.1 Crystalline structure

AlN films deposited by R-DCMS for this study show only the wurtzite (002) peak and the higher order (004) peak in diffractograms from XRD θ-2θ scans symmetric to the AlN film surface. This implies that AlN films are purely (002) textured in the growth direction (z). This is confirmed by a (002) pole figure (PF), which shows a single central pole for a sample inclination angle ψ=0.
θ-2θ scans in-plane, thus orthogonal to the sample surface and correspondingly to (002), show (100) and (110) signals. Both peaks have intensities that do not vary if the sample is rotated around its central z axis by φ. The crystallites hence have no preferred in-plane orientation. This is confirmed by (103) and (101) PFs, which show rims at ψ=31.6° and 61.6°, respectively, with constant intensities over the entire φ-circle. The AlN films thus have (002) fiber texture.

For Al-O-N films with an O concentration between 0 and 8%, the (002) fiber texture of the film persists. The (002) peak shifts linearly to higher 2θ diffraction angles, broadens and decreases in intensity with increasing O concentration. The c-axis lattice spacing calculated from the (002) peak position, the crystallite size (CS) and the microstrain (MS) obtained from a line profile analysis (LPA)[11], are plotted in fig. 3.1a), b) and c), respectively.
The wurtzite c-axis lattice parameter decreases by -0.5% from 0.4975 nm for AlN to 0.4950 nm for Al-O-N for an O content increased from 0-8%. Asymmetric θ-2θ scans reveal a lattice shrinkage also in the directions of (105), (104) and (103) for increased O contents and hence a contraction of the crystal unit cell. In previous work addressing the Al-Si-N system, the observed contraction of the wurtzite crystal lattice with increasing Si content was attributed to the generation of V(Al) vacancies in Al lattice sites. These V(Al) were proposed to form upon Si(Al) substitution as compensation for the additional valence e^- in Si compared to the replaced Al[129]. As O also contains an additional e^- compared to N, we conclude that the O(N) substitution occurring in Al-O-N also leads to V(Al) and therefore

to the observed wurtzite lattice shrinkage upon increasing O content.

Together with the crystal cell contraction, we observe a grain refinement (fig. 3.1b)). The CS decreases from 140 nm to 60 nm in Al-O-N with an O concentration increased from about 2 to 8%. For films with a lower O concentration, scattering of the CS between 70 and 130 nm is observed, typical for materials exhibiting mosaicity. The MS (fig. 3.1c)) remains constant around $2{\cdot}10^{-5}$. (002) rocking curves (RCs) broaden with increasing O content, which indicates that the crystallites assume a progressive misorientation of the c-axis off the growth direction z.

No further shift of the (002) peak is observed for films with 8-16% O content. Consequently, the c lattice remains constant. This behavior is similar to that found in the Al-Si-N system, where no further lattice shrinkage was observed for a Si content higher than 6%. We thus identify an O concentration of 8 % as the solubility limit for O incorporated into the wurtzite lattice. Consequently, excess O of concentrations between 8-16% is incorporated in the form of a separate phase. As no additional diffraction peaks occur from this phase, and the films remain transparent, we conclude that the second phase consists of amorphous Al_2O_3 that encapsulates the AlN grains, hereby forming a nanocomposite. The CS was found to shrink slightly from 60 nm down to 40 nm (fig. 3.1b)). The microstrain increases from about $2{\cdot}10^{-5}$ to about $6{\cdot}10^{-5}$ for an O concentration above 8%, indicating that the formation of the amorphous grain boundary phase exerts a pressure onto the Al-O-N grains.

At an O content approaching 16% O, wurtzite (100) and (101) peaks appear in addition to the major (002) peak in symmetric θ-2θ diffractograms. We conclude that at these high O concentrations the uniaxial (002) texture is lost, and crystallites with other orientations appear. The XRD results of two typical samples with such a mixed, yet highly preferred (002) orientation are plotted with open symbols in fig. 3.1. Their c lattice parameter and CS are lower, and their MS significantly higher compared to purely (002) textured samples.

For Al-O-N films with 16-20% O, the (002) peak develops an asymmetric shoulder towards lower 2θ, possibly arising from a weakly ordered grain boundary phase. For O contents of 20-30%, only small humps between 30-40° in 2θ are visible in the

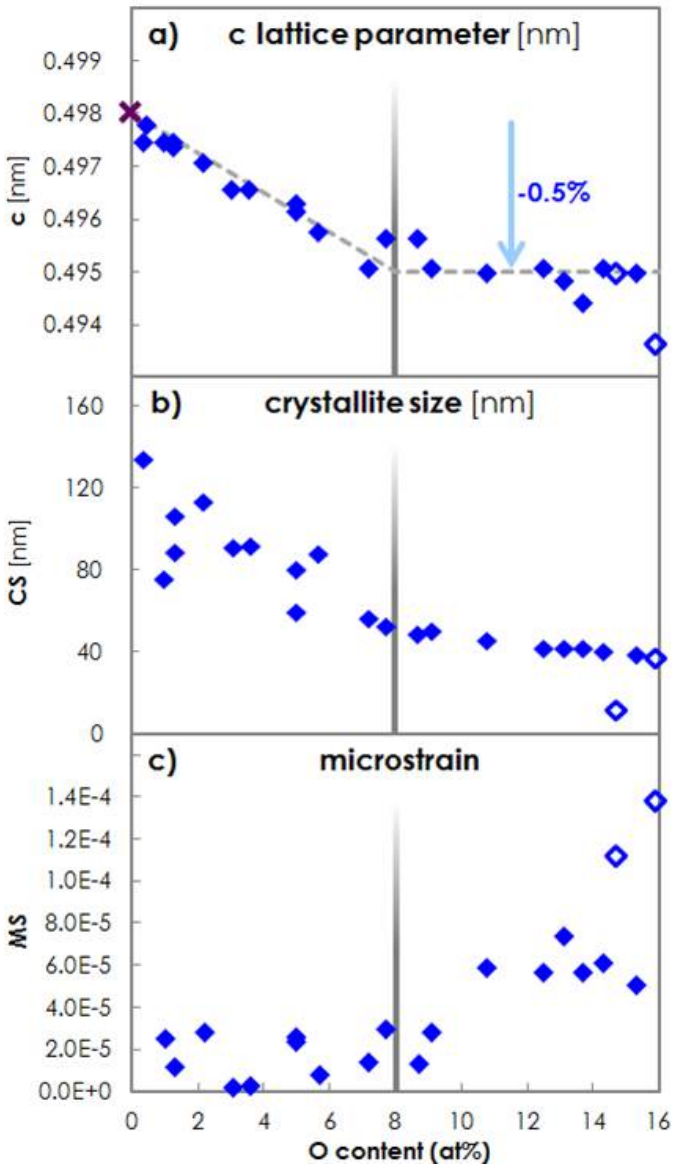

Figure 3.1: a) c-axis lattice parameter [nm] (found to be parallel to the (002) axis and the growth direction z) of wurtzite crystallites. The literature value for c in AlN[145] is marked by a purple cross. The dashed lines highlight the linear decrease of c observed between 0 and about 8% O, as well as that no further lattice shrinking occurs above 8% O. b) crystallite size (CS) [nm] and c) microstrain (MS) in Al-O-N plotted versus O content. XRD results of specific samples without uniaxial (002) texture with O concentrations below 16%, *i.e.* within the O content range typically leading to a (002) fiber texture, are shown by open symbols.

diffractograms, which cannot be clearly attributed to a crystalline phase. We can thus conclude that at such high O contents of 16-30%, the coatings contain small, poorly aligned grains. The volume fraction of the crystalline phase decreases, while that of the amorphous tissue phase increases. Films with O contents beyond 30% are X-ray amorphous.

3.3.2 Cross-sectional film structure

Fig. 3.2 shows cross-sectional Transmission Electron Microscope (TEM) bright field (BF) images (left), electron diffraction (ED) patterns (small insertions) and high resolution (HR) images (right) of samples with O contents of a) 5.0%, b) 13.9% and c) 16.6%.

The cross-sectional TEM of the film with 5% O in fig. 3.2a) shows a columnar structure along the z-direction (green arrow). The ED pattern in fig. 3.2a) contains sharp wurtzite diffraction spots. The HR TEM reveals large coherent crystalline regions. This confirms the (002) wurtzite fiber texture of the films revealed by our XRD analysis.

Fig. 3.2b) displays cross-sectional TEM data for a film containing 13.9% O. Again a fiber texture is apparent, but the ED pattern shows broadened spots, compatible with the decreasing alignment of the (002) axes of crystallites along the growth direction z.

The grain refinement (fig. 3.1b)) and loss of (002) texture at higher O concentrations becomes apparent in the TEM results displayed in fig. 3.2c), showing data obtained on a film with 16.6% O. Only faint column features are visible in the BF image. The ED pattern consists of rings with an increased brightness along the (002) direction. This indicates that (002) is still the preferred orientation that crystallites adopt in z, but that the pure (002) fiber texture observed in films with lower O contents is lost, and grains of random orientation exist. The latter is confirmed by the HR TEM data, where crystallites of 5-10 nm length with different (002) orientations are visible (encircled with dashed yellow lines in fig. 3.2c)).

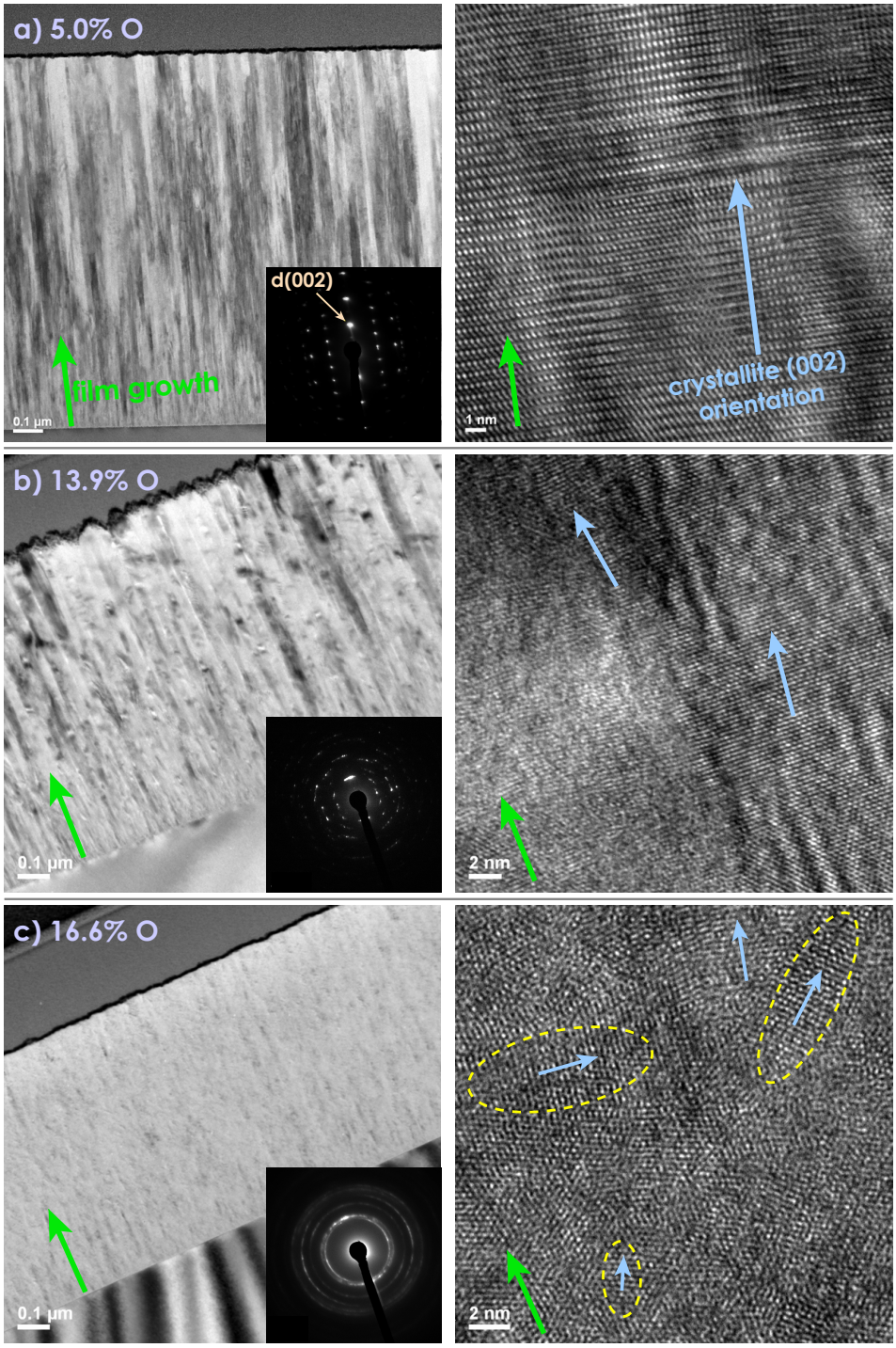

Figure 3.2: TEM images of cross sections of Al-O-N thin films with different O contents of a) 5.0% (top), b) 13.9% (middle) and c) 16.6% (bottom). On the left, a BF image and an ED pattern (small insert), and on the right, a HR image for each sample are shown. Film growth directions are indicated with green, crystallite (002) orientations with blue arrows. For the 16.6% O sample, nanometer-sized crystallites typically occurring for such an O content are highlighted by yellow, dashed ellipses.

3.3.3 Chemical states

The dependence of the chemical states of Al, N and O in Al-O-N films on their O content was analyzed by X-Ray Photoelectron Spectroscopy (XPS), recording binding energy (BE) and full width at half maximum (FWHM) evolutions of photoelectron (photo e^-) lines. Fig. 3.3 shows the BEs (panels a), c), e)) and FWHMs (panels b), d), f)) of the photo e^- lines Al *2p*, N *1s* and O *1s* in Al-O-N coatings with increasing O content from 0-60%. This O content range corresponds to a variation of the material composition from AlN (0% O) over Al-O-N up to Al_2O_3 (60% O).

The BE_{Al2p} in Al-O-N is higher than in metallic Al, which has a BE_{Al2p} of 72.6 eV. The reason for this is that Al in Al-O-N is oxidized as it acts as an e^- donor, because χ_{Al} of 1.5 is lower than χ_O of 3.5 and χ_N of 3.0[183]. The BE_{Al2p} increases linearly from 72.5 in AlN to 74.5 eV in Al_2O_3, *i.e.* with increasing O content from 0-60% (see dashed gray line in fig. 3.3a)). Concordant values for Al *2p* in sputter deposited AlN of 72.5 eV[124] and Al_2O_3 of 74.6 eV[133] are reported (see gray circle and gray open circle in fig. 3.3a)). The increase of BE_{Al2p} occurs as an increasing number of Al-N bonds are replaced by Al-O bonds. As O is more electronegative than N, Al-O bonds are more polar than Al-N bonds, thus the average oxidation level of Al and therefore BE_{Al2p} increase with increasing O content.

$FWHM_{Al2p}$ increases linearly from 1.5 to 1.8 eV with increasing O content from 0-8% (see dashed gray line in fig. 3.3b)). In this O content range, XRD reveals that a solid solution forms, in which O populates the N-sites in wurtzite crystallites. While Al as e^- donor remains in cationic wurtzite lattice sites, incorporating O replaces N in anionic lattice sites, as both O and N are e^- acceptors. In wurtzite, cationic sites are coordinated to only anionic sites and vice versa. Al is thus directly connected to N and O. Hence, the variability of the Al oxidation states grows and the $FWHM_{Al2p}$ broadens with increasing O content. Beyond the solubility limit of 8% O in wurtzite, $FWHM_{Al2p}$ stays constant at 1.8 eV (see dashed gray line in fig. 3.3b)). The reason for this is that from 8% O upwards O is no longer incorporated into the AlN wurtzite lattice but an X-ray amorphous Al_2O_3 grain boundary phase, that increases in volume with increasing O content is formed. In this phase, no higher oxidation level of Al than that in Al_2O_3 can form, thus the Al *2p* line

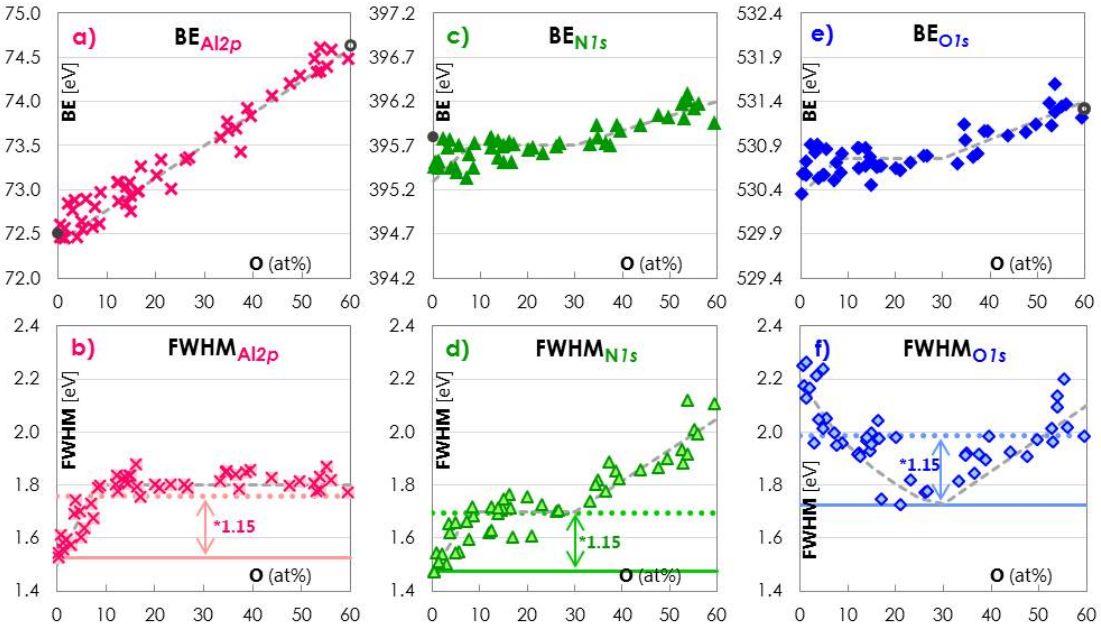

Figure 3.3: The top panels show the dependence of the a) Al *2p*, c) N *1s* and d) O *1s* binding energies (BEs) on the O content. The dashed gray lines highlight the evolution of the BEs on O content discussed in the main text. Literature values are marked with gray circles for AlN[124] and with gray open circles for Al_2O_3[133]. The bottom panels b), d) and f)) display the Full Widths at Half Maximum (FWHM) of the photo e^- lines. Again dashed gray lines are shown to highlight the observed dependence on the O content. Solid and dotted lines are added to the graphs highlighting the observation of a broadening more than by a factor 1.15 that has been previously indentified as a critical value for the occurance of disorder-induced line broadening[121,72,24].

does not broaden further. The $FWHM_{Al2p}$ value for O contents beyond 8% is more than 1.15 times wider than the initial FWHM in AlN of 1.5 eV (see dashed gray line in fig. 3.3b) and the dotted line highlighting the FWHM broadening by a factor of 1.15). We attribute this to significant disorder broadening due to a variation in the coordination around Al[121,72,24].

The BE_{N1s} in Al-O-N is lower than in molecular N_2, which has a BE_{N1s} of 405.3 eV[170]. This is due to N acting as e^- acceptor, as $\chi_N > \chi_{Al}$. For an O content between 0-8%, Al-N bonds in the wurtzite lattice are gradually replaced by Al-O bonds. In addition, V(Al) vacancies appear to compensate for the extra e^- from O compared to N[129]. We thus expect that the BE_{N1s} and $FWHM_{N1s}$ are modified by the presence

of next-nearest neighbor O in the Al-O-N wurtzite unit cell and nearest neighbor V(Al). As $\chi_O > \chi_N$, we expect that the e^- density at the N decreases with increasing O content, and consequently the $BE_{N\,1s}$ and the $FWHM_{N\,1s}$ increase. The dependence of the $BE_{N\,1s}$ on the O content (fig. 3.3c)) is compatible with such a scenario, while the $FWHM_{N\,1s}$ data clearly show a linear dependence on the O content (fig. 3.3d)). The latter is because the V(Al) induce a variation and therefore an increased scattering of the $BE_{N\,1s}$ (fig. 3.3c)) thus leading to a significant broadening of the N *1s* line (see dashed gray line in fig. 3.3d) and the dotted line highlighting the FWHM broadening by a factor of 1.15). For O contents between 8 and 30%, XRD reveals that no other crystalline phase than that of wurtzite containing 8% O is in the films, and that the CS in the latter decreases. It can therefore be proposed that an amorphous Al_2O_3 grain boundary phase of increasing thickness grows around the shrinking Al-O-N crystallites. Hence the chemistry of the Al-O-N grains and thus the $BE_{N\,1s}$ and $FWHM_{N\,1s}$ do not change. For O contents beyond 30% the films are X-ray amorphous. As the atoms no longer sit on lattice sites in the amorphous Al-O-N phase, a direct O-N interaction exists. The latter further increases the $BE_{N\,1s}$ as well as the $FWHM_{N\,1s}$ (see dashed gray lines in panels c) and d) of fig. 3.3 for this O content range). In addition, a weak second N *1s* photo e^- line appears at a BE of 401.8-402.5 eV compatible with the formation O-N bonds from partially oxidized N[70,96,39,154,180].

As with $BE_{N\,1s}$, the $BE_{O\,1s}$ in Al-O-N is lower than in molecular O_2, which has a $BE_{O\,1s}$ of 538.8 eV[170]. Also the dependence of the $BE_{O\,1s}$ on the O content in Al-O-N is equal to that of the $BE_{N\,1s}$ (fig. 3.3e)). This is a result of both species being e^- acceptors. However, a pronounced difference between the dependence of the $FWHM_{O\,1s}$ on O content (fig. 3.3f)) and that of $FWHM_{N\,1s}$ (fig. 3.3d)) is evident. The N *1s* line widens at high O concentrations, while the O *1s* line widens at low O concentration because at low concentration of each species, there is a wide variety of environments resulting in line broadening. The $FWHM_{O\,1s}$ reduces to a minimum at 30% O because at this concentration O predominantly exists in an amorphous Al_2O_3 grain boundary phase while the N is mainly present in the nanoscale Al-O-N grains. Above 30% O, both the $FWHM_{O\,1s}$ and $FWHM_{N\,1s}$ broaden due to the appearance of the additional N-O interaction in the amorphous Al-O-N phase.

3.4 Microstructural evolution model

We propose a model for the structural evolution of our Al-O-N films with increasing O content based on the experimental observations with XRD, TEM and XPS described above. The model, shown in fig. 3.4, is characterized by three regimes distinguished by O content.

At low O content of 0-8%, XRD and TEM reveal a wurtzite (002) fiber tex-

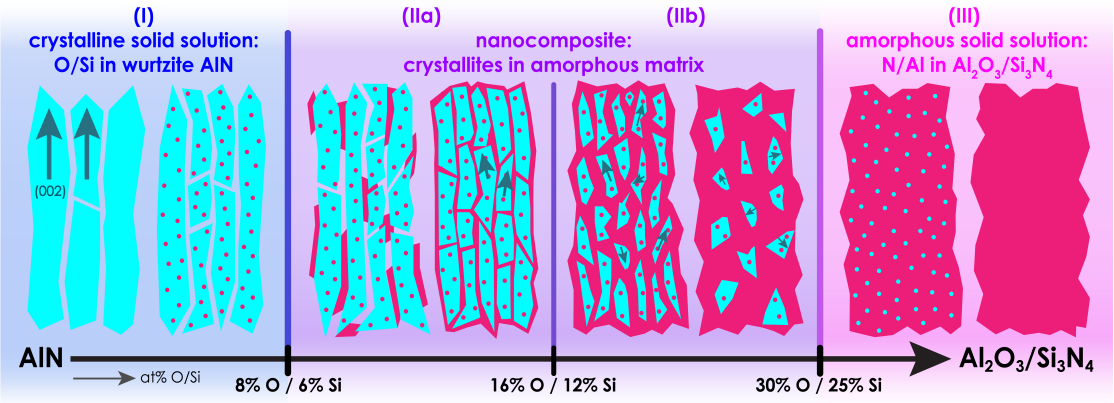

Figure 3.4: Microstructural evolution model of Al-O-N and Al-Si-N coatings with increasing O or Si content. Three regimes could be identified: Between 0-8% O (0-6% Si) a solid solution regime (I) exists. A shrinking of the c lattice parameter (fig. 3.1a)) accompanied by a gradual refinement of the grains (fig. 3.1b)) is observed. Between 8-16% O (6-12% Si) a nanocomposite sub-regime (IIa) is observed. The characteristics of the latter is a formation of an amorphous Al_2O_3 (Si_3N_4 for the case of Si added) grain boundary phase. In sub-regime (IIa) the (002) orientation of the crystallites remains along the growth axis z. This differentiates sub-regime (IIa) from (IIb). In the latter, the orientation of the crystallites along the 002 direction is gradually lost, as the O (Si) content is further increased from 16-30% O (12-25% Si). Above 30% O (25% Si), the coatings are X-ray amorphous.

ture in the Al-O-N films. While the compositional analysis with ERDA and RBS shows that an increase in O leads to a decrease in N, XPS reveals that both O and N are chemically reduced (fig. 3.3c) and e)) as they act as e^- acceptors. It can therefore be concluded that O substitutes N in the wurtzite lattice. Upon these O(N) replacements, the wurtzite lattice shrinks linearly with increasing O content (fig. 3.1a)) and the photo e^- lines Al *2p* and N *1s* exhibit a significant

disorder broadening in the XPS spectra (fig. 3.3d) and f)). These observations can be attributed to vacancies in the Al lattice sites, as one V(Al) forms per each three O(N) in order to compensate the additional valence e^- that O has compared to the replaced N. Simultaneously to the crystalline changes in the wurtzite grains, XRD shows a grain refinement (fig. 3.1b)) and a gradual loss of preferred orientation (XRD RCs) with increasing O concentration. This can be attributed to the e^- configuration of O, which mismatches the electronic structure of wurtzite and thus interrupts crystal growth. TEM images (fig. 3.2a)) reveal crystalline domains in contact with each other. We can thus conclude that coatings with 0-8% O belong to a crystalline solid solution regime (I) (fig. 3.4)), in which O (red dots) is integrated into wurtzite grains (green) exhibiting (002) fiber texture (green arrows). At intermediate O concentrations of 8-16%, the c-axis lattice parameter of the crystal grains in the Al-O-N films remains constant (fig. 3.1a)). This observation leads to the conclusion that the solubility limit of O in the wurtzite crystallites of the sputter-deposited Al-O-N coatings is reached at 8% O and that the structure of the wurtzite grains does not change with increasing O content. Consequently, above 8% O, the additional O must be contained in an Al_2O_3 grain boundary phase. This phase is not detected in XRD diffractograms and hence is amorphous. The microstrain increases in coatings with 8 to 16% O (fig. 3.1c)), supporting the formation of a grain boundary phase that exerts a pressure onto the wurtzite grains. In XPS spectra, the photo e^- lines Al *2p* and N *1s* do not broaden further between 8-16% O (fig. 3.3b) and d)), an observation that also corroborates the existence of a second phase. XRD PFs reveal that the (002) fiber texture persists, while TEM images and XRD RCs show that the clear (002) alignment of the crystallites along the z-axis is gradually lost at higher O contents (fig. 3.2b)). It can thus be concluded that Al-O-N films of 8-16% O are made up of a (002) fiber textured nanocomposite (IIa) (fig. 3.4), in which crystalline Al-O-N wurtzite grains with an increased (002) tilt (diverging green arrows) are progressively encapsulated in an amorphous Al_2O_3 matrix (red). At O contents of 16-30%, the XRD diffractograms show weak, broad peaks of (002) and further diffraction signals, and TEM reveals small crystallites oriented in arbitrary directions (fig. 3.2c)). Coatings with more than 16% O thus exhibit a gradual loss of crystallinity and a loss of the fiber texture and therefore belong to the nanocomposite sub-regime without uniaxial

texture (IIb) (fig. 3.4).
A third regime can be identified for O concentrations between 30-60%: XRD diffractograms of the Al-O-N films do not exhibit crystalline diffraction signals, signifying that the coatings are fully amorphous. XPS shows that the BE of all photo e^- lines as well as the FWHM of N *1s* and O *1s* increase, and that a second N *1s* component from oxidized N appears. These XPS results support the formation of an amorphous Al-O-N network in which bonds between all species exist. We conclude that coatings with more than 30% O consist of an amorphous solid solution (III) (fig. 3.4), in which progressively less N (green dots) is interspersed in an amorphous network consisting mainly of Al_2O_3 (red) up to the maximum of 60% O.

The microstructural evolution model of the Al-O-N system discussed here is reminiscent of the Al-Si-N discussed in earlier work[122,123,125,129], apart from a slightly lower solubility for Si in wurtzite and lower concentrations for the boundaries between regimes of the latter system. The concentration boundaries of the Al-Si-N system are also shown in fig. 3.4. It is noteworthy that in the Al-O-N system discussed here, the e^- acceptor N is replaced by the e^- acceptor O, while in the Al-Si-N system, the e^- donor Al is replaced by the e^- donor Si.

3.5 Material performance of Al-O-N coatings

Residual film stress (σ), hardness (HD) and Young's modulus (E) and their evolution with the microstructural state of protective hard (transparent) coatings govern their performance in applications.

The residual stress states σ of the coatings investigated in this study were determined with the new Stoney equation[75], using film thicknesses and curvatures of extra-thin (30 μm Si(100) / 145 μm glass) substrates measured by profilometry as input parameters. The dependence of σ in Al-O-N coatings with increasing O content is shown in fig. 3.5. For all coatings, $|\sigma|$ remains below 1 GPa. In the crystalline solid solution regime (I) of 0-8% O, σ is tensile and reaches values of 0.6-0.8 GPa. We attribute the tensile stress to the presence of open grain boundaries and consequently to the occurrence of attractive intergranular forces[185,2]. We

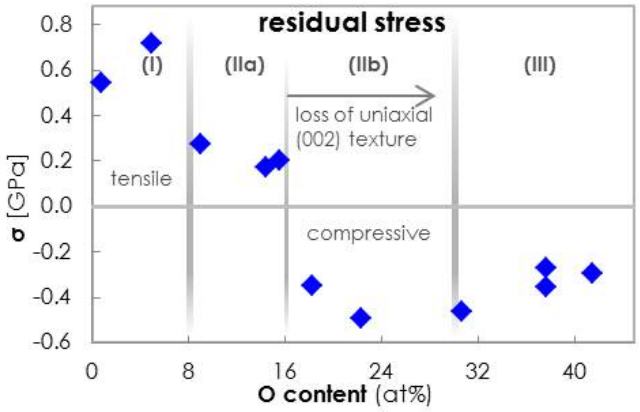

Figure 3.5: Evolution of the residual stress, σ, in Al-O-N coatings plotted versus the O content. σ was determined from films on extra-thin (30 μm) Si(100) wafers, as these bend instead of leading to stress relaxation cracks in the coatings. The microstructural regimes are distinguished with gray boundary lines.

observed that this stress level is high enough to cause relaxation cracks on regular (not extra-thin) Si substrates. Cross sections at locations of film cracks, prepared and imaged with a Gallium Focused Ion Beam SEM (GaFIB-SEM), revealed that the cracks propagate through the whole film and end inside the Si wafer (see supplementary material). This is typical for films that are stiffer than the substrate[10,149], as is the case for Al-O-N coatings of regime (I) on Si(100). $E_{\text{Al-O-N}}$ is 300 GPa in regime (I) (see fig. 3.6 discussed below), while E_{Si} is 130 GPa in (100) and 169 GPa in (110) direction. The Si substrates were found to crack open along (100) planes, as the mismatch in E between Al-O-N and Si(100) is larger than between Al-O-N and Si(110), and as the surface energy for Si(100) is with 1.36 Jm^{-2} lower than that of Si(110) with 1.43 Jm^{-2} [40,184,50].

In the fiber textured nanocomposite sub-regime (IIa) at 8-16% O, σ remains tensile but is at a lower level of 0.2-0.3 GPa, a stress level that allows crack-free films on substrates with conventional thickness. The reduction in tensile strength occurs along with the encapsulation of the crystallites by the amorphous Al_2O_3 matrix in (IIa), which prevents attractive forces between the grains (fig. 3.4). It has been reported that there are additional mechanisms for the reduction of tensile or the increase of compressive stress attributed to a volume increase arising from the in-

corporation of O[185,79,2]. In the nanocomposite sub-regime (IIb) at 16-30% O, σ becomes compressive and reaches values down to -0.5 GPa. This happens together with the loss of the uniaxial (002) fiber texture.
In the amorphous solid solution regime (III), σ relaxes to moderate compressive stresses of around -0.3 GPa.
Irrespective of the stress level, all coatings adhere strongly to the substrates (Si(100) and glass) and no delamination has been observed. The evolution of the film stress of the A-O-N thin film system with the O content described here is similar to that of the Al-Si-N system with the Si content[122], supporting the universality of the structural evolution model for these systems.

HD and E of Al-O-N coatings measured by nanoindentation are plotted in fig. 3.6 against increasing O content. In regime (I), the coatings exhibit high HD values of 20-25 GPa; the same value range is found in literature for binary AlN films[122,109,81]. In sub-regime (IIa), the Al-O-N coatings undergo a pronounced dip in HD down

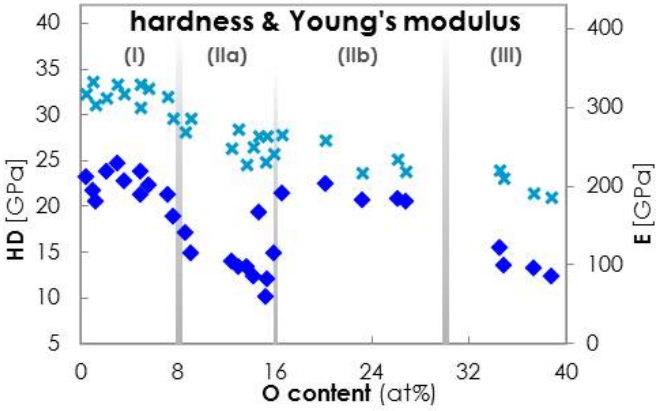

Figure 3.6: Evolutions of the hardness HD (blue rhombi, left axis) and Young's modulus E (bright blue crosses, right axis) of Al-O-N coatings plotted versus O content. The microstructural regimes are distinguished with gray boundary lines.

to values around 10-15 GPa. This observation is somewhat surprising, because the Al-Si-N systems shows a HD maximum in this sub-regime of the structural evolution model. We attribute the observed reduction of the HD in the Al-O-N system to the inclusion of hydrogen (H) that was detected by He-ERD in concentrations

up to 3% exclusively in this sub-regime. H terminates covalent interactions in a network with a single bond and can therefore reduce the cohesive strength of a material and with it the HD. We assume that incorporation of H stemming from adsorbed H_2O is possible in (IIa), as the Al_2O_3 matrix forming in this sub-regime is hygroscopic[47,95] and under tensile stress. In comparison, the Si_3N_4 matrix in the Al-Si-N thin film system is less hygroscopic. Consequently, the hardness of the latter system is governed solely by the microstructural state of the film and not jeopardized by a H-induced weakening of the chemical bonds. In (IIb), the HD values of the Al-O-N system increase back to a level of 20-25 GPa. We attribute this to the compressive stress in this sub-regime which may prohibit H incorporation. In fact, no H was detected for films in this sub-regime.
In regime (III), HD values decrease to around 15 GPa. Towards the oxidized side of fig. 3.6, Al-O-N coatings approach the value reported for sputter deposited amorphous Al_2O_3 of 11.5 GPa[80].
In contrast to the HD, the Young's modulus, E, shows no dependence on the H incorporation in (IIa). E in Al-O-N coatings decreases continuously from 300 to 200 GPa as the O content increases from 0-40% over all three microstructural regimes.

AlN, Al_2O_3 and Si_3N_4 and also stoichiometric mixtures of these binary systems such as transparent Al-O-N, Al-Si-N and Al-Si-O-N are known to be widely chemically and thermally inert. In addition, materials with an increased O content are less prone to post-fabricational oxidation[101,155,17]. In order to test the thermal stability of the fabricated Al-O-N coatings, high temperature *in situ* X-Ray Diffraction (HT*is*XRD) was carried out for selected samples with O contents up to 16%. The tests showed a c-axis lattice parameter increase by 0.6% upon heating to 900°C due to the thermal expansion of the wurtzite lattice and full reversibility upon cooling. From this we conclude that the films are inert up to 900°C.

3.6 Quaternary Al-Si-O-N coatings

The XRD, TEM, and XPS results obtained on the Al-O-N system discussed above revealed a microstructural evolution of the system with increasing O content that is reminiscent of that observed for Al-Si-N system with increasing Si content described in earlier work[122,123,125] (fig. 3.4). We argued that the microstructural evolution in both systems is governed by the extra valence e^- that arises from e^- acceptor O replacing the N in the Al-O-N and from the e^- donor Si replacing the Al in the Al-Si-N systems. We thus expect that these mechanisms would also be present in the quaternary Al-Si-O-N films and that the boundaries between the regimes would be defined by the sum of the O and Si content. The data obtained on the quaternary system, however, reveals that this is not the case (see supplementary material). We attribute this to the formation of Si-O bonds in the quaternary system, which is in competition with the replacement processes of the e^- donor Al by Si and of the e^- acceptor N by O. These latter processes drive the V(Al) formation and microstructural evolutions of the Al-Si-N and Al-O-N systems.

Similarly to Al-O-N and Al-Si-N, the valences of the involved elements strictly define the stoichiometry for transparent Al-Si-O-N. The stoichiometry of such films is given by $AlSi_xO_{y=1.5+2x-1.5z}N_z$ with $z_{max} = 1 + \frac{4}{3}x$ for $y = 0$. This can be derived from a mixture of the binary stoichiometries AlN, Al_2O_3, Si_3N_4 and SiO_2 and was confirmed by ERDA/RBS for the Al-Si-O-N coatings fabricated for this study. As in our earlier work[122,123,125], an additional Si target was used in the sputter deposition system to fabricate the quaternary Al-Si-O-N films. The Si content in the coatings was varied from 0-20% through the power on the Si target during the R-DCMS process.

In the quaternary system, the residual stress σ shows no dependence on either Si or O, such that all films exhibit moderately compressive stresses of around -0.3 GPa. This suppresses the formation of cracks in all Al-Si-O-N coatings independent of their chemical composition. Furthermore, Al-Si-O-N films show no significant H incorporation and thus no dip in the hardness HD. We observed that

the HD of Al-Si-O-N depends only on the O, but not on the Si content. In Al-Si-O-N coatings of low O content, the HD is with 23-27 GPa slightly higher than that of Al-O-N, and decreases linearly to ∼8 GPa for Al-Si-O-N coatings containing around 65% O. Concomitantly with HD, the Young's modulus E of Al-Si-O-N decreases linearly from 250 to 150 GPa with O increasing up to 65%. For high O contents, Al-Si-O-N shows similar HD and E values as glass consisting of amorphous SiO_2, which has a HD of ∼8 GPa and an E of ∼75 GPa[8]. This suggests a structural similarity between Al-Si-O-N with low N content and glass, possibly arising from a large number of Si-O bonds. The advantageous mechanical proper-

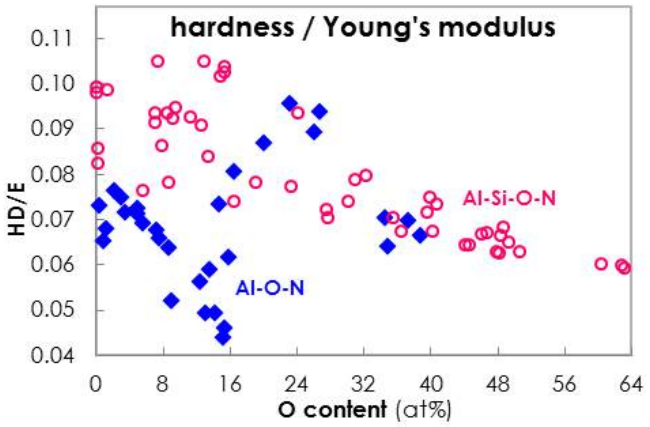

Figure 3.7: Evolution of HD/E (hardness divided by Young's modulus) of Al-O-N (blue rhombi) and Al-Si-O-N (open red dots) coatings plotted versus O content.

ties of protective coatings are often quantified by the HD/E coefficient (hardness divided by Young's modulus)[94]. The higher the HD/E value, the more resilient, tough and fracture resistant a coating is. Fig. 3.7 shows HD/E against O content for the Al-O-N and Al-Si-O-N systems. While HD/E is similar for Al-O-N and Al-Si-O-N of high O contents, Al-O-N shows a dip in HD up to 16% O. In this O content range, Al-Si-O-N clearly shows improved mechanical properties with an HD/E up to around 0.105. However, in the range of 16-30% O, Al-O-N has better HD/E values around to 0.095.

3.7 Conclusions

Transparent thin films of Al-O-N and Al-Si-O-N with different O and Si contents were fabricated by R-DCMS. The structure, morphology, hardness HD, Young's modulus E and stress state σ of these coatings, the chemical states and bonding of the constituents were analyzed as a function of the O and Si content. We found that O addition to wurtzite induces the same microstructural evolution as Si addition, as both species lead to an e^- excess. This commonality allows a general material evolution model to be proposed for both Al-O-N investigated in this study and Al-Si-N discussed in prior work[122,123,125]. In this evolution model, three regimes are distinguished by the O or the Si content: A crystalline solid solution regime (I), a nanocomposite regime (II) and an amorphous solid solution regime (III).

Microstructural tuning in thin films of the Al-Si-O-N system is therefore achievable by adjusting the chemical composition of the coatings through the sputter deposition conditions. In future work, the R-DCMS may be used to fabricate coatings with vertical gradients. This could, for example, be achieved through a change of the sputter power on each of the targets or by changing the gas flow during deposition. The possibility of microstructural tailoring within gradient layers provides a powerful methodology for the design of coatings for specific applications. At the substrate-film interface, for example, the mechanical properties of an Al-(Si-)(O-)N coating can be adapted to those of the substrate through HD and E. If the coating shall provide *e.g.* a diffusion barrier, a nanocomposite under moderate compressive stress and without open grain boundaries can be chosen for the bulk of the film. Towards the surface of the coating, the O content can be increased to obtain stability and inertness against post-depositional oxidation, or decreased to obtain a scratch-resistant coating with a high HD.

Preliminary experiments have shown that additionally, the refractive index n can be varied over a large range in fully transparent Al-(Si-)(O-)N coatings. Our future work therefore focuses on the tuning of the optical properties, together with the optimization of the microstructurally governed coating properties reported here. Preliminary results reveal good candidate material systems for protective, antireflective coatings.

Acknowledgments

The Swiss National Science Foundation [project Nr. 200021_150095] and Empa are acknowledged for the financial support. Cordial thanks go to Max Döbeli and his coworkers from the LIP at ETHZ for RBS and ERDA measurements and evaluations, and to Yucheng Zhang for TEM imaging.
Declarations of interest: None.

4 Al vacancies in Al-O-N investigated by *ab initio* Density Functional Theory

4.1 O and Si in wurtzite induce V(Al)

As reported in section 3.3.1, the incorporation of O as well as that of Si into wurtzite cause a shrinkage of the crystal lattice in the crystalline solid solution regime (I) (fig. 3.4). At first sight, however, it is not evident that these two incorporations induce the same phenomenon, because O and Si instigate substitutions of opposite chemical nature in wurtzite. As explained in chapter 3, O with its high Pauling electronegativity χ_O of 3.5 replaces the e^- acceptor N with a χ_N of 3.0, while Si with its low χ_{Si} of 1.8 replaces the e^- donor Al with χ_{Al} of 1.5[183]. O(N) and Si(Al) substitutions take place in different positions within the wurtzite structure: The former in anionic and the latter in cationic lattice sites. This difference is illustrated in fig. 4.1, which schematically shows an O(N) (top) and a Si(Al) (bottom) replacement in sub-units of AlN.

While the two types of replacements differ in their locations, however, they both impose an extra e^- on the structure (as mentioned in chapter 3): O has the electronic configuration $2s^2p^4$ and thus six valence e^-, while the replaced N with $2s^2p^3$ has only five, and Si $3s^2p^2$ has four valence e^-, while the replaced Al with $3s^2p^1$ has only three. The result is an e^- excess in the final Al-Si-O-N structure on the right in fig. 4.1 for both cases.

Former theory work of our group addressed the role of this extra e^- in the Al-Si-N system[129]. *Ab initio* Density Functional Theory (*ai*DFT) calculations were per-

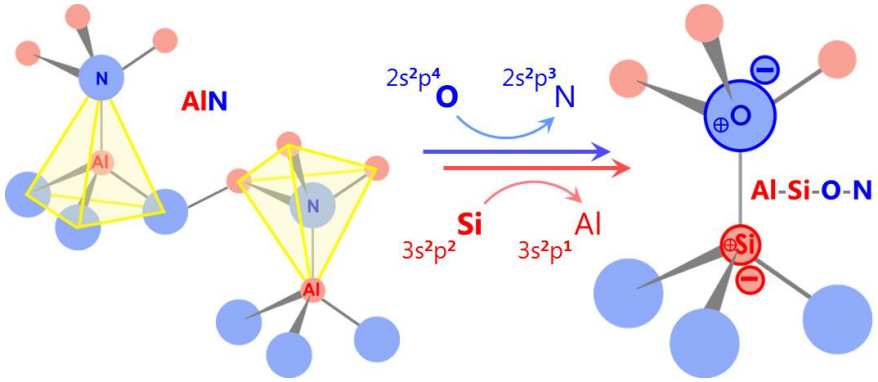

Figure 4.1: O(N) (top, blue) and Si(Al) (bottom, red) replacements in wurtzite. Both substitutions lead to an e^- (right). N and Al are both tetrahedrally coordinated by species of the other element, as highlighted by yellow pyramids (left).

formed for a supercell of wurtzite, into which increasing concentrations of Si were incorporated by substituting Al. The result of these calculations yielded a lattice expansion due to the repulsive Coulomb forces arising from the extra e^- of Si compared to the replaced Al. This calculated wurtzite lattice expansion was in clear contradiction to the experimentally observed lattice shrinkage. It was therefore hypothesized that each three extra e^- from Si were compensated by one V(Al). Upon introducing these V(Al) into the wurtzite supercell, the DFT calculations yielded a lattice shrinkage congruent to that measured with XRD experiments, clearly corroborating the hypothesis of V(Al) formation.

As a lattice shrinkage is also measured experimentally in Al-O-N of the crystalline solid solution regime (I) with increasing O content up to 8% (section 3.3.1), it can be proposed that the extra e^- in Al-O-N upon replacing N by O as well leads to V(Al) for compensation. This is tested with DFT calculations for an Al-O-N wurtzite supercell in this chapter. In addition to cell lattice parameters, the DFT calculations provide the enthalpy (H) changes upon defect generation. H will be combined to the entropy (S), approached with a combinatorial model, in order to obtain the Gibbs Free Energy (G) and thus an estimate on the thermodynamic stability of wurtzite grains containing O and V(Al).

A simplistic model as in fig. 4.1 shows that through a rearrangement of the e^-, the octet rule, followed by main group elements such as Al, Si, O and N, and

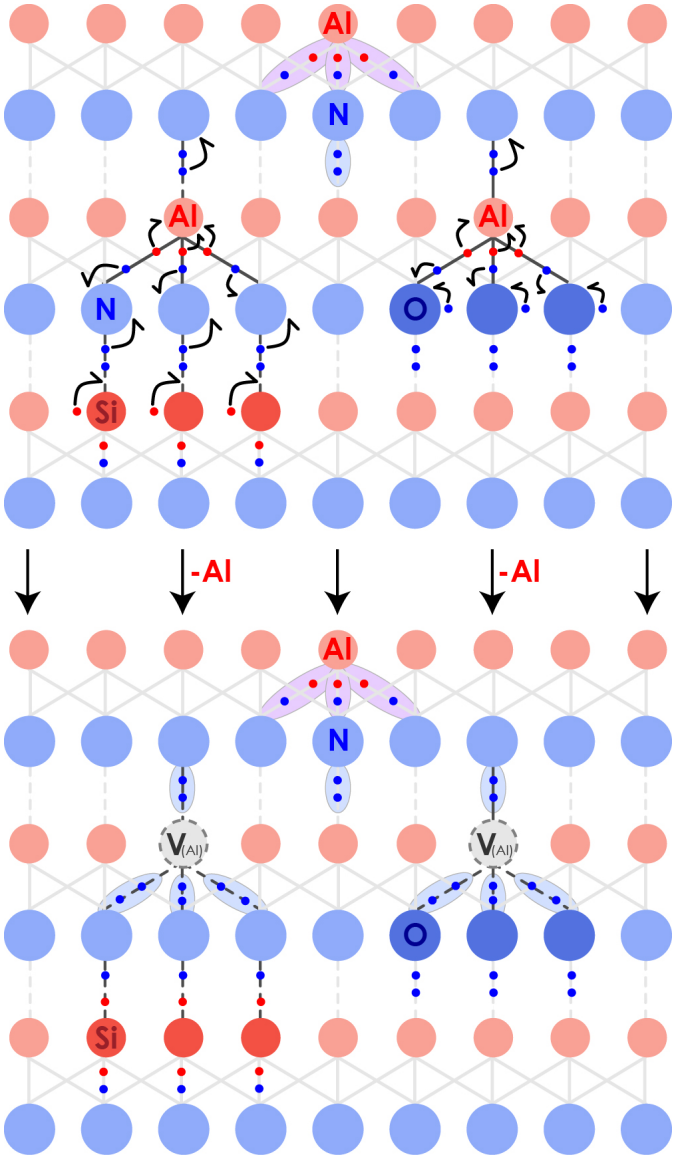

Figure 4.2: Model of the electronic rearrangements of the excess e^- from O(N) and Si(Al) substitutions in wurtzite. At the top, the bonding interactions in pure AlN are shown, with the e^- originating from Al in red and those from N in blue. To the left, three Si (darker red) substitute three Al, and on the right, three O (darker blue) substitute three N. e^- rearrangements are indicated with half-arrows. Both substitutions lead to V(Al) (bottom), which allows fulfilling the octet rule through the same electronic structure in both replacement cases.

therefore the electronic balance can be maintained upon introducing V(Al) both for Si and for O incorporation. The 1:1 stoichiometry in AlN facilitates this e^- rearrangement, as e^- donors in wurtzite are only coordinated to acceptors vice versa. Therefore bonds always connect donors and acceptors, and extra e^-, irrespective of whether they originate from the donor or acceptor, can be shared and relocated in neighboring bonds or e^- lone pairs. In fact, the e^- donor and acceptor sub-lattices in wurtzite are crystallographically equivalent, as highlighted by yellow pyramids in fig. fig. 4.1: Each N is tetrahedrally surrounded by only Al, and vice versa each Al is tetrahedrally surrounded by only N in wurtzite.
For clarity, the Si(Al) and O(N) replacements in the model in fig. 4.1 are grouped around one V(Al), which is not expected to occur in reality due to increased electrostatic repulsion upon high local charge densities. A more realistic distribution of the defects will be covered by the DFT calculations.

4.2 Vacancies in further materials

Other material systems have been reported to form vacancies due to the incorporation of alio-valent elements. One example is cubic Yttria Stabilized Zirconia (YSZ)[56]. In contrast to Al-O-N and Al-Si-N, where vacancies in cationic lattice positions form due to an e^- excess induced by O and Si, YSZ contains vacancies on anionic lattice positions, as Y provides less e^- than the Zr it replaces. Recently, it was reported that understoichiometric cubic zirconia could be stabilized binarily without the addition of Y, but by an O deficiency induced through the sputter deposition process used[132]. Further binary systems have been reported in the literature that experience a stabilization through vacancy formation. Examples of this are the low temperature form of Ta_2O_5[161] or the cubic form of Y_2O_3. In the latter, the CaF_2 structure is not formed but instead that of bixbyite, which reduces cation coordination from eight to six leaving two of the eight positions of the coordination cube unoccupied[58]. For Al-O-N, V(Al) formation has been reported for O contents up to 0.75% in single crystals of wurtzite[151,153,59].

4.3 DFT calculations to assess V(Al) in Al-O-N

The calculations were performed by Dr. Carlo Pignedoli, Dr. Daniele Scopece and Dr. Daniele Passerone from the Empa nanotech@surfaces Lab205. Part of the description of the modelling work discussed in this section has been adapted from a paper draft written by D. Scopece and C. Pignedoli. The approach introduced for Al-Si-N[129] was followed, improved by the use of a larger simulation cell and a PBE exchange correlation functional[126]. The atomistic models were based on an orthogonal supercell of wurtzite AlN corresponding to 48 units of the primitive hexagonal cell, yielding a total of 192 atoms in the case of pure, defect-free AlN. The large cell was chosen to investigate the relevant range of O concentration as well as different defect geometries for each concentration. The DFT calculations[65] were implemented according to the mixed Gaussians-plane-wave approach in the code CP2K[69]. The electronic core-valence interactions were described by norm-conserving pseudopotentials[53]. For each geometry considered, the equilibrium lattice parameters were computed imposing zero pressure on the system and optimizing the internal coordinates until the atomic forces were smaller than $\sim$0.01 eV/A. To create atomic models for the different O concentrations, AlN was used as starting point and O atoms were included substituting N atoms (O(N)). Two opposite defect geometries were considered for each concentration: O(N) incorporated in nearest neighbor sites, termed "close", and O(N) maximally diluted without neighboring substitutional sites, termed "far". The supercell allowed the uptake of more than 20 O atoms in the diluted configuration, corresponding to an O concentration range spanning from 0 to $\sim$11%.

To accommodate the excess e^- from O in the wurtzite supercell, (i) one V(Al) was introduced per three O(N)[160]. The resulting V(Al) is able to act as an e^- acceptor (fig. 4.2). For comparison, two alternative scenarios were tested. In the first (ii), the excess e^- were removed artificially by charging the cell positively and the background negatively by the same absolute value[86]. This scenario was included to mimic a non-specific e^- excess compensation mechanism. In the second (iii), the e^- excess induced by O was not compensated for; the e^- were left as free e^- on O.

4.4 DFT calculations in comparison to experimental results

Fig. 4.3 shows the change in the c lattice parameter in wurtzite upon incorporation of O. The value for pure wurtzite (c_0) is subtracted from all calculated and measured values (c). The experimental data derived from XRD measurements (as also plotted in fig. 3.1a)) is shown with blue rhombi. A lattice shrinkage by approximately -0.003 nm is found for Al-O-N containing 8% O, and no further c lattice parameter change is seen for higher O contents (section 3.3.1). The calculated data including (i) V(Al) generation, shown with bright blue squares, is in good agreement with the experimental trend. The scatter in the calculated data is the result of the different configurations (positions of the O(N) and V(Al) inside the supercell) tested. Further data points originate from calculations for scenarios

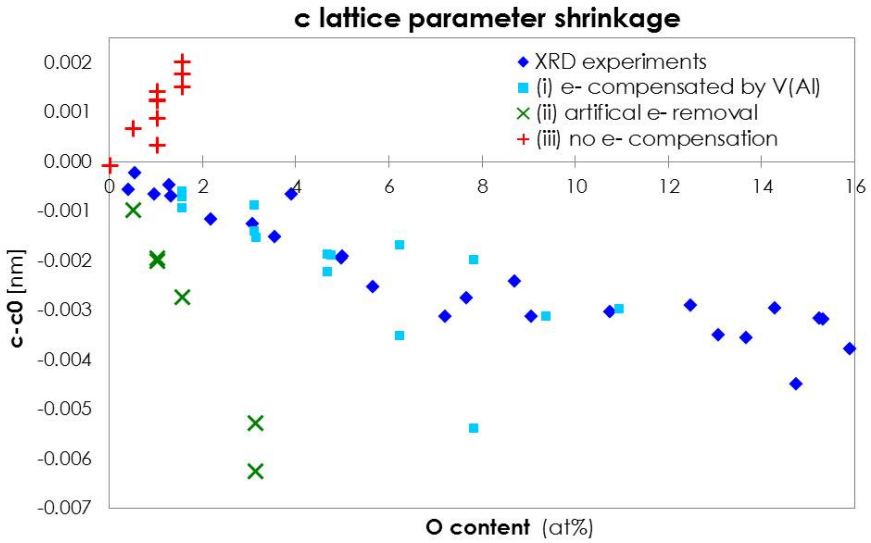

Figure 4.3: Changes in the c lattice parameter (c-c_0) [nm] of wurtzite upon O incorporation. Experimental data points (blue rhombi) and *ai*DFT data points upon (i) V(Al) generation (bright blue squares), upon (ii) artificial e^- removal (green crosses) and upon (iii) no e^- excess compensation (red plus signs) are shown.

other than V(Al) generation during O introduction into wurtzite. Data points calculated (ii) after removing excess e^- from O artificially from the supercell and compensating for the resulting charge in the background are shown with green

crosses. The lattice shrinkage is about -0.006 nm, twice as strong as that observed experimentally. A possible explanation for this is that the extra positive charge of the O nucleus increases the attractive force on the neighboring atoms, while the homogeneously distributed background charge does not apply a force on the unit cell.

Data points calculated (iii) without compensating for the additional e^- of O

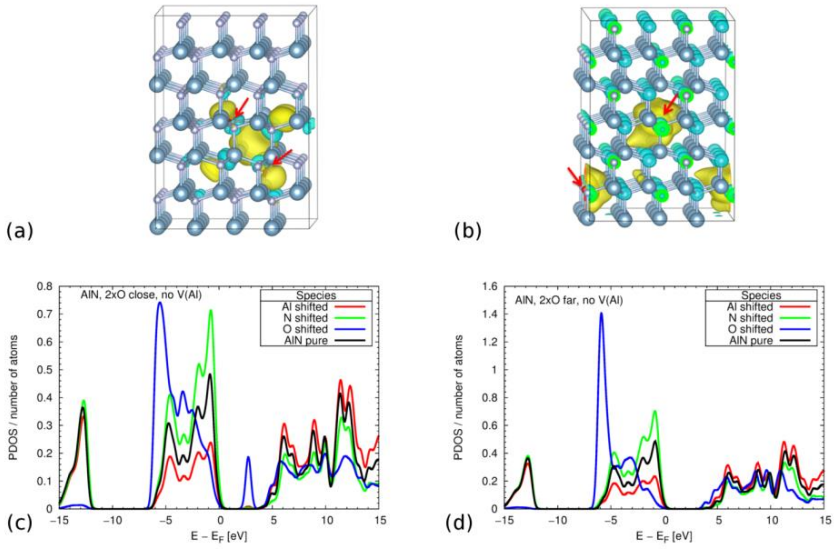

Figure 4.4: MOs (a), b)) and DOS (c), d)) of Al-O-N supercells containing ∼1% O (red arrows). The MOs are shown with an isovalue of 0.0188 and 0.0164 e^-/Bohr^3, corresponding to the HOMO level. The DOS are broadened with a Gaussian function with standard deviation of 0.25 eV divided by the number of atoms. The total DOS of the defected structures are shifted to overlap with the pure, defect-free AlN shown for comparison. The shift amounts +2.75 eV in c) and +3.90 eV in d) to take into account different Fermi energies from the O-doped systems.

are shown with red plus signs. In opposition to the experimental observation, a lattice expansion is obtained. We attribute this to the Coulomb repulsion arising from the extra charge density. Apart from the increased Coulomb energy that destabilizes the unit cell, such excess charge could also diffuse or hop through the crystal which would lead to some electrical conductivity. All Al-O-N coatings were however found to be electrically insulating. To examine this scenario (iii) in de-

tail, a close and a far configuration were investigated for a supercell containing two O(N), *i.e.* for $Al_{96}N_{94}O_2$ corresponding to Al-O-N with an O content of ∼1%. Fig. 4.4 shows the molecular orbitals (MOs) (a), b)) and the density of states (DOS) (c),d)) for the close (a), c)) and the far (b), d)) configuration of this supercell. In the MOs for the close configuration (fig. 4.4a)), where the two O (red arrows) are in neighboring anionic lattice sites, the charge is more localized compared to the far case (fig. 4.4b)). This difference is reflected in the scatter of the red plus sign data points (iii) in fig. 4.3 for 1% O in Al-O-N. The DOS of the close configuration (fig. 4.4c)) shows an additional state in the band gap occupied by excess e^-; this state is not seen in the far configuration (fig. 4.4d)).
In summary, it can be concluded that the c lattice parameter calculations shown in fig. 4.3 support the hypothesis of (i) V(Al) formation upon incorporation of O into wurtzite and contradict other tested e^- compensation mechanisms, reminiscent to the case of Al-Si-N[129].

4.5 Enthalpy obtained from DFT

When investigating the different possible configurations for (i) V(Al) formation, one configuration, termed "smart", was observed to be energetically particularly favored. The MOs for the smart configuration are shown in fig. 4.5. Here, two O(N) sites are close to each other as well as close to the V(Al) that accommodates the e^- density of the O atoms, while the third O(N) is far to dilute the electronic imbalance.

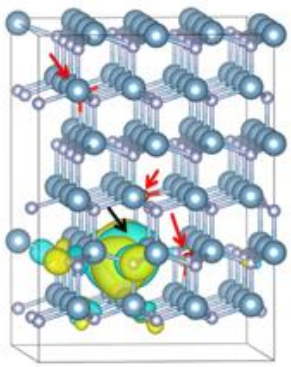

Figure 4.5: Electronic isovalue of the HOMO state of the smart structure.

To compare the stability of different scenarios, the defect formation enthalpy for different O concentrations and different configurations in Al-O-N for (i) V(Al) formation and (iii) no excess e^- compensation are plotted in fig. 4.6. The formation enthalpies were computed according to *ab initio* thermodynamics[57,45] as

$$H(\text{defected}) - H(\text{defect-free}) - n(O)\mu(O) - n(Al)\text{-}\mu(Al) - n(N)\text{-}\mu(N)$$

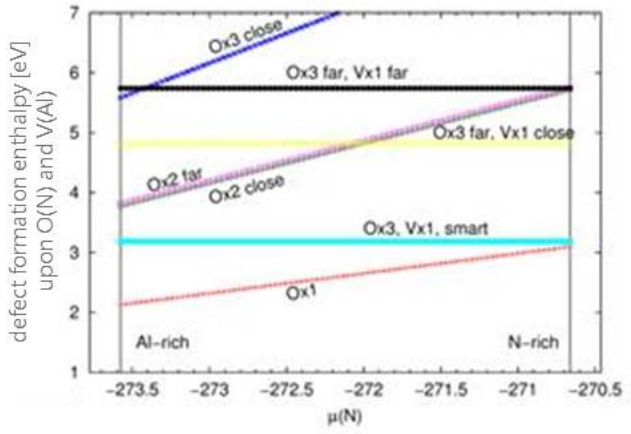

Figure 4.6: Formation enthalpies [eV] of some defects as a function of the chemical potential μ(N) [eV].

where n(X) is the number of atoms of species X, μ(X) is the chemical potential of species X and thermodynamic equilibrium with bulk AlN and bulk Al_2O_3 is assumed. The flat curves in fig. 4.6 correspond to the systems (i) containing V(Al) which have an exact stoichiometry mixture of AlN + Al_2O_3, while the curves with a positive slope correspond to systems (iii) without excess e^- compensation.

Upon increasing O content, (iii) without excess e^- compensation is less stable than (i) V(Al) generation. For a μ(N) of -272 eV, for example, the (i) smart configuration containing three O(N) and one V(Al) requires 2 eV of formation energy less than a configuration (iii) without excess e^- compensation containing only two O(N).

In order to study the dependence of the stability of different distributions of O(N) and V(Al) inside the supercell on O concentration, the dissociation enthalpy (H_{diss}) of Al-O-N containing (i) V(Al) into AlN + Al_2O_3 is calculated, as plotted in fig. 4.7. It is negative for all configurations with a decreasing stability for higher O concentrations. Further, configurations with larger distances between O(N) and V(Al) are less stable for all O concentrations. This suggests that the three extra valence e^- contributed by three O are in close vicinity to the V(Al) which compensates the excess valence charge. Note that for a negative dissociation enthalpy the thermodynamically stable state consists of pure AlN crystallites embedded in an Al_2O_3 grain boundary phase, but not in a solid solution of O inside the AlN grains. Considering the dissociation enthalpy here, the stability of the solid solution even decreases for increasing O contents. However, the existence of a solid solution is experimentally confirmed (section 3.4). We identify two possible scenarios to re-

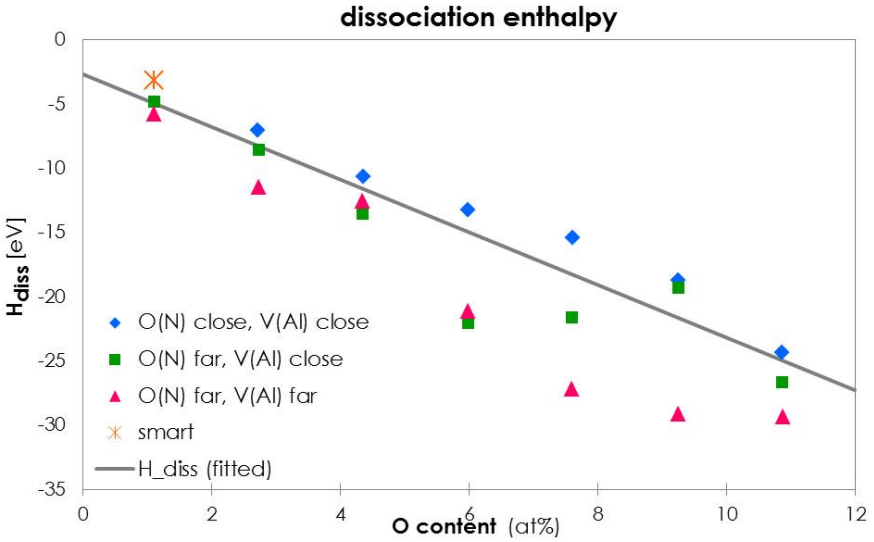

Figure 4.7: Dissociation enthalpies [eV] for Al-O-N $\rightarrow$ AlN + Al_2O_3 in systems with (i) V(Al) generation upon O incorporation. Different close/far configurations are given: O(N) close and V(Al) close (blue rhombi), O(N) far and V(Al) close to some O(N) (green squares), O(N) far and V(Al) far (red triangles) and the smart configuration (orange cross). The most probable first and second case are combined in the linear fit H_{diss} (gray line).

solve this apparent contradiction. Firstly, a sputter-deposited film may be locked in a metastable state. Secondly, only the zero-temperature enthalpy of the system is accessible by DFT, whereas the Gibbs free energy G, not the enthalpy H alone determines the thermodynamical stability of the system. For G, the system entropy S must be considered, which becomes of importance particularly at higher temperatures or when local energy is provided by the impact of ions during the sputter process. A system with an arbitrary distribution of O(N) and V(Al) inside the AlN crystallites has a higher entropy compared to that of pure AlN. Such a mixing entropy could thus lead to an entropic stabilization of the solid solution state. Entropy stabilization has recently gained attention in the literature. Alloys[173] as well as ceramics[138] stabilized by entropy have been reported on. In the following, the possibility of entropy stabilization is tested for Al-O-N thin films.

4.6 Calculation of the mixing entropy

The entropy of a system is defined as

$$S = k_b \cdot \ln(\Omega) \ ,$$

where k_b is the Boltzmann constant with a value of $1.38064852(79)\cdot10^{-23}$ J/K, ln is the natural logarithm and Ω is the number of microstates that a system can adopt. A simple combinatorial approach was followed here to obtain an estimate for the entropy of the wurtzite Al-O-N system upon O(N) incorporation and V(Al) generation. The number of microstates can be defined as the number of arrangement possibilities, which is given by combinatorics as

$$\Omega = \log\left(\underbrace{\binom{N}{k}}_{=\,\Omega_O} \cdot \underbrace{\binom{N}{k/3}}_{=\,\Omega_{V_{Al}}}\right)$$

This bracket notation means, for example, (N low k) = N! / ((N-k)!), where N is the total number of anionic plus cationic lattice positions, k is the number of O atoms incorporated, and k/3 is the corresponding number of V(Al) generated. Ω_O therefore is the number of possibilities to distribute the O atoms, *i.e.* the number of possible microstates of the anionic sub-lattice, while Ω_{Al} is the number of possibilities to distribute the V(Al), *i.e.* the number of possible microstates of the cationic sub-lattice. Fig. 4.8 illustrates the calculation principle on the basis of a small crystal cell of 18 anions and 18 cations, which shall represent AlN. For simplicity, a trivial 2D rock salt structure is shown instead of that of 3D wurtzite, which does not influence the result here, as only the 1:1 stoichiometry of anionic and cationic positions is important.
On the left, a defect-free structure is shown; 18 N (blue) are sitting in anionic positions and 18 Al (red) in cationic positions. Only one microstate can be adopted, thus Ω=1. In the middle figure, one O(N) is incorporated corresponding to 2.8% O in Al-O-N with no V(Al). There are already 18 possibilities to place the O in

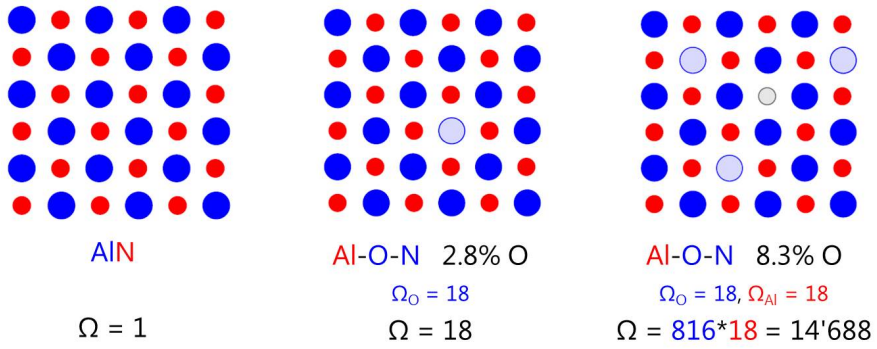

Figure 4.8: Possible microstates Ω in Al-O-N upon O increase. 18 anionic lattice positions (blue) and 16 cationic ones (red) are shown. O(N) is shown in bright blue, V(Al) in bright gray.

any of the anionic sites. On the right, 3 O(N) plus one V(Al) are incorporated, yielding Al-O-N with 8.3% O, thus close to the solubility limit of O in wurtzite detected in this project. This leads to 816 possibilities to distribute the O(N) in anionic sites and 18 possibilities to place V(Al) in a cationic site. Ω is given by the product of the two numbers, amounting to 14'688 possible microstates. S as a function of Ω thus increases significantly for an O increase from 0 to 8%.
To estimate the entropy S in the Al-O-N films deposited for this project, the calculation above was carried out for a supercell of 192 atoms as used for the *ai*DFT calculations.

4.7 Thermodynamic stability of Al-O-N

The change in the Gibbs free energy ΔG is given by

$$\Delta G = \Delta H - T\Delta S \ ,$$

where ΔH is the enthalpy calculated by DFT, T is the temperature, and ΔS is the entropy difference between the solid solution and phase-separated state. While the entropy of the solid solution state can be obtained from the mixing entropy *Ansatz*, the assessment of the entropy of the phase-separated state remains challenging. In a first approach we set it to zero.

The difference of the Gibbs free energy (purple) is plotted in fig. 4.9, together with -TΔS (pink) and the association enthalpy ΔH_{ass}. The latter describes the formation enthalpy of the solid solution and is equal to the negative dissociation enthalpy (fig. 4.7). For a T of 2000 K, the Gibbs free energy difference remains

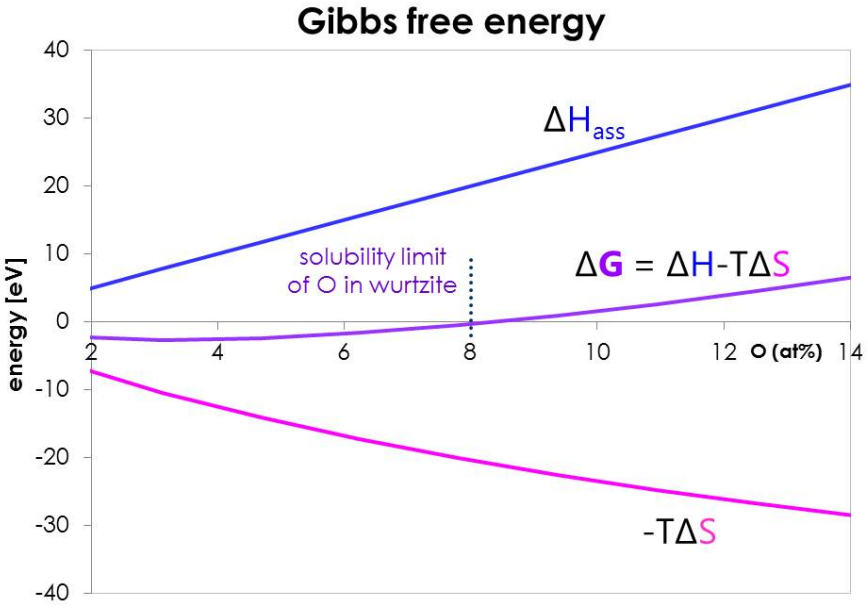

Figure 4.9: Association Enthalpy H_{ass} (blue), entropy S (pink) and Gibbs free energy G (purple) [eV] for supercells of Al-O-N with up to 14% O at 2000 K.

negative for O concentrations below 8%, which is the experimentally determined solubility limit of the system (section 3.3.1). Note that T=2000K was chosen such that ΔG=0 at 8% O content. Energies compatible with such a temperature could however be reached at the surface of a sample during sputtering through the impact of high energy particles. Because sputtering is a process far off thermal equilibirum, the sample could have been locked in its high-temperature entropic energy configuration.

It can thus be hypothesized that Al-O-N films consisting of a wurtzite solid solution are entropy stabilized up to 8% O during the sputter process, which corresponds to an equilibrium T of 2000 K, but that they are metastable after the process at room T. Even at elevated temperatures up to 900°C (fig. 7.9), no phase segregation was observed.

4.8 Entropy in Al-O-N assessed experimentally

To test this hypothesis, two experiments[138] were carried out. For both experiments, Al-O-N films containing 8% O deposited onto amorphous Al_2O_3 wafers were heated to a high T up to 2000 K and thermally equilibrated. At this high T, entropy becomes important and is, based on our calculations (fig. 4.9), expected to stabilize a solid solution of wurtzite with O(N) replacement sites and V(Al).

In the first experiment (1), the samples were cooled slowly down to room T. It was expected that the system would remain in thermal equilibrium during the cool-down, as enough time was provided at each T. Therefore, the entropic energy was expected to go from a high-energy state to a low-energy state. Entropic energy at room T is negligible. Hence O was expected to diffuse out of the crystallites, such that crystallites of pure AlN remained.
In the second experiment (2), the samples were quench-cooled quickly down to room T. It was expected that the system would not remain in thermal equilibrium, as not enough time to reach the latter during any stage of the cool-down was provided. Therefore, the entropic energy was expected to remain locked in a high-energy state, and O was expected to remain in the crystalline wurtzite solid solution.

The experimental control of the state of the crystalline wurtzite phase was achieved by XRD, with which the samples were measured before as well as after the experiment. Before the experiment, all samples exhibited the wurtzite (002) peak at around 36.3° in 2θ, the position of Al-O-N wurtzite crystallites with 8% O and therefore a c lattice parameter of 0.495 nm (fig. 3.1). After the experiment, the (002) peak of coatings in which O was expected to have diffused out of the crystallites due to the low-energy entropy state (experiment 1, slow cooling) was expected to be found at around 36.1° in 2θ, the position of pure AlN wurtzite crystallites. The (002) peak of coatings in which O was expected to have remained in the crystallites due to the high-energy entropy state (experiment 2, shock-cooling)

was expected to remain at around 36.3° in 2θ, the position of Al-O-N wurtzite crystallites with 8% O.

As a high T up to 2000 K is difficult to reach experimentally, two heating/cooling procedures were applied for both experiments (1 and 2). For the first version, the samples were heated *in vacuo* by an e^- beam generated from a tungsten (W) filament through which a current was applied. To direct the e^- beam towards a sample, the Al_2O_3 wafer carrying the film was coated with 200 nm tantalum (Ta) on the backside. With an increasing current through the W filament, the sample was heated to approximately 1800 K within 3 h and equilibrated at that T for 20 min. T was controlled with a pyrometer through a view port. For the slow cooling (experiment 1), the current through the W filament and thus the e^- beam onto the sample were reduced to zero over 20 min. For the quench-cooling (experiment 2), the current was stopped abruptly so that the sample stopped glowing immediately. For the second heating/cooling version, the samples were heated in an Ar-flooded oven. T inside the oven was brought to 1873 K within 3 h and equilibrated at that T for 6 h. T was controlled by the software of the oven and cross-checked with a pyrometer through the opening of the oven. For the slow cooling (experiment 1), the oven with the samples inside was cooled to room T over 22 h. For the quench-cooling (experiment 2), the samples were taken out of the oven to atmospheric conditions.

The results of heating/cooling experiments are shown in fig. 4.10, for a) a slow cooling (experiment 1) and b) a shock-cooling (experiment 2; performed with fresh samples), in both cases for a heating to ∼1800 K with an e^- beam. Both experiments (1 and 2) were repeated several times by both heating methods and were found to be reproducible, such that the data in fig. 4.10 is representative for all experiments performed. Diffractograms recorded before the heating/cooling are shown in blue, those recorded after in red.

In fig. 4.10a) (experiment 1), the (002) peak in the blue diffractogram before the heating/cooling is found at 36.26° in 2θ, the position of Al-O-N wurtzite containing 8% O. After heating and a slow cooling, the peak in the red diffractogram is

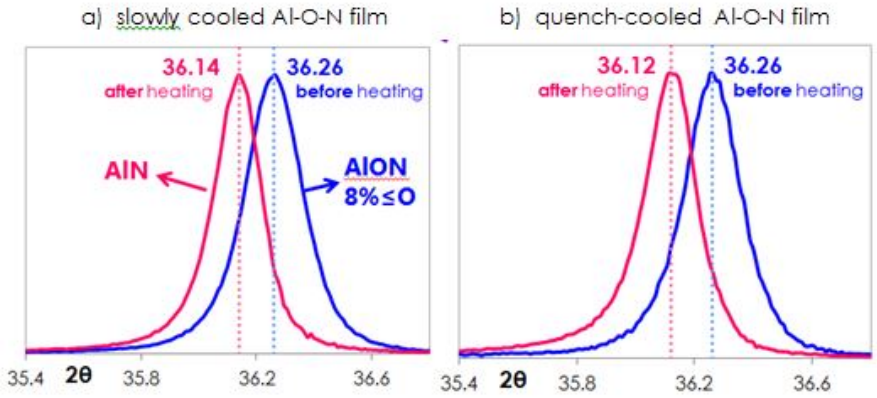

Figure 4.10: Diffractograms before (blue) and after (red) heating experiments for Al-O-N films containing 8% O that were a) slowly cooled and b) quench-cooled.

detected at 36.14°, the 2θ for pure AlN. The expectation of experiment (1) is thus met; O has diffused out of the crystallites. We attribute this to the low-energy state of the entropy in the crystallites, assumed by the system because of the slow cooling rate that allows continuous thermal equilibration.

In fig. 4.10b) (experiment 2), the (002) peak in the blue diffractogram before the heating/cooling is also found at 36.26° in 2θ. After heating and a rapid cooling, the peak in the red diffractogram is detected at 36.12°. This is the position for O-free AlN, which signifies that also during a fast quench-cooling, O has diffused out of the crystallites. The outcome of experiment (2) thus does not support our hypothesis on the entropy stabilization of 8% O in Al-O-N.

Both cool-down procedures clearly show a relaxation of the contracted lattice of the samples with 8% O to the normal lattice parameter observed for pure AlN. We thus conclude that the O has been driven out of the AlN crystallites for both cool-down procedures. These data do not support the hypothesis that the Al-O-N with 8% O is an entropy stabilized material. However, in our model used for the calculation of the entropy, the entropy of the solid solution state could be calculated, but that of pure AlN with O at the grain boundaries was assumed to be zero in a first approach. Clearly, entropy must play a role at least at higher temperatures. We thus argue that the entropy of the grain boundary phase (and O contained in the grain boundaries) must be higher than the mixing entropy.

Considering that the grain boundary phase consists of amorphous Al_2O_3, *i.e.* is not detected by XRD, supports this. Firstly, atoms in an amorphous network have a higher entropy than in a crystal as they do not assume well-defined crystal lattice positions, and secondly, an under-dense amorphous grain boundary phase contributes vibrational entropy.

We can thus conclude that the Al-O-N nanocomposite thin films consisting of Al-O-N crystallites containing up to 8% O embedded in an amorphous Al_2O_3 grain boundary phase obtained by R-DCMS are in a thermodynamically metastable state. Although this metastable state is quite inert, *e.g.* not changed by annealing for 1 h at 900°C (sections 3.5 and 7.9), O is driven out of the AlN crystallites when annealing to much higher temperatures, *e.g.* 1500°C, that are however not reached in most applications. We could further conclude that the grain boundary phase entropy must be higher than the mixing entropy of the solid solution phase. The thermodynamically stable state of Al-O-N thin films is thus a nanocomposite, in which wurtzite AlN grains with a low entropy are surrounded by an amorphous Al_2O_3 matrix having a high entropy.

5 Applications

The most valuable properties of the Al-(Si-)O-N system are the hardness and the optical transparency. While the focus of this project was clearly on the material evolution inducible through altering the chemical composition of the coatings, a few applications were tested in addition, as the coatings turned out to be highly interesting for those. The first group of applications in this study was those requiring hard, impact- and scratch-resistant coatings for protective purposes. The durability of Al-(Si-)O-N was therefore tested for coatings on Si(100) wafers and on Gorilla glass of the generations G3 and G5 (Corning, New York, USA)[25] and on polycarbonate (PC). The second group of applications of interest was optical coatings that suppress the appearance of undesired color effects on transparent substrates. Thirdly, the suitability of the coatings for decorative purposes was explored. As it is transparent, Al-(Si-)O-N can be used as a matrix for the inclusion of nanoparticles that act as color centers.

5.1 Protective coatings

5.1.1 On Si(100)

As transparent Al–(Si)-O-N coatings exhibit tunable mechanical properties such as the stress state σ, the hardness HD and the HD/E ratio as well as a tunable microstrucutre and good adhesion to substrates such as Si(100) and glass (sections 3.6 and 3.4), they can be proposed as good candidates for protective coatings. When crystallinity and a high HD are desired, coatings with low O contents out of the crystalline solid solution regime (I) can be chosen. When penetration of *e.g.* a corrosive such as O_2 through the coating shall be hindered, the nanocomposite regime (II) or the amorphous solid solution regime (III) are suitable, as in those,

σ becomes compressive and no open grain boundaries exist. When the coating shall be inert against post-depositional oxidation, the high O content regime (III) is advisable.

In order to test the performance of Al-O-N coatings in weathering conditions, four coatings deposited on Si(100) were exposed to open air on the rooftop of an Empa building for half a year during February-July 2016. Fig. 5.1 shows a photograph of the experimental arrangement. One crystalline coating with 1% O and thus close to pure AlN was selected, one coating with 5,7% O from in-midst regime (I), one with 14.3% O from regime (IIb) as such a coating is a compressively stressed diffusion barrier, and one with 49,7% O from regime (III) as such a coating undergoes little oxidation.

After the exposure time, no weather-induced damages such as delamination, cor-

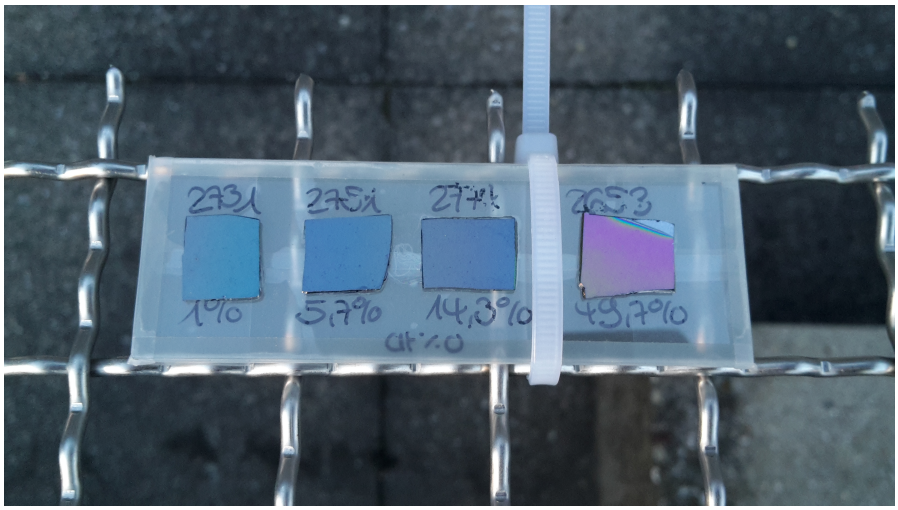

Figure 5.1: Al-O-N films on Si(100) exposed to weathering. Four samples containing 1.0%, 5.7%, 14.3% and 49.7% O were chosen (from left to right). The samples were glued onto a glass slide and fixed to a horizontal mesh with a cable tie. Exposure time was February-July 2016. The numbers on top of the samples are in-house experimental identifiers.

rosion, inclusions or fractures could be detected by eye nor by optical microscope. Pollution particles such as pollen or dust were easily removed with ethanol. This experiment shows that the Al-O-N films are inert against influences of atmospheric weathering conditions.

5.1.2 On Gorilla Glass G3 and G5

Gorilla glass is a tempered glass, hardened by the dissolution of sodium ions (Na^+) out of the surface and the replacement of those with larger potassium ions (K^+) in a hot salt ion-exchange bath. This exchange imposes compressive stress onto the Gorilla Glass surface, which is reported to render the Gorilla glass harder and more wear resistant[25]. Corning, producer of Gorilla glass, reports increased durability and improved drop failure for Gorilla glasses of advanced generations applied as mobile phone screens[26]. However, it is not indicated how the drop tests were performed, and customers often report immediate splittering of Gorilla glass mobile phone screens upon impacts onto corners and edges[51]. The probable reason for this is that due to the compressively hardened surface, Gorilla glass covers perform well against impacts perpendicular to the surface, such as in drop tests onto the front, but when the force impact is close to parallel to the glass surface, the latter shatters due to the high compressive surface strain.
In a joint project with an industrial partner, initial experiments were therefore performed to test whether Al-(Si-)O-N coatings of varying compositions on Gorilla glass of the generations 3 and 5 (G3 and G5) could reduce the shattering of the glass upon drops onto corners and edges. Preliminary feedback of the industrial partner is positive and suggests that this goal is achieved through the coatings, and that additionally, a higher hardness and better scratch resistance of the coated Gorilla substrates is obtained. However, the results of a thorough investigation are still outstanding. In case Al-(Si-)O-N coatings effectively increase the resilience of G3 and G5, two reasons for that can be suggested. Firstly, the hardness and toughness of the coatings (sections 3.5 and 3.6) may be beneficial. Secondly, it is possible that the RF cleaning of substrates, generally applied prior to coating depositions for glass and Si(100) substrates (2.2) and therefore also for G3 and G5 in these experiments, releases the surface compression induced by the ion exchange process during the fabrication of Gorilla glass.

5.1.3 On polycarbonate

Polycarbonate (PC) is a polymer that is inexpensive, lightweight and arbitrarily shapeable while maintaining optical transparency, and is therefore a material frequently used for *e.g.* eyeglass lenses. The disadvantage of PC in this application, however, is the low hardness of <1 GPa[42], which leads to scratches upon small force impact. PC could thus greatly profit from protection by a hard coating. However, a problem with very thin coatings on PC of low hardness is the "eggshell effect", which describes the observation that a thin coating on a soft substrate breaks easily due to lacking support. Possibly a hard coating could be applied on top of a conventional dip-fabricated coating to further increase the hardness.
In this project, for testing purposes, coatings of Al-(Si-)O-N were applied directly onto domed PC blanks for eye glass lenses and several difficulties were encountered. Firstly, PC has a low glass transition point of around 150°C[106]. Therefore, a deposition temperature of 200°C could not be used for PC. The deposition T of 200 °C was used for this project, as films deposited at lower T are reported to be of lower quality[122]. When a lower deposition T of 100°C was chosen, the PC substrates turned brownish, especially at the lens rims that were in contact with the substrate holder. Regions in the bulge of the lens, not touching the substrate holder and therefore expected to have experienced a lower T, turned less brownish. An excerpt of such a substrate coated with Al-(Si-)(O-)N at 100°C is shown in fig. 5.2c). A blank without coating, clearly less colored, is shown in a) for comparison. A brown tarnishing of PC substrates upon heat is a well-known phenomenon attributed to thermo-oxidative reactions including cross-linking at the polymer surface[46]. In order to test whether UV radiation from the plasma is a source for the embrowning, PC substrates were exposed to an RF plasma in Ar and to sunlight radiation on the Empa rooftop (as the samples in fig. 5.1) for a period of three months. These treatments did, however, not lead to coloring, and UV radiation was therefore excluded as the reason for the brown tarnish.
Another problem encountered was the formation of cracks in the coatings after deposition, as visible in the photo of a side view onto a coated lens under lab light in fig. 5.2d) (not visible in the top views a)-c)). Cracks in Al-(Si-)(O-)N occurred irrespective of whether the samples were removed from the deposition chamber

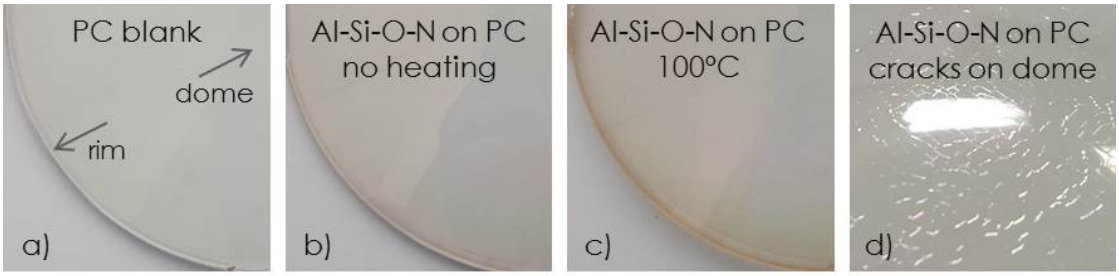

Figure 5.2: Photographs of sections of PC eyeglass lenses, a) blank, b) coated with Al-Si-O-N without heating, c) coated with Al-Si-O-N at 100°C, and d) a section of an Al-Si-O-N coated dome exhibiting cracks, particularly visible in a side view under lab lights. The coated lenses show a brown tarnishing, more intense for higher deposition T and towards the lens rims.

immediately after the deposition and thus not fully cooled, or after a cooling inside the vacuum chamber. However, in the latter case, crack formation took place more slowly. It can be postulated that these cracks are the result of the difference in the thermal expansion coefficients of the PC substrate ($3{\cdot}10^{-4}$ °C^{-1} [106]) and Al-(Si-)(O-)N ($5{\cdot}10^{-6}$ °C^{-1} [189]): PC contracts more strongly upon cooling and may thus lead to damages in the coating. Also, the changes in mechanical properties on cooling will occur at a different rate in the two materials, with the PC remaining softer for longer. Tests were carried out to determine whether the problems of embrowning and crack formation could be avoided by reducing the deposition T further in processes by not actively heating. The PC substrates coated with Al-(Si-)(O-)N without heating, depicted in fig. 5.2b), indeed showed less damage, but a lower degree of browning and a slower crack formation still occurred. This suggests that the brownish coloring of PC upon application of a coating arises, in addition to from heat, from the interaction of the PC surface with the coating in the form of chemical reactions and/or deformations. While films on PC substrates coated without heating were mostly crack-free immediately after the deposition process, crack formation started within hours and progressed over several days upon exposure to atmosphere. This may be due to oxidation processes at the interface or chemical changes at the surface due to contaminants from the atmosphere as seen in environmental stress cracking[113]. Therefore, if Al-(Si-)O-N is to be applied on PC by R-CFDC-MS, further research and optimization is needed.

5.2 Optical coatings

Transparent protective coatings are important to enhance the durability and lifetime of optical devices such as *e.g.* camera lenses and screens of mobile phones (section 5.1). Al-(Si-)O-N with optical transparency (sections 3 and 2) and a high HD (section 3.5) is a good candidate for such coatings. Thin transparent coatings, however, often show strong light interference effects leading to a coloration of the coatings. This is undesirable for most optical applications.

5.2.1 Coatings to reduce interference coloration

Interference colors from coatings arise, as incident light (each incident photon) is split at the film surface: One part is reflected, while the other part is transmitted through the film and then reflected at the film/substrate interface. The two reflected parts interfere, leading to higher intensities for specific colors under specific angles. Such an interference is however only possible if the path difference remains smaller than the coherence length of the incoming light. Here we assume the light arises from incoherent light sources, *i.e.* light with a very small coherence length typically in the range of a few wavelengths. For a coating thickness of around a micron or thinner, the path difference remains comparable to the wavelength of the light and thus comparable to the coherence length. Then, interference and associated coloration will occur even for conventional light sources (*e.g.* blackbody radiation). Note that the same explanation holds for soap bubbles. A thicker coating of *e.g.* 1500 nm then yields less intense interference colors than a thinner coating of *e.g.* 300 nm. Light with a continuous spectrum, *e.g.* solar light or light emitted by a bulb or even LED white light, leads to less perceivable interference coloration than light from a fluorescent lamp that has a spectrum with a few strong spectral components. This is because each of these spectral components has a higher intensity than the same wavelength range in a blackbody spectrum from an ordinary light bulb, white LED light or sunlight. Therefore, the part of the spectrum of a fluorescent lamp with strong weighting generates intense interference colors at certain observation angles, while at other observation angles, no interference is seen.

The refractive index n of a coating is an important parameter when designing antireflective or low interference optical coatings. The larger the difference in n between two media is, the stronger is the intensity of the beam reflected from the interface between the two media. Here, ellipsometry was used to measure n (details given in section 8.5). In fig. 5.3, n for light of 632.8 nm is plotted versus O and Si contents of the coatings. For both Al-O-N and Al-Si-O-N, $n_{632.8nm}$ decreases linearly from 2.1 to around 1.6 for an O content increasing from 0 to around 60%. The Si content of the coatings shows no influence on n.

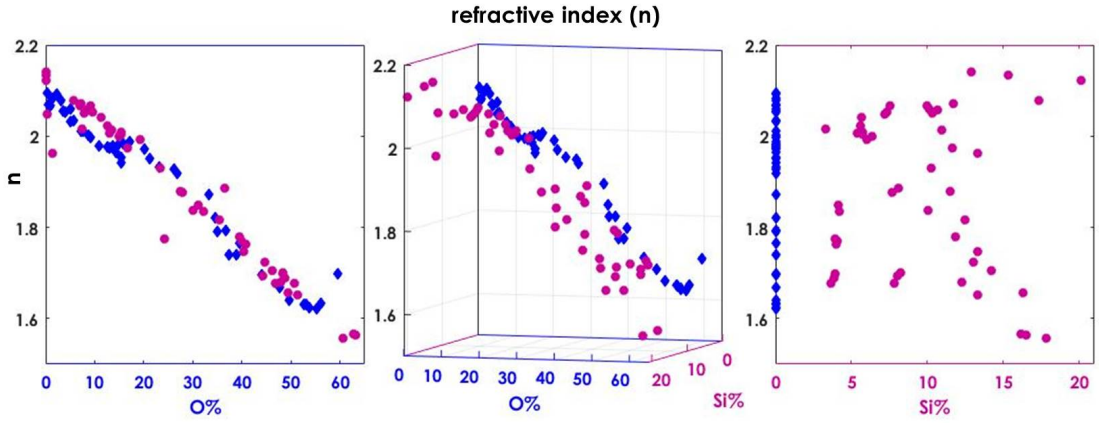

Figure 5.3: 3D diagram of refractive indices for light of 632.8 nm wavelength ($n_{632.8nm}$) versus O and Si contents in thin films of Al-O-N (blue rhombi) and Al-Si-O-N (magenta circles). The spread of n in Al-Si-O-N (on the right) is due to different O contents of the coatings.

To suppress optical interferences, the n of a coating must be matched to that of the substrate. Al-(Si-)O-N exhibits a reduced n similar to that of glass at higher O content, which is the concentration region where the coatings also are less hard and therefore less suitable for a protective coating. However, the variation of n with O in Al-(Si-)O-N can be used to design coatings with suppressed interference coloration, if a gradient layer with increasing O content towards the substrate is deposited. This is illustrated in fig. 5.4, which a) shows a gradient coating with Al-Si-N at the surface and Al-(Si)-O-N of a high O content of 60% at the interface to a glass substrate, in comparison to b) a homogeneous Al-Si-N coating. Al-Si-N was chosen as a material in this example, as it exhibits high HD values up to 30 GPa as well as no open crystal boundaries in the solid solution regime (II)[122]

(sections 3.6 and 3.4), and is therefore well suited for a protective coating that is also a diffusion barrier. For simplicity, the phase shift in the interfering light beams induced by the coating thickness is neglected in the model in fig. 5.4, and only one light incidence angle of 45° with respect to the beam as well as to the sample surface is considered.

At the air/Al-Si-N boundary of both coatings, the reflection angle for the reflected part of the beam is equal to the incidence angle and thus 45°. The angle for the transmitted part of the beam with respect to the sample surface normal can be derived from Snell's law:

$$n_1 sin\theta_1 = n_2 sin\theta_2 \tag{5.1}$$

with n_1 and n_2 the refractive indices in media 1 and 2, respectively, and θ_1 and θ_2 the incidence angle in medium 1 and the transmitted angle in medium 2, respectively. At the coating surface of both situations a) and b), n_1=1.0 for air, n_2=2.1 for Al-Si-N and θ_1=45°, and θ_2 therefore amounts to 19°.

The reflected part of the beam can be derived from the Fresnel equations:

$$R_s = \left|\frac{n_1 cos\theta_1 - n_2 cos\theta_2}{n_1 cos\theta_1 + n_2 cos\theta_2}\right|^2, \; R_p = \left|\frac{n_1 cos\theta_2 - n_2 cos\theta_1}{n_1 cos\theta_2 + n_2 cos\theta_1}\right|^2 \text{ and } R = \frac{R_s + R_p}{2} \tag{5.2}$$

with R_s, R_p and R the reflectances for s-, p- and un-polarized light, respectively. R at the coating surface in amounts to 14%.

In the homogeneous Al-Si-N coating in b), the transmitted beam of 100%-14%=86% continues at the angle of 19° down to the Al-Si-N/glass interface. There, the reflection is with 2.7% (formulae 5.2) lower than at the air/Al-Si-N surface, as the mismatch in n between Al-Si-N and glass with n=1.5[103] is lower than that between air and Al-Si-N. Back at the Al-Si-N/air interface, 2.7%*0.86=2.3% of the incident light beam is transmitted to air and interferes with the former constructively. Without a phase shift, this leads to a maximal intensity of 2.3%/0.14=16.4% intensity of the interference beam with respect to the initially reflected beam.

In the gradient coating in a), the beam transmitted initially also amounts to 86% of the incident beam and proceeds through the coating at 19° with respect to the sample surface. Within the coating, however, the latter angle gradually increases to 26° (formula 5.1), as n decreases to 1.6 for Al-(Si-)O-N of high O content

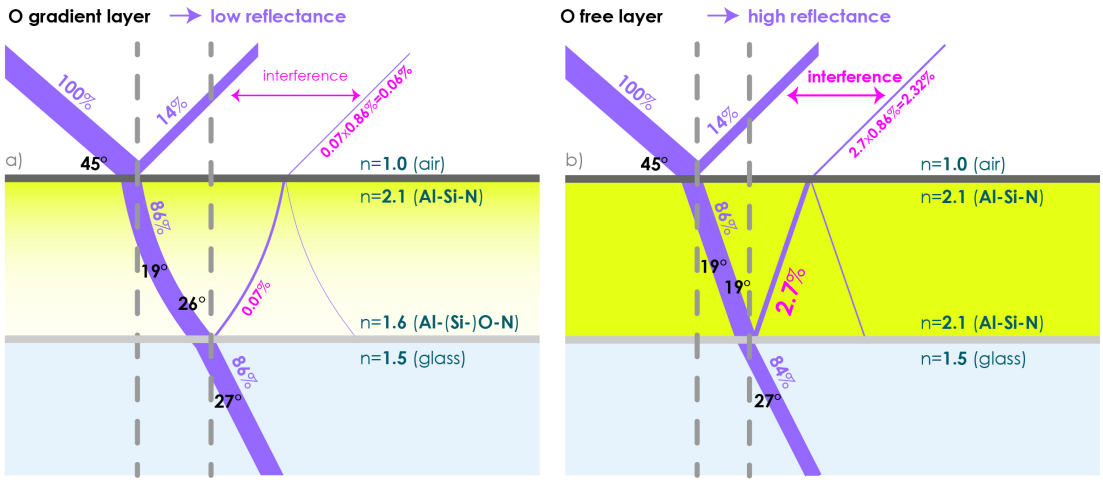

Figure 5.4: Light beam interactions in a coating a) with and b) without O gradient. Snell's law provides the angles and the Fresnel equations the reflectances.

(fig. 5.3). At the Al-(Si-)O-N/glass interface, the mismatch in n between Al-(Si-)O-N with n=1.6 and glass is only 0.1, and therefore the reflected beam part amounts to only 0.07%. Of the latter, 0.07%*0.86=0.06% is transmitted back to air and interferes constructively with the reflected part of the incident beam, leading to 0.06%/0.14=0.4% intensity of the interference beam with respect to the initially reflected beam.

While the reflected light power of the beam is with 14%+0.06%=14.06% only 14% lower in the gradient coating (a)) compared to the uniform coating (b)) with 14%+2.3%=16.3%, the interference intensity, being 0.4% and 16.4%, respectively, is significantly suppressed by a factor of more than 40.

The graded coating (a)) has a further advantage. While Al-Si-N at the surface of the coating is hard and therefore provides protection against wear and impact, the mechanical properties of Al-Si-N (HD=30 GPa and E=250 GPa[122], sections 3.5 and 3.6) are significantly different from those of glass (HD=5.5 GPa and E=74 GPa for sodalime glass; HD=6.4 GPa and E=63 GPa for borosilicate glass[23]). The transition to Al-(Si-)O-N (HD=8 GPa and E=150 GPa, section 3.6), however, adapts the mechanical properties of the coating gradually to those of the glass substrate.

5.2.2 Antireflective coatings

Antireflective (AR) coatings are designed to suppress any reflectance. Such coatings are typically produced with CVD processes and consist of multilayer systems of one or several transparent materials having different refractive indices n, with the topmost layer having the lowest n[62]. SiO_2 with $n_{632.8nm}$ of 1.5[103] or MgF_2 with 1.4[33] are possibilities for such top layers. A general problem is that many materials of low n are also of low hardness, *e.g.* 8 GPa for SiO_2[8] and 4.2 GPa for MgF_2[130], and are thus not advantageous as a top layer for an optical coating that should simultaneously be abrasion resistant.
In the Al-(Si-)O-N system, this disadvantage is also evident. While coatings with increasing O content have a lower n (fig. 5.3), they also become less hard (sections 3.5 and 3.6). However, if AR coatings shall be produced with a PVD process, Al-(Si-)O-N can more easily be deposited by R-DCMS than pure oxides or fluorides (chapter 2), which may require radio frequency (RF) power control of the targets[182]. Therefore, Al-(Si-)O-N coatings remain potential candidates for sputtered AR coatings, providing the possibility to tune n between 2.1 and 1.6 within the same material system. This application has not yet been explored.

5.3 Decorative coatings

5.3.1 Colored transparent coatings

In section 5.2.1, a strategy was described to suppress interference coloration, which is useful for protective coatings on optical devices. For decorative effects, in contrast, interference colors can be specifically enhanced. As discussed in section 5.2.1, interference coloration is intensified by choosing a low film thickness (*e.g.* 300 nm rather than 1500 nm) and a chemical composition regime with a low O content and therefore a high n (fig. 5.3). On transparent substrates such as glass, pastel colorations are observed, while the transparency of substrate plus film is maintained. Interference colors are especially preeminent on dark reflective substrates such as polished Si. This is visible in fig. 5.1, even though these coatings would not generally be described as very thin with around 1 μm and thus interference coloration is not particularly intense. Greenish (sample with 1% O), bluish (5.7% and 1.3% O) and purplish (49.7% O) colors are visible.

5.3.2 Colloidal Au

A different decorative application for Al-(Si-)(O-)N is its use as a transparent matrix for the incorporation of color centers, a function that can be fulfilled by nanoparticles of metals. If such nanoparticles are dissolved in a matrix, they are often referred to as "colloidal metal". Metallic nanoparticles scatter and absorb visible light, as their conducting e^- at their surface oscillate in resonance with irradiating light. This effect is called Localized Surface Plasmon Resonance (LSPR) and evokes intense colorations. The resulting color depends on the size, size distribution, shape, chemical composition and aggregation state of the nanoparticles. The larger the particles, the larger the absorbed wavelength. Smaller nanoparticles thus lead to a red coloration and larger ones to a blue coloration. The more narrow the size distribution, the less polychromatic the color[175,16].
Church glass windows made over the last centuries were often colored through the LSPR phenomenon. With Au nanoparticles, lustrous colors of the entire spectrum were created. Fig. 5.5 shows a modern creation of such a stained glass window decorating *La Sagrada Familia* in Barcelona.

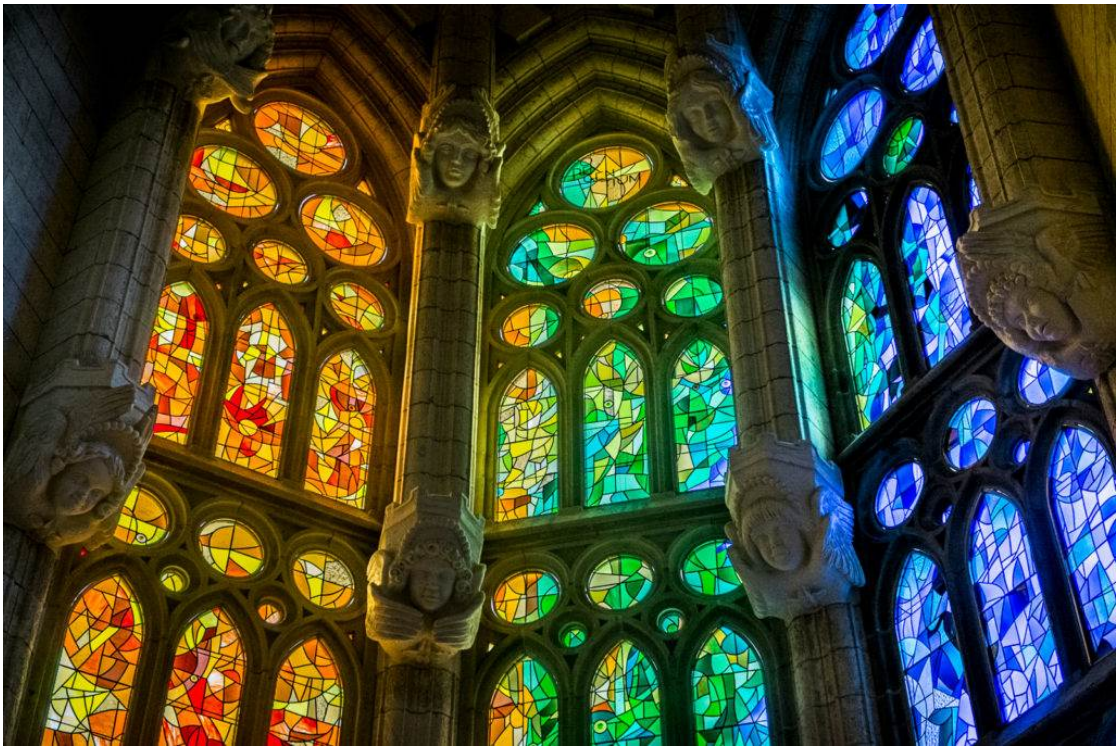

Figure 5.5: Stained glass window in *La Sagrada Familia*, Barcelona. Colors arise from Au nanoparticles dissolved in the glass. Photo taken by Dan Taylor and retrieved from *Galerie* (http://www.galeriemagazine.com).

In sputter deposition, metal inclusions of small size can be obtained by generating multilayers. To separate the metal containing areas in the growth direction, interlayers of metal-free transparent films are used as spacers, and the thickness of these can be precisely controlled through the deposition rate. The spacing of the metal in-plane, however, is more difficult to control, as the deposition proceeds layer-wise. The lateral spacing is therefore determined by the amount and the species of metal deposited and separated clusters or homogeneous nanolayers can form.

In this project, Au was chosen as the nanoparticle material, as this metal is well-known for its tendency to form islands instead of wetting a surface homogeneously[123]. Au is therefore expected to form a lateral separation of isolated metal clusters in preference to a nanolayer. The four options AlN, Si_3N_4, Al-Si-N

and Al-O-N were assessed as matrix materials. AlN, Si_3N_4 and Al-Si-N coatings including colloidal Au were observed to have an unfavorable grayish tint, and some of these films were homogeneously gray. Al-O-N yielded the most intense coloration and was thus used for most of the investigated coatings. In addition, two different metal spacing options were investigated, as illustrated in fig. 5.6.

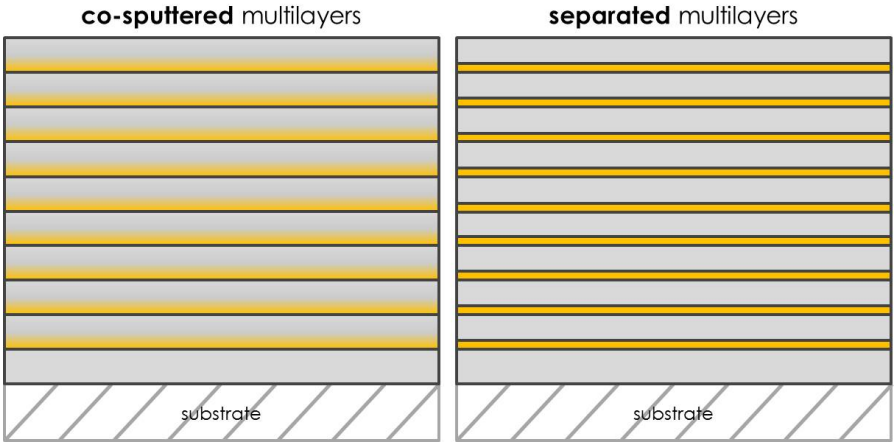

Figure 5.6: Two matrix/Au multilayer coatings containing colloidal Au. Both begin with a pure matrix layer (gray) on the substrate. On the left, Au (yellow) is co-sputtered with matrix material in the beginning of each layer and the continuation is with matrix material only. A stack of nine such layers is shown. On the right, Au is sputtered separately and sandwiched between 10 pure matrix layers. In the experiments described in the text, the number of stacked layers was varied.

Option one, on the left, was to co-sputter Au plus matrix during the first few seconds of a layer, and then deposit matrix material alone until the next layer started. 10 to 20 such layers were stacked for each coating. Option two, on the right, was to deposit separate layers of matrix and Au. Around 9 Au layers were embedded between 10 matrix layers. Both options were primed with an Au-free, pure matrix layer.

Fig. 5.7 shows such Al-O-N multilayer stack samples of both options, with three c (co-sputtered) and two s (separately sputtered matrix and Au) samples, and table 5.1 summarizes their production parameters. Option one (c samples) yielded reddish films, attributed to smaller colloidal Au particles, and option two (s sam-

ples) bluish films, attributed to larger particles[175,16].

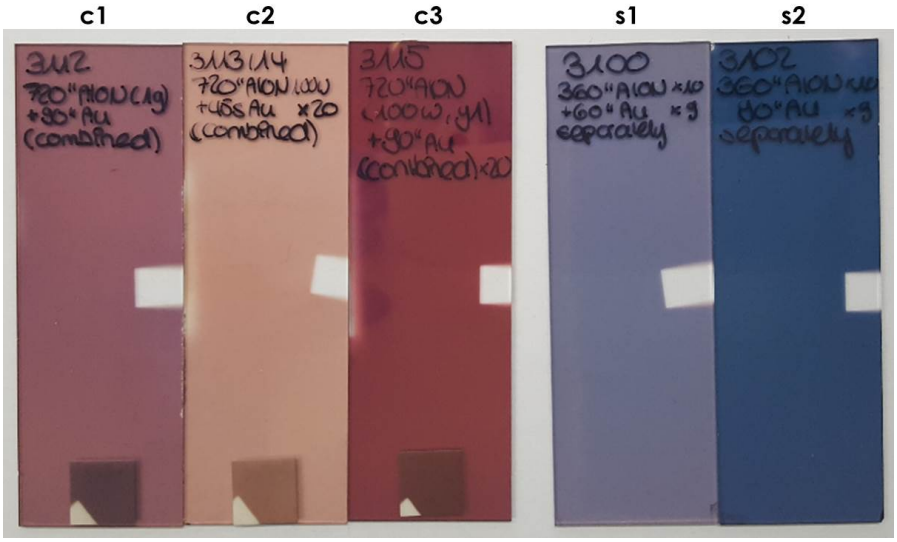

Figure 5.7: Photograph of Al-O-N/Au multilayer coatings on glass. c are co-deposited multilayers of Au and Al-O-N, s are separated Au and Al-O-N multilayers as illustrated in fig. 5.6. Co-sputtered stacks (c1, c2 and c3) are reddish, separately sputtered ones (s1, s2) are bluish. Detailed deposition parameters are given in table 5.1. The samples are labeled with in-house numbers and comments in black on top. Colorless, coating-free areas result from clamping the substrates. c1-c3 additionally show a polycrystalline α-Al_2O_3 platelet, coated in the same deposition to test the color effect on a non-transparent white substrate, in the lower part of the photograph.

The intensity and brightness/darkness of the coatings can be adapted by altering the length of time of Au sputtering, the power on Al, and the number of multilayers,. This is for example evident in the comparison of c2 and c3 (fig. 5.7 and table 5.1), both deposited with 100 W on Al and consisting of 20 combined multilayers. The sample c2, for which the Au sputter time was 45 s, is brighter than c3, for which the Au sputter time was with 90 s twice as long. Due to the lower deposition rate obtained in 100 W samples compared to 200 W samples, 20 multilayers were deposited for the former and 10 for the latter. All films have a purplish tint and thus exhibit polychromatic coloration. This indicates that the particles have a variation in size and shape. The co-sputtered samples c2 and c3, deposited with 100 W on Al, appear less purplish and less polychromatic than c1, sputtered with 200 W on Al. This suggests that lower Al-O-N deposition rates

Table 5.1: Parameters used for the colloidal Au samples c1, c2, c3, s1 and s2. P is DC power [W], T is time [s]. All multilayer stacks were deposited onto glass slides; c1, c2 and c3 additionally onto polycrystalline α-Al_2O_3 and PEEK. The pressure during depositions was around 5 μbar. The setup described in chapter 2 was used. 12 sccm pure N_2 and 6 sccm 10%O_2/90%N_2 were used for all Al-O-N films deposited. This resulted in $AlN_{0.6}O_{0.6}$ for Au free fractions.

sample	Au P	Au T	Al P	Al-O-N T	# layers	thickness
c1	5 W	90 s	200 W	720 s	10*combined	326 nm
c2	5 W	45 s	100 W	720 s	20*combined	273 nm
c3	5 W	90 s	100 W	720 s	20*combined	291 nm
s1	5 W	60 s	200 W	360 s	10*Al-O-N+9*Au	314 nm
s2	5 W	90 s	200 W	360 s	10*Al-O-N+9*Au	316 nm

lead to smaller Au nanoparticles having a more narrow size distribution.
The experiments demonstrate that colloidal Au can be generated inside hard films, which colors the films red, purple or blue and provides decorative coatings. Additionally, the colored films can serve functional purposes, *e.g.* in plasmon-based detectors and modulators or LSP-enhanced solar cells[16]. An industrial partner in this project is exploring a further potential application of the colored coatings for medical tooth implants. These need a hard and wear resistant surface, which can be inherent in ceramic implants, or be provided by an Al-(Si-)O-N coating. White ceramic implants, uncoated or transparently coated, however, would be visible through the gums, which is undesirable. A purple colored coating on the denture part implanted in gingiva could avoid the visibility of the implant through the gums. Therefore, the coloration effect of Al-(Si-)O-N coatings containing Au nanoparticles was also tested on bright, non-transparent ceramic substrates. Polycrystalline α-Al_2O_3 and polyether ether ketone (PEEK) platelets were coated along with glass in some runs. In fig. 5.7, c1-c3 contain the α-Al_2O_3 platelets at the bottom of the photograph (PEEK not shown). A coloration similar to that of gingiva is obtained.

6 Conclusions and Outlook

In this project, a setup was developed that allowed the controllable and reproducible reactive sputter deposition of transparent thin Al-(Si-)O-N films using the highly reactive gas O_2. The development of this modification to the coating equipment, including separated inlets for all gases, brought a deeper understanding of the processes occurring during the Physical Vapor Deposition assisted by magnetrons. This method could also be used to show that the poisoning of the target by O_2 can be inhibited by feeding N_2 locally concentrated to the target.

With this setup, around 300 deposition runs were carried out, yielding transparent Al-O-N and Al-Si-O-N coatings with adjustable O and Si contents. An in-depth analytical investigation of these samples revealed a gradually evolving microstructure of the ternary Al-O-N system with increasing O content. It could be shown that the O content correlated with the evolution of mechanical and physical film properties such as the hardness, the elasticity, the residual stress and the refractive index. A model for these evolutions could be proposed, containing a crystalline wurtzite solid solution regime (I), a fiber textured nanocomposite regime (IIa), a nanocomposite regime without pure uniaxial texture (IIb), and an amorphous solid solution regime (III). This evolution model is reminiscent of that of Al-Si-N which has been investigated previously[122,123,125], although substitutions of different nature are induced in the two systems. It could be hypothesized that this similarity is due to extra e^- [129] in both cases, which was corroborated by DFT calculations.
These calculations provide additional insight into the thermodynamic state of the Al-O-N coatings. The results yield a preliminary estimation of the free energy in the coatings but are not conclusive, and a further investigation, *e.g.* into the entropy arising from grain boundary phases in nanocomposites, poses an interest-

ing topic for future research. Furthermore, Al-O-N samples of all microstructural regimes have been measured by now by Positron Annihilation Spectroscopy (PAS) as well as lifetime measurements of the latter (PALS) at the ELBE beamline in Dresden-Rossendorf, Germany. This technique is supposed to provide an experimental assessment of vacancies such as V(Al) or voids in grain boundaries. The evalutation of the measurements is ongoing and the results are expected soon, and shall be combined to the results obtained by DFT calculations.

The quaternary system Al-Si-O-N exhibits more complex microstructural changes, probably assignable to additional interactions between Si and O. While a detailed investigation into the microstructure of Al-Si-O-N films was not the aim in this project, it was demonstrated that the quaternary system exhibits physical properties in the same range as Al-O-N and Al-Si-N and is useful as a complementary material in a number of applications. The potency of coatings made from Al, Si, O and N therefore lies in the high degree of freedom in variability, as the contents of each element can be precisely adjusted to deposit coatings with specific, desirable properties. The R-DCMS technique has the advantage that this variability of chemical composition can be applied *in situ* by changing sputter parameters such as the gas flows or magnetron power values during a single deposition run, resulting in multilayer or gradient coatings. This allows, for example, the mechanical properties of a coating to be adapted to a relatively soft substrate such as glass, while providing a hard or oxidation resistant finish at the coating surface.

Al-(Si-)O-N coatings were tested for several applications. This showed the potential of this versatile material system, but equally the areas where further research is needed for a successful application. The coating of mobile phone parts, for example, such as screens and also backside glass covers is, according to preliminary tests, promising for abrasion and fracture resistance. However, a thorough evaluation of coated parts by an industrial partner are still required and ongoing. In such applications, the suppression of interference colors by gradient layers may emerge to be highly useful, and eventually also the design of sputter-deposited antireflective coatings. These could, for example, be fabricated with Al-(Si-)O-N, an application not yet addressed in this project.

An application that proved to be challenging was the coating of polycarbonate. As Al-(Si-)O-N coatings are significantly harder than the polymer substrate, the latter could greatly profit from the application of the former. However, the crack formation in the film due to the difference in elasticity between film and substrate remains a drawback. Additionally, low deposition temperatures are required due to the low glass transition temperature of PC. The use of High Power Impulse Magnetron Sputtering (HiPIMS) could be interesting here and worth further investigation. As higher ionization rates and particle energies are involved in HiPIMS processes compared to conventional DC sputtering, the interaction between PC substrate and film may be modified, and a good film quality may be achieved despite a lower deposition temperature.
A particularly fascinating experimental part was the creation of red, purple and blue coatings by incorporation of colloidal Au. Such coatings are simultaneously protective and decorative, and could be used to enhance the value of objects such as furniture parts or jewelry.

7 Appendix A: Supplementary data

The modified setup for R-DCMS described in the paper in chapter 2 allowed the deposition of ternary and quaternary Al-(Si-)O-N thin films in stable, reproducible processes. The material properties of these Al-(Si-)O-N films are reported in the paper in chapter 3. This appendix part contains measurement data that constitutes the basis for the processed data reported in the paper in chapter 3.

7.1 Chemical compositions

As reported in section 3.2 and explained in section 1.3.4, transparent, metal-free Al-(Si-)O-N films have the general stoichiometry $AlSi_xO_{1.5+2x-1.5z}N_z$, which simplifies to $AlO_{1.5(1-z)}N_z$ for Al-O-N films containing no Si and thus having x=0. Close alignment between these theoretically expected stoichiometries and those measured experimentally with RBS and ERDA for the films of this project was found and the formulas above held within the accuracy of the analytical techniques.

The composition of the Al-(Si-)O-N coatings can be displayed in a 2D diagram as in fig. 7.1. Each axis shows the content of one element, and the other two elements are then a function of the first two according to the formula above. O and Si are chosen as axes in this project, since the starting point was AlN and O and Si were added. Al and Si as well as N and O can be regarded as complementary: The more Si a film contains, the less Al is present, and the more O is added, the less N is present. In fig. 7.1, the compositions of the deposited Al-O-N (blue rhombi; all on the O% axis due to zero Si content) and Al-Si-O-N (magenta dots) films are plotted. The Si content varies as a function of the sputter power applied to the Si target, while the O content varies with the O_2 flow rate fed into the deposition process (chapter 2).

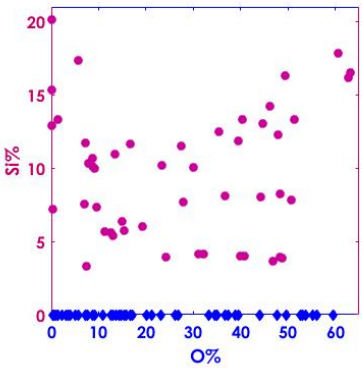

Figure 7.1: Chemical compositions of thin films of Al-O-N (blue rhombi) and Al-Si-O-N (magenta dots) with respect to their O and Si contents.

Further film properties given in this appendix part will be added as a z-axis to the composition graph, resulting in a 3D plot. For each 3D plot, three views will be given: The view on the x-z-plane (*i.e.* property parameter versus O content) on the left, a view into the 3D diagram in the middle and the view on the y-z-plane (*i.e.* property parameter versus Si content) on the right.
Such a graph is shown in fig. 7.2 for the amount of hydrogen H detected in the coatings by He-ERD. As discussed in section 3.2, H was found in Al-O-N exclusively in films with 8-16% O belonging to the fiber textured nanocomposite regime (IIa) (compare fig. 7.2, left to section 3.4). The films were produced on different days and correspondingly under differing deposition chamber conditions, and the RBS, ERDA and He-ERD measurements were carried out on different days. This indicates that H incorporation into Al-O-N exclusively in regime (IIa) is repeatable and not an artifact. While a conclusive explanation for this phenomenon of H incorporation could not be found, it can be speculated (as in section 3.5) that the Al_2O_3 matrix encapsulating the wurtzite crystallites is hygroscopic and under tensile stress and thus allows the absorption of water. In films with less than 8% O, no Al_2O_3 matrix exists, and films with more than 16% O are under compressive stress. Thus no water is stored in films of any other regime.

For Al-Si-O-N, H contents of ∼1% were detected in around $\frac{1}{3}$ of the films with no

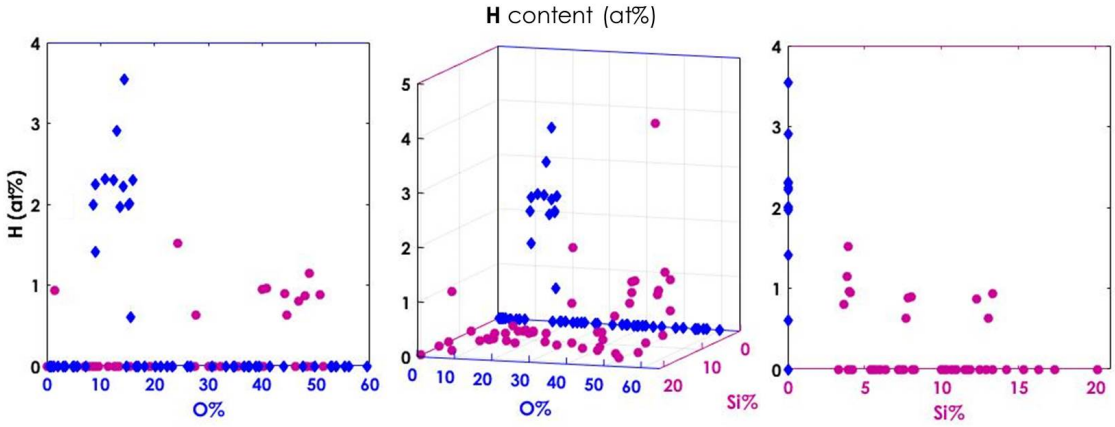

Figure 7.2: 3D diagram of H contents detected by He-ERDA versus O and Si contents in thin films of Al-O-N (blue rhombi) and Al-Si-O-N (magenta dots). Three different views of the 3D graph are given to show H vs. O and H vs. Si more clearly.

restriction to their contents of O or Si (fig. 7.2). The H content in Al-Si-O-N is therefore lower than in Al-O-N and not significant.
It is not possible to conclude from the results of He-ERD measurements whether H was incorporated directly during film deposition or afterwards via diffusion, as no dispersion trend can be perceived in depth profiles.

7.2 Crystallinity

As reported in section 3.3.1, thin films of ternary Al-O-N fabricated in this project exhibit a gradual loss of crystallinity with increasing O content. For films with 0-8% O belonging to regime (I), a (002) wurtzite fiber texture forms (fig. 3.4). The crystallites exhibit a decreasing c-axis lattice parameter, a decreasing crystallite size (CS) and an increasing (002) axis tilt for increasing O concentration. Films with 8-16% O of sub-regime (IIa) consist of a (002) fiber textured nanocomposite, as an amorphous Al_2O_3 matrix surrounds the crystallites. The microstress (MS) increases in the encapsulated crystallites. For 16-30% O in (IIb), a nanocomposite without fiber texture results, such that crystal grains can assume any orientation in the Al_2O_3 matrix while becoming progressively smaller towards the X-ray detection limit with increasing O content. Films with 30-60% O of regime (III) consist of an X-ray amorphous Al-O-N network.
The following sections will show diffractograms and plots of raw data obtained from XRD techniques. This data provided the basis for the processed data implemented in section 3.3.1.

Al-O-N

Figs. 7.3 and 7.4 show the symmetric θ-2θ diffractograms that led to the results on the c-axis lattice parameter, the CS and the MS plotted in fig. 3.1 and discussed in section 3.3.1. Fig. 7.3 shows diffractograms for Al-O-N films containing up to 14.3% O. The only peak detected is that of the wurtzite (002) planes, which indicates that these are the only planes perpendicular to growth direction z and thus constitute the texturing in the growth direction. Only the 2θ range relevant for (002) between 35-38° is shown. The fitted components for Cu Kα_1 are plotted with a thinner line under each peak. The diffractogram of a film with residual 0.4% O shows the Kα_1 (002) signal close to the theoretical value of 36.07 for pure wurtzite (ICSD collection code 34475)[145]. A gradual shift to higher 2θ is then observed with increasing O concentration up to 8%, which corresponds to the c lattice shrinkage reported for that O content regime (fig. 3.1a)). Between 8 and 14% O, the (002) peak remains constant at 36.3°. A peak broadening is seen for the entire span of the O increase. Two effects are simultaneously responsible for this: CS shrinkage and MS generation. CS and MS were obtained from peak deconvolution through line profile analysis (LPA)[11, p. 85–101] as reported in section 3.3.1 (fig. 3.1b) and c)).
Fig. 7.4 shows diffractograms for Al-O-N films containing 14.7-34.6% O. Additional diffraction signals appear in the range 30-40° in 2θ. Around 16% O, a transition in the texture is observed. The two samples with O concentrations of 14.7% and 15.9% do not only exhibit (002), but also (100) and (101) planes in z direction and thus are not uniaxially (002) textured in z. As the (002) peak has a higher intensity than the (100) and (101) peaks, the texture in z is still (002)-preferred and not random. These two samples with preferred (002) texture in z are shown with open symbols in fig. 3.1. The sample with 15.3% O maintains (002) fiber texture.

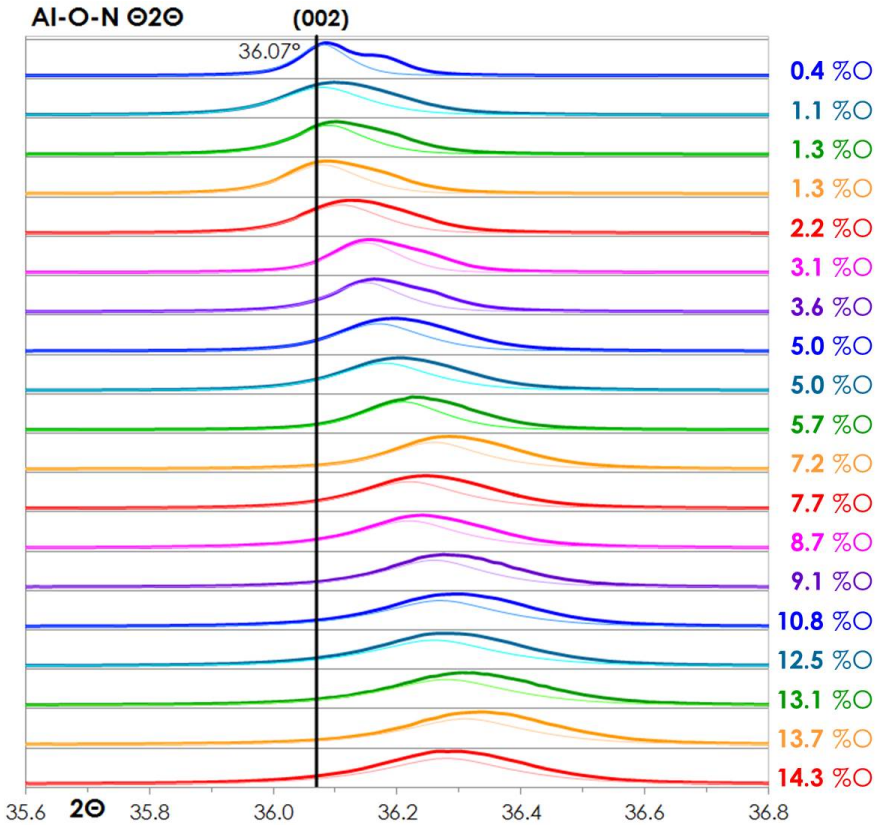

Figure 7.3: Diffractograms of Al-O-N thin films derived from symmetric θ-2θ scans recorded with Cu Kα. Normalized diffractograms of samples with O contents in the range 0.4-14.3% are shown between 35.6-36.8° in 2θ. Fitted Cu Kα_1 components are added with thinner lines. The position of the Kα_1 wurtzite AlN (002) reference peak[145] at 36.07° is shown in black for comparison.

From 16% O upward, the (002) line develops a shoulder towards lower 2θ. This is clearly seen for the peak of the 16.6% O sample: Two Kα_1 components are needed to fit this peak. One remains at the position of 36.3°, while the second is found at 35.7°. Two phenomena can explain this shoulder. Firstly, the additional peak can arise from c lattice spacing variation towards the grain boundaries. The volume in the outer shell region of a small crystallite is significant compared to its core volume; variation in c at the outer shell therefore becomes detectable as the size of the of the crystallite decreases. Secondly, the additional peak can be caused by a partially ordered phase forming around the grain boundaries[125]. Also a combination of these two effects is possible. For films with a higher O content than 17%, LPA was not meaningful and thus no Cu Kα_1 components are shown.
Films with O concentrations of 23-30% generate two broadened peaks, possibly corresponding to right shifted (100) and (002) peaks.

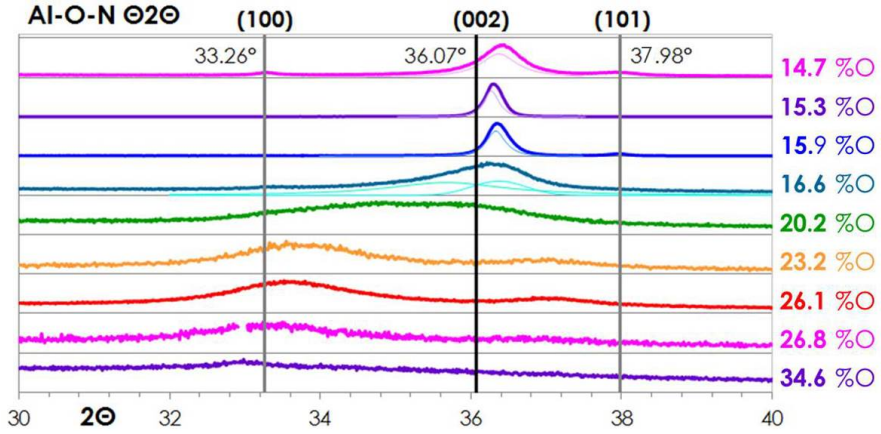

Figure 7.4: Diffractograms of Al-O-N thin films derived from symmetric θ-2θ scans with Cu Kα. Normalized diffractograms of samples with O contents in the range 14.7-34.6% are shown between 30-40° in 2θ. Fitted Cu Kα_1 components, where relevant, are added with thinner lines. The positions of the Kα_1 wurtzite AlN reference peaks[145] at 33.26 for (100), at 36.07 for (002) and at 37.98 for (101) are shown in black and gray. In the data trace of the sample with 26.8% O, the Si(200) peak region around 33° was removed for a clearer view on the film signals.

In the data trace of the sample with 26.8% O, Si(200) was removed, leaving a small gap. Si(200) is basis-forbidden and thus normally not seen in diffractograms recorded on Si(100). It can however be detected due to multiple diffraction[135,190,137], and disturb the diffractogram under investigation with a sharp, intense peak. Omitting it thus serves to clarify the diffractogram.
Films containing more than 30% O do not show wurtzite crystallinity. The sample containing 34.6% O still shows an unassigned, broad hump at a 2θ around 33°. At more than 35% O, the films yield fully flat diffractograms.

On the (002) peaks obtained in the diffractograms, rocking curves (RCs) were performed. As discussed in section 3.3.1, these (002) RCs broaden for coatings with increasing O content. Fig. fig. 7.5 shows the full widths at half maximum (FWHMs) of the measured RCs for Al-O-N coatings with 0-8.7% O. A film with residual 0.4% O has a RC with a FWHM of 2.1°. With increasing O, the FWHMs of the RCs continously broaden up to 10.8° for a sample containing 8.7% O. RCs at higher O contents are too broad to be

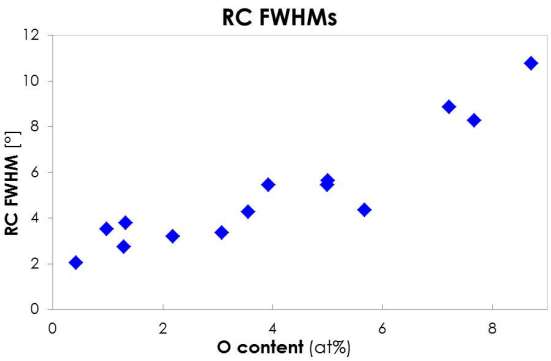

Figure 7.5: FWHMs of RCs [°] measured on wurtzite (002) peaks for Al-O-N films with up to 8.7% O.

properly evaluated.
Broadening (002) RCs for samples with increasing O content signify that the c-axes of crystallites deviate more and more from growth direction z, as crystallites adopt an angular tilt as reported in section 3.3.1. The advanced tilt of crystallites in films with O contents around 16% and above is also seen in the appearance of additional peaks in symmetric θ-2θ diffractograms (fig. 7.4). The appearance of (101) requires crystallite (002) axis tilts with respect to z of 61.57° and (100) requires tilts of 90.0°, meaning the absence of pure (002) texture in growth direction z.

In section 3.3.1 it is reported that pole figures (PFs) reveal that Al-O-N films with an O content up to around 16% are (002) fiber texured. Fig. 7.6 shows set of three such PFs, *i.e.* (002), (103) and (101) PFs, for an Al-O-N coating containing 5.0% O. Linear 2.5D plots on the left, logarithmic ones on the right and logarithmic 2D top views in the middle are shown. $PF_{(002)}$ (fig. 7.6 top) shows a single pole at a sample inclination angle Ψ=0, indicating that (002) planes are only found orthogonal to growth direction z. This confirms the observation of symmetric θ-2θ XRD, which only showed the (002) peak for samples of the same O content. The weak rim at Ψ=55° is of such low intensity that it is only visible on the logarithmic scale. Its origin is probably a shoulder signal of (101), as (101) planes have an inclination τ of 61.57° with respect to (002) planes and with 37.98° a 2θ close to that of (002)[145].
$PF_{(103)}$ (fig. 7.6 middle) appears at a Ψ close to the theoretically expected value of τ=31.63°. The same is valid for $PF_{(101)}$ (fig. 7.6 bottom), having a Ψ close to τ=61.57°. Both $PF_{(103)}$ and $PF_{(101)}$ show rims of equal intensity on the entire Φ circle, which indicates that the film exhibits wurtzite (002) fiber texture.
It should be noted that the single presence of the (002) peak in symmetric θ-2θ diffractograms (fig. 7.3) and the single pole in $PF_{(002)}$ show uniaxial z texturing, but these two results alone do not exclude epitaxy of a film with respect to the substrate. The even annular rims obtained in $PF_{(103)}$ and $PF_{(101)}$, however, demonstrate random in-plane orientation.
All samples with pure (002) orientation in z exhibit the same PF pattern, but an increasing rim width for increasing O content. The PF rim widths are the equivalent of widths of RCs (fig. 7.5), but for a different scan angle (Ψ instead of ω).

Al-O-N could potentially form in the cubic sphalerite modification, which has the (111) XRD peak close to that of (002) wurtzite. In order to test the films for the presence of sphalerite, PFs were thus also taken on planes of the latter. No sphalerite was detected.

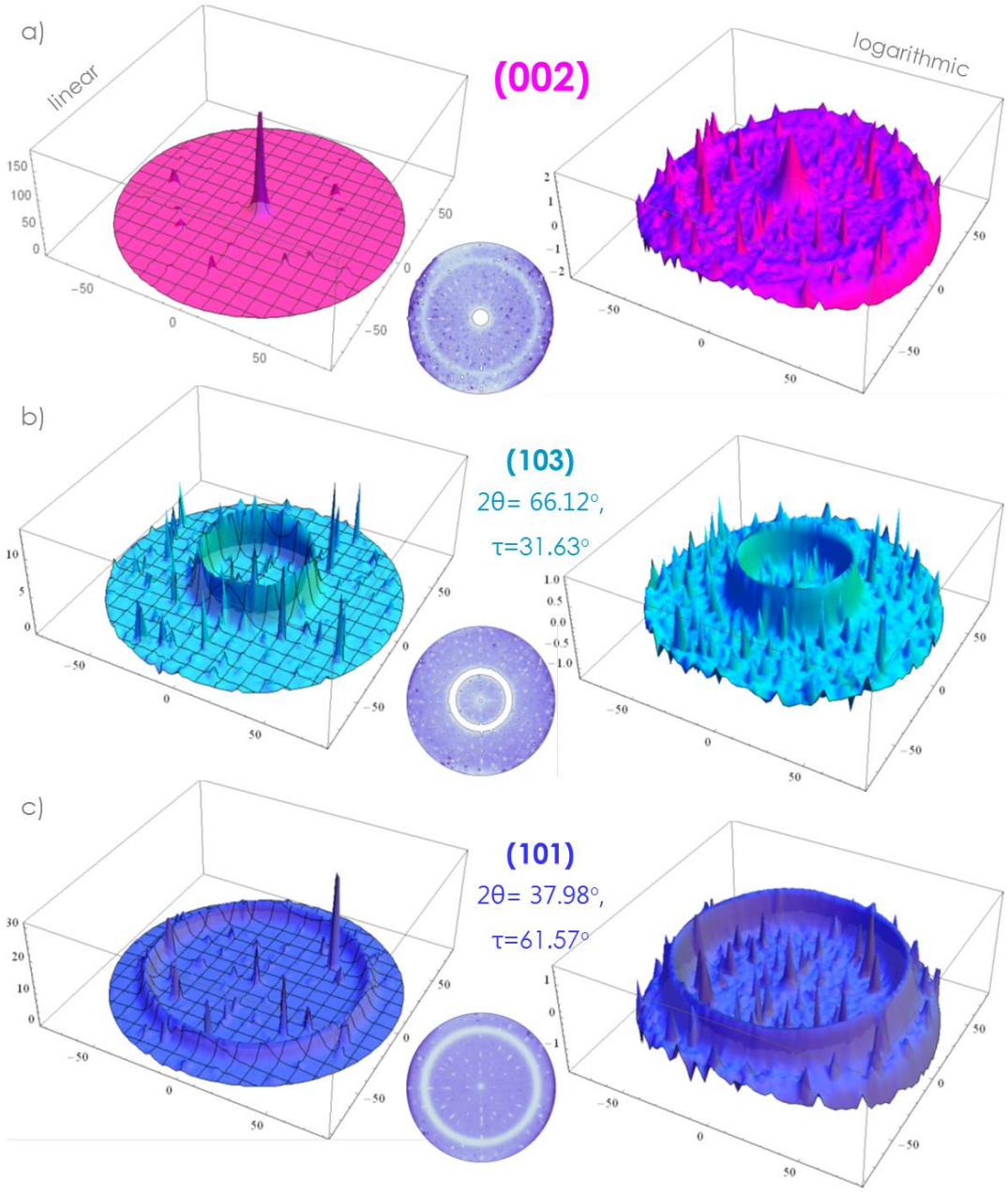

Figure 7.6: PFs measured for an Al-O-N thin film containing 5% O. $PF_{(002)}$ (a), top, magenta), $PF_{(103)}$ (b), turquois, middle) and $PF_{(103)}$ (c), blue, bottom.) Linear 2.5D plots (left), logarithmic 2.5D plots (right) and logarithmic 2D top views (middle) are shown.

As a result of (002) texturing in growth direction z for samples with an O content up to approximately 16%, the lattice shrinkage up to 8% O shown in fig. 3.1a) is only seen in the c direction in symmetric θ-2θ scans. In order to determine whether the same trend also applies for the a=b dimension, in-plane measurements and θ-2θ scans asymmetric to the surface were performed.
In-plane measurements were carried out to assess planes perpendicular to the sample surface such as (100) and (110). The XRD device used for this purpose has the special ability to tilt the line shaped beam by 90°, so that its full line height can be sent in parallel into the film to probe the material. Without this option, only a line section of the height of the film thickness would be probing the sample volume. The 90° tube tilt thus improves the obtained signal intensity significantly. However, the beam is transmitted into the sample via Snellius angle α, and α has to be set by optimizing the intensity of a known signal, which is a non-trivial alignment. As a result, the scattering vector Q is not lying perfectly parallel to the sample surface and thus not perfectly perpendicular to the (xy0) planes to be probed. A flank of the proper Bragg peak is therefore recorded, and the resulting error is too large to allow accurate measurements. In-plane measurements were thus only performed for preliminary access to the a=b dimension. Fig. 7.7 shows a typical in-plane map generated for an Al-O-N sample containing 7.2% O.

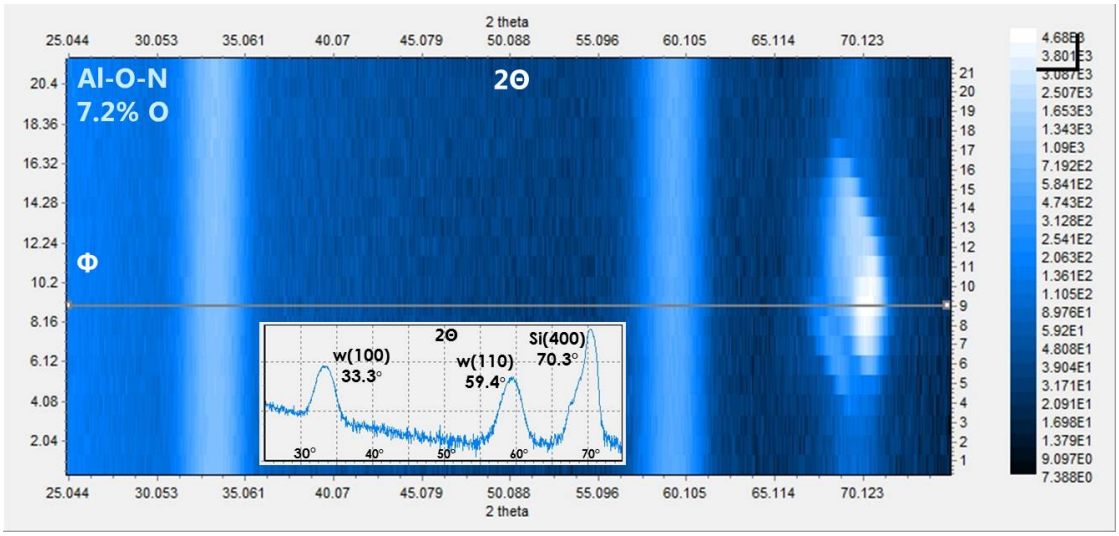

Figure 7.7: In-plane XRD map plotting 2θ versus ϕ (presented as measurement number) for an Al-O-N sample containing 7.2%O. 21 θ-2θ scans from 25-75° were recorded in 0.2° ϕ increments over a ϕ range of 4.2°. A diffractogram derived from the horizontal map cross section delineated in gray is included. Si(400) was measured at 70.3° and has a low 2θ shoulder arising from the wurtzite peak (200). (100) and (110) of wurtzite were measured at 33.3° and 59.4° respectively over the whole ϕ range.

Si(400), theoretically expected at 69.20° in 2θ[12], is found at a higher value of 70.3°, which illustrates the inaccuracy of the method. The positions of the measured peaks cannot be given with higher precision than that shown in fig. 7.7 due to broad signals. To the left of the Si(400) peak, the Al-O-N wurtzite peak (200) generates a shoulder.

Wurtzite (100) and (110) are at 33.3° and 59.4°, while the theoretical values for O-free AlN are 33.26° and 59.44° in 2θ[145], respectively. A right shift in the wurtzite peaks, which would indicate a lattice shrinkage in the (100) and (110) directions for the sample with 7.2%O, is not present.
A feature that is clearly observed in the in-plane map is the fiber texture of the sample, as already seen in the PFs (fig. 7.6). The fiber texture here is shown by the signal intensity of the wurtzite peaks that remains at the same level for the entire ϕ range scanned, also for wurtzite (200). Si, in contrast, present as a single crystal in the wafer, has a peak only visible for a defined ϕ range comprising around 15 measurements. Si(400) superimposes wurtzite (200) in that ϕ range.
It should be noted that for the (xy0) peaks of wurtzite, the same map is obtained if 2θ instead of θ-2θ scans are recorded over the same ϕ range due to the fiber texture of the sample. The Si(400) peak, however, would not be detected if the beam incidence is not at 34.6° with respect to Si(400).

Asymmetric θ-2θ scans recording the wurtzite peaks (105), (104) and (103) were performed to achieve a more accurate and precise assessment of the lateral lattice shrinkage of the crystallites. In the fiber textured samples, the plane normals N of each of these

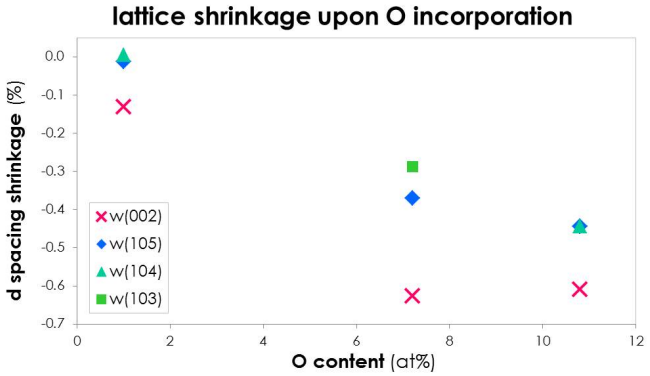

d spacings	AlN (34475)		Al-O-N **1.0**% O				Al-O-N **7.2**% O				Al-O-N **10.8**% O			
	2Θ	d [nm]	2Θ	d [nm]	Δd	Δd %	2Θ	d [nm]	Δd	Δd %	2Θ	d [nm]	Δd	Δd %
w(**002**)	36.07	0.24900	36.09	0.24867	-3.26E-4	-0.13	36.28	0.24744	-1.56E-3	-0.63	36.27	0.24748	-1.52E-3	-0.61
w(**105**) τ=20.28	111.22	0.09342	111.24	0.09341	-1.25E-5	-0.01	111.84	0.09307	-3.45E-4	-0.37	111.97	0.09300	-4.16E-4	-0.45
w(**104**) τ=24.79	86.02	0.11301	86.02	0.11301	4.31E-6	0.00					86.50	0.11251	-5.03E-4	-0.44
w(**103**) τ=31.63	66.12	0.14132					66.33	0.14091	-4.06E-4	-0.29				

Figure 7.8: d spacing shrinkages for the wurtzite lattice dimensions (002), (105), (104) and (103) for samples containing 1.0%, 7.2% and 10.8% O. The plot shows shrinkage values in % relative to pure AlN[145]. The corresponding numbers are listed in the table. The wurtzite peaks are given with their τ relative to (002). Blank cells indicate unmeasured data points.

planes lie on a cone surrounding the sample surface normal which corresponds to the (002) direction. In order to bring the scattering vector Q onto N of a plane for a measurement, the sample needs to be tilted by the angle τ corresponding to the angle between (002) and the appropriate tilted plane. (105) needs the least tilt of τ=20.28°, (104) needs a tilt of τ=24.79°, and (103) needs the most tilt of τ=31.63°. These τ angles were set through the

ψ-tilt in the Eulerian cradle of the diffractometer during the asymmetric XRD measurements. Fig. 7.8 shows the measured d spacing shrinkages of the (105), (104) and (103) planes and tabulates the corresponding values for three samples containing 1.0%, 7.2% and 10.8% O. In order to compare the shrinkages between the dimensions, the values for pure AlN were used as a reference[145], and the changes in d are given relative to those. (002) was taken over from the symmetric θ-2θ measurements as shown in fig. 3.1a) for the relevant samples. Selected measurements were carried out as listed in the table in fig. 7.8. The slope of the shrinkages of the wurtzite dimensions (105), (104) and (103) follows the same qualitative trend as that of (002), but to a lesser extent. (105) shrinks by -0.4% with O contents between 0-7.2% and then maintains this shrinkage level for increasing O content. (104) shows congruent data points for 1.0% and 10.8% O (7.2% O not measured). (103) shows a less strong shrinkage of -0.3% in a sample with 7.2% O (1.0% and 10.8% O not measured). These results indicate that the cell lattice shrinks in all directions. The shrinkage in the c direction is stronger than in the a=b direction; the degree of shrinkage follows the order $c_{(002)} > d_{(105)} \simeq d_{(104)} > d_{(103)}$.

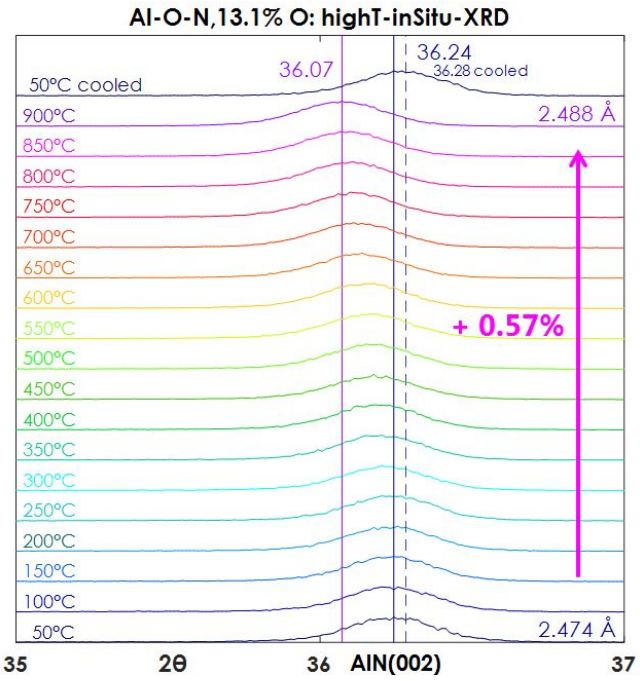

Figure 7.9: HT*is*XRD on an Al-O-N film containing 13.1% O. Thermally equilibrated measurements were taken with Cu Kα in 50°C steps up to 900°C. Following this, the sample was cooled back down to 50°C.

As reported in section 3.5, high temperature *in situ* X-Ray Diffraction (HT*is*XRD) shows that Al-O-N films are thermally inert and stable up to 900°C. Fig. 7.9 shows a (HT*is*XRD) heating series for an Al-O-N film containing 13.1% O. At 50°C, the (002) peak is recorded at 36.24°. On heating up to 900°C, the peak shifts to reach a lower 2θ of 37.07. This corresponds to a d spacing increase of 0.57% from 0.2474 nm at 50°C to 0.2488 nm at 900°C due to thermal expansion. Upon re-cooling the sample down to 50°C, (002) moves back to 36.28°C, a highly similar position as observed initially. No additional peaks are observed in the diffractogram. This test indicates that the system is inert up to 900°C. A number of (002) fiber textured samples were measured and all showed the thermal reversibility. This indicates that the samples are in a thermodynamically stable or metastable state of high inertness.

Al-Si-O-N

Diffractograms of Al-Si-O-N are more complex and cannot be correlated with a single parameter such as the total concentration of O plus Si (O+Si). In general, four types of θ-2θ diffractograms can be distinguished. Fig. 7.10 shows these. The first Al-Si-O-N

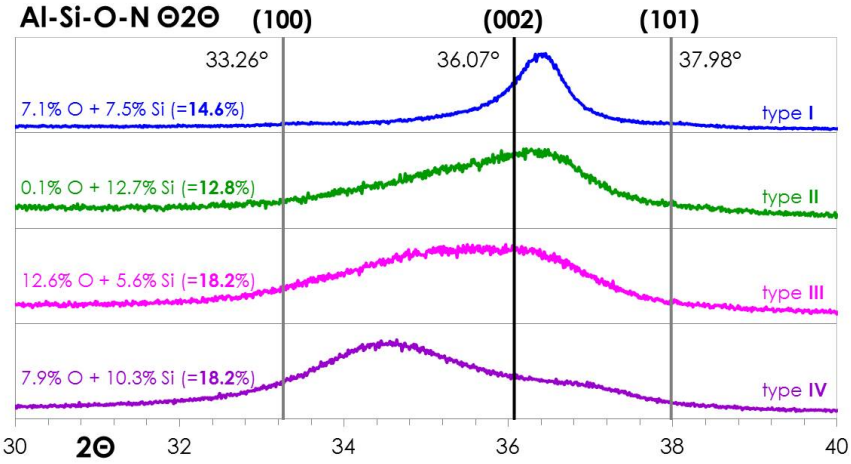

Figure 7.10: Diffractograms of Al-Si-O-N derived from symmetric θ-2θ scans with Cu Kα. Normalized diffractograms of samples with O contents in the range 0.1-12.6% and Si contents in the range 5.6-12.7% are shown between 30-40° in 2θ. Diffractograms are distinguished into type I (blue), type II (green), type III (magenta) and type IV (purple). The positions of the Kα_1 wurtzite AlN reference peaks[145] at 33.26 for (100), at 36.07 for (002) and at 37.98 for (101) are shown in black and gray.

diffractogram type I shows one dominant peak at 36.4°, and two much weaker ones at 33.5° and at 38.1°. These possibly originate from right shifted wurtzite (002), (100) and (101) peaks, respectively. Type II shows one peak at 36.4° with a tail extending towards lower 2θ, ending at 32.5°. From this it can be concluded that wurtzite (002) is the major component. The tail towards (100) may arise from an ordered phase with high variation in d. Type III exhibits one broad peak. This can be attributed to a continuation of type II, with a decreased (002) and increased (100) portion. In type IV, the lower 2θ peak, now found at a right shifted (100) position of 34.5°, clearly prevails.
Table 7.1 lists the samples obtained for each diffractogram type with their chemical composition. An unambiguous assignment of the changes in diffractograms to changing total concentration of O+Si cannot be made. There is a trend for films with increasing O+Si content to give diffractograms with a higher type number. In contrast to Al-O-N, Al-Si-O-N films of the compositions reported here do not have a unique texture in growth direction z. However, a preference for (002) or (100) oriented along z is seen for most samples, and therefore the crystallite orientation distribution is not random. Films with higher Si and/or O contents than shown above were amorphous.

Table 7.1: The four diffractogram types observed for Al-Si-O-N coatings and the corresponding samples. Their O and Si contents as well as the sum are given in at%.

type **I** content (at%) O+Si=**O+Si**	type **II** content (at%) O+Si=**O+Si**	type **III** content (at%) O+Si=**O+Si**	type **IV** content (at%) O+Si=**O+Si**
7.1+7.5=**14.6**	7.4+3.3=**10.7**	0.0+15.3=**15.3**	0.1+17.6=**17.7**
9.6+7.3=**16.9**	0.1+12.6=**12.7**	12.6+5.6=**18.2**	0.1+17.6=**17.7**
11.4+5.7=**17.1**	0.1+12.7=**12.8**	14.9+6.4=**21.3**	7.9+10.3=**18.2**
0.2+20.1=**20.3**	0.1+12.9=**13.0**	19.2+6.0=**25.2**	8.7+10.2=**18.9**
	1.5+13.4=**14.9**		7.1+11.7=**18.8**
	13.0+5.4=**18.4**		9.2+10.0=**19.2**
	15.4+5.7=**21.1**		8.6+10.7=**19.3**
	15.4+5.8=**21.2**		5.6+17.4=**23.0**

7.3 Cross-sectional micro- and nanostructure

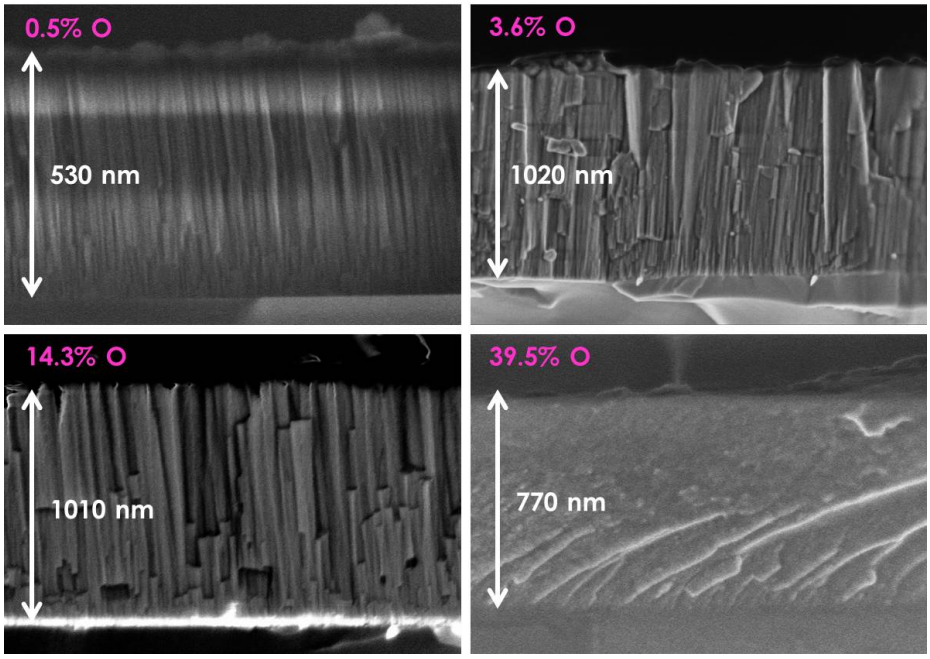

Figure 7.11: SEM cross sections of Al-O-N thin films with differing O contents of 0.5% (top left), 3.6% (top right), 14.3% (bottom left) and 39.5% (bottom right).

In the paper in section 3.3.2, the cross-sectional morphology of Al-O-N films was discussed with TEM images (fig. 3.2). Additional SEM images are given here in fig. 7.11, showing cross sections of four Al-O-N coatings containing 0.5%, 3.6%, 14.3% and 39.5% O. An AlN film with a residual O amount of 0.5% shows columnar growth with column widths of 10-50 nm. The columns are of smaller diameter in proximity of the substrate due to competitive crystallite growth[6,128]. Within the first 100 nm of film growth, they collapse to broader columns which maintain a constant width upwards for the rest of the coating. O addition causes the columns to broaden. In a film with 3.6% O, the columns are still narrow at the substrate but widen conically towards the surface of the coating. Columns in a coating of 14.3% O are straighter and broader with approximately 100-150 nm. When the O content is further increased, the columnar morphology disappears, such that a film with 39.5% O shows a glass-like, conchoidal fracture.

7.4 Chemical states

Al-O-N

As reported in section 3.3.3, XPS expriments show that all species in Al-O-N experience an increase of the binding energy (BE) of their core e^- upon increasing O content. Additionally, the FWHMs of their photo e^- lines vary relative to the lowest value they show by more than a factor of 1.15 upon changing O contents, which indicates that every element undergoes a significant disorder broadening[121,72,24]. The reasons are discussed in section 3.3.3.

In section 3.3.3, it is reported that films of the amorphous solid solution regime (III) exhibit a second N 1s photo e^- line. This second peak emerges at a BE between 401.8-402.50 eV and is thus approximately 6 eV higher in BE than the usual N *1s* photo e^- line. The higher BE indicates that this second peak arises from (partially) oxidized N, which is the case for N bound to O in the amorphous network. Fig. 7.12 shows the area of this peak as a percentage of the total peak area for N *1s*.

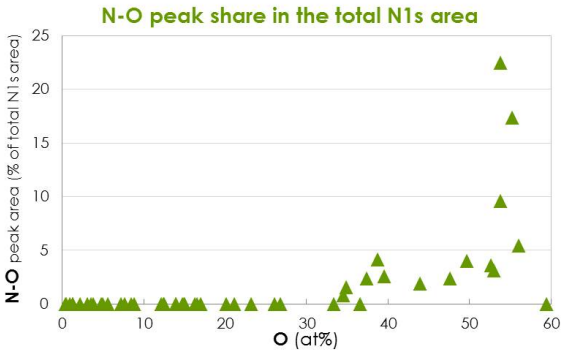

Figure 7.12: Percentage of the high-BE N-O peak area in the total N *1s* peak area of spectra of Al-O-N thin films.

N-O interactions were not detected in films with less than 30% O. Above this level, the area of the N-O peak remains below 5% until 55% O has been incorporated in the film. As seen in fig. 7.12, there is a large variation in the area of the N-O peak at an O concentration of approximately 55%. In the literature, there is no unambiguous assignment of

this peak to an oxidized state of N. It has been attributed to both N^{1+} [154] and N^{2+} [180]. It can be postulated that in Al-O-N investigated for this project, the degree of oxidation of N varies with the proximity of O and the number of bonds formed towards O. Literature reports on further high BE N *1s* components are also available. They assign peaks from 398 to 408 eV to different oxidation states of N [70,96,39,154,180]. The films that exhibit the N-O peak in XPS spectra deposited in this project are amorphous, which is why N can be incorporated with varying bond numbers towards O. These films represent one of the rare cases where a slight overstoichiometry is realized. Since e^- are stabilized in N-O bonds, more N and O can be incorporated than the maximal amount reducible by the Al in the films. It should be noted, however, that in the high O regime of these films, the concentrations of N are low. Samples with around 55% O contain less than 10% N. Therefore, the influence of N-O interactions on stoichiometry is largely redundant and no significant overstoichiometry is measured.

Al-Si-O-N

In the spectra of Al-Si-O-N, BE and FWHM of the photo e^- lines were found to correlate with both the Si and the O content in the films. This is to be expected, since Si and O induce similar phenomena in the material system such as V(Al) generation (section 4.1), nanocomposite formation (section 3.4) and amorphization (section 7.2). Additionally, the XPS measurements of Al-Si-N show similar trends when Si is added [123] as the spectra of Al-O-N show upon addition of O. The best correlations of BE and FWHM for Al-Si-O-N were thus found by analyzing each with respect to the sum of Si plus O. Fig. 7.13 shows BE and FWHM for each component in Al-Si-O-N versus Si+O in atomic percent (at%). To facilitate comparison, the same graph scales are used as in fig. 3.3. Table 7.2 comprises the changes induced in the photo e^- lines for each element in Al-Si-O-N as well as literature values for BEs and Pauling Electronegativities (χ) [183] for elemental, metallic Al and semi-metallic Si and for O and N.

The trends seen in Al-O-N (section 3.3.3) proceed in a similar way in Al-Si-O-N. The lowest Si+O value measured is 10.7%, thus the early trends in Al-O-N below the O solubility limit are not seen in the Al-Si-O-N samples investigated in this project. This is why FWHMs within the spectra of Al-Si-O-N show less variation than those of Al-O-N. The only species to cross the threshold of FWHM broadening by a factor of 1.15 is O. However, it is more relevant to consider Al-Si-O-N FWHMs in comparison with the lowest values obtained in Al-O-N, which are added in darker colors in fig. 7.13 (except for Si). With respect to those, all photo e^- line FWHMs in Al-Si-O-N (except Si *2p*) broaden by more than a factor of 1.15. The FWHM of each species increases to the same value as found for Al-O-N.
Unlike the $BE_{Al\,2p}$ in Al-O-N, that in Al-Si-O-N does not increase on the addition of low amounts of O. An initial plateau is observed at 73 eV up to an O concentration of 30%. Si *2p* is present as an additional photo e^- line and behaves similarly to Al *2p*. $BE_{Si\,2p}$ maintains a level of 100.5 eV up to 30% O and then increases, by a similar ΔBE as

BE_{Al2p}, to 102.5 eV. The reason for the similarity between the BEs of Al *2p* and Si *2p* is probably that both Al and Si act as e^- donors. BE_{N1s} and BE_{O1s} evolve qualitatively in the same way, with an initial plateau followed by an increase, but with a lower ΔBE of 1 eV or less. The similarity between the FWHMs of N *1s* and O *1s* is probably due to both O and N being e^- acceptors.

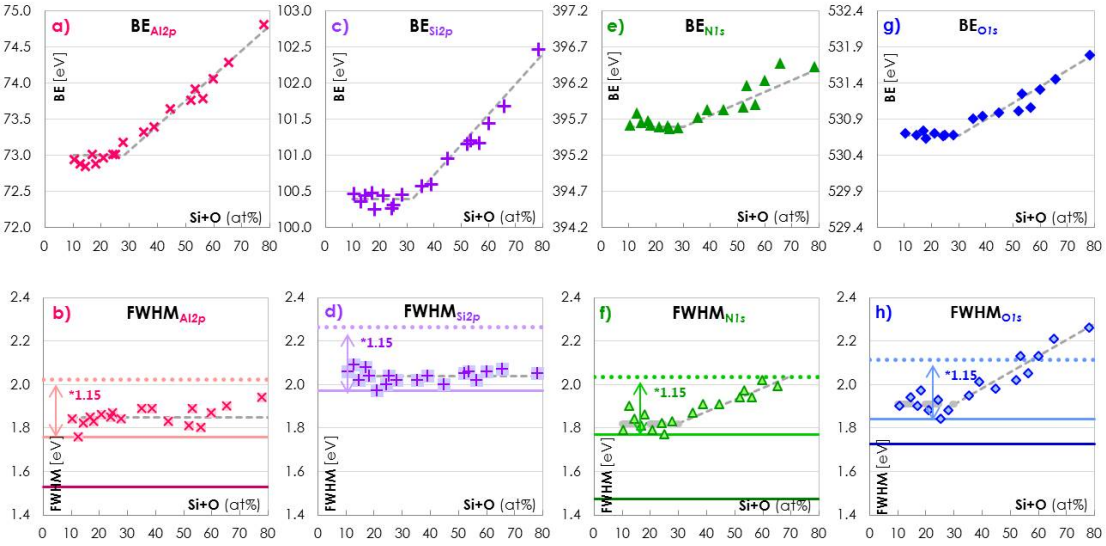

Figure 7.13: BEs [eV] (top) and photo e^- line FWHMs [eV] (bottom) of Al *2p* (pink crosses), Si *2p* (purple plus signs), N *1s* (green triangles) and O *1s* (blue rhombi) in Al-Si-O-N with rising Si+O content. Gray dashed lines have been added as visual guides. The FWHM disorder broadening band by a factor of 1.15 (*1.15) for each species is indicated with a solid line for the lower and a dotted line for the upper limit. The lower limit found in Al-O-N is shown by a darker solid line.

Table 7.2: Changes in core e^- BEs and photo e^- line FWHMs [eV] upon O incorporation into Al-Si-O-N. Elemental (el.) BEs and χ for metallic Al, semi-metallic Si, N and O are given from literature for comparison.

atom (line)	BE range	ΔBE	FWHM range	ΔFWHM	el. BE	χ
Al (*2p*)	72.9 - 74.8	1.9	1.76 - 1.94	0.18	72.8 [34,61]	1.5 [183]
Si (*2p*)	100.3 - 102.5	2.2	1.97 - 2.09	0.12	99.6 [108]	1.8 [183]
N (*1s*)	395.6 - 396.5	0.9	1.77 - 2.02	0.25	405.3 [170]	3.0 [183]
O (*1s*)	530.6 - 531.8	1.2	1.84 - 2.26	0.42	538.8 [170]	3.5 [183]

$FWHM_{Al2p}$ and $FWHM_{Si2p}$ show no dependence on Si+O, while $FWHM_{N1s}$ and $FWHM_{O1s}$ increase after addition of 30% O.

One of the Al-Si-O-N samples that were analyzed, containing 52.3% Si+O, led to a spectrum with the additional oxidized N *1s* peak that has been found in Al-O-N and could be assigned to N-O interactions (section 3.3.3 and section 7.4). It amounted to 2.6% of the total N *1s* area.
Two data points were omitted, namely $FWHM_{N\,1s}$ of a sample with 78.3 % Si+O and $BE_{O\,1s}$ of a sample with at 13.0% Si+O. These are samples with very low N content (resulting in effectively Al-Si-O) and with very low O content (Al-Si-N), respectively, making the evaluation of the N and the O peak unreliable.

Al-O-N ∞ Al-Si-O-N

Conclusions about both material systems are summarized in the following.

- All species in Al-(Si-)O-N exhibit similar qualitative trends to each other. Their BEs all rise with O(+Si) addition due to progressive oxidation.
- The e^- donors (Al and Si) show similar quantitative trends to each other as do the e^- acceptors (N and O). $\Delta BE_{Al\,2p/Si\,2p}$ is approximately 2 eV, while $\Delta BE_{O\,1s/N\,1s}$ is about 1 eV. After the O/Si solubility limits in wurtzite have been reached, $FWHM_{Al\,2p/Si\,2p}$ do not vary with O(+Si), while $FWHM_{N\,1s/O\,1s}$ increase after addition of 30% O.
- Two distinct threshold values are observed, the first is at 8% O in Al-O-N and the second at 30% O(+Si) in both systems. These values correspond to the borders between the three Al-O-N material evolution regimes (I), (II) and (III) (section 3.4).
- In A-Si-O-N, the BEs of Al, O and N are slightly higher than in Al-O-N (by 0.3-0.4 eV for Al, 0.2-0.3 eV for N, and 0.2-0.4 eV for O).

7.5 Hardness and elasticity

In section 3.5, the changes in HD and E assessed by nanoindentation of Al-O-N coatings with increasing O content is reported. Fig. 7.14 shows the HD of both Al-O-N (blue rhombi) as well as Al-Si-O-N (magenta dots) versus O and Si contents in a 3D plot.

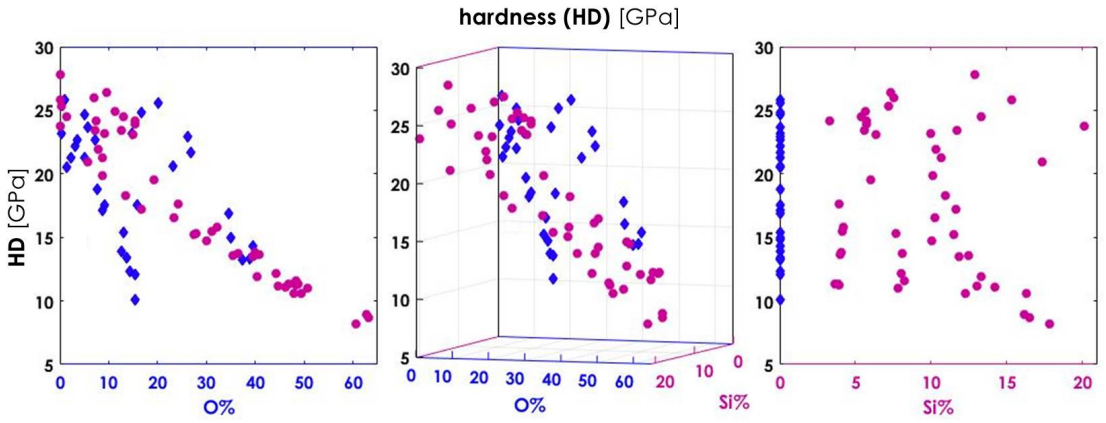

Figure 7.14: 3D diagram of HD [GPa] versus O and Si content in thin films of Al-O-N (blue rhombi) and Al-Si-O-N (magenta dots). The spread of n in Al-Si-O-N (on the right) is due to different O contents of the coatings.

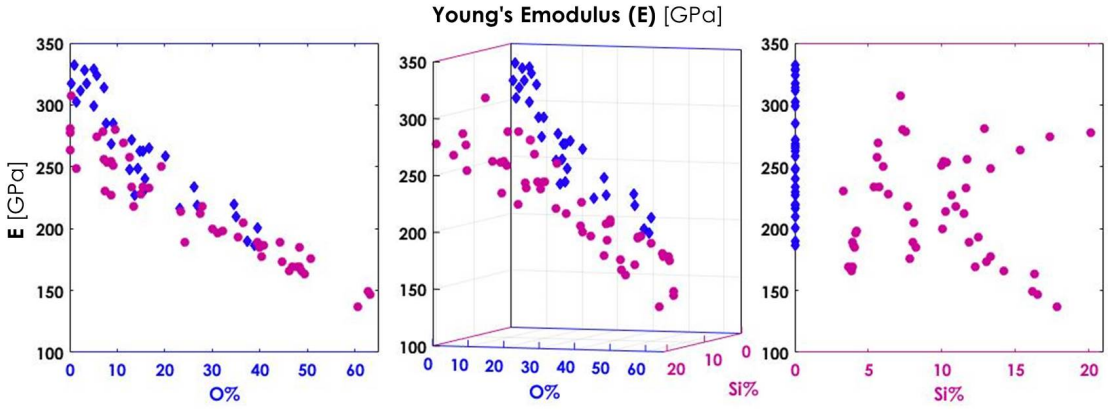

Figure 7.15: 3D diagram of E versus O and Si contents in thin films of Al-O-N (blue rhombi) and Al-Si-O-N (magenta dots). The spread of n in Al-Si-O-N (on the right) is due to different O contents of the coatings.

Both systems exhibit a strong HD dependence on O but none on Si. Al-O-N shows HD values between 10-27 GPa and a dip in HD in the fiber textured nanocomposite regime (IIa), probably caused by H incorporation exclusively in this regime (section 3.4 and section 7.1). Although the origin of H incorporation can only be speculated, a connection between the dip in HD and the H incorporation is highly probable. H atoms interrupt

the bonding continuation in a covalent network. They act as terminating points, as they can only form one single bond. This can reduce HD values significantly. Al-Si-O-N exhibits a continuous decrease in HD from values around 26 GPa to around 8 GPa with an O content increasing from 0 to 65%. In the literature, conform values for the binary systems AlN[122,109,81], Al_2O_3[80] and SiO_2[8] are reported. In summary, O incorporation in both material systems leads to a reduction in HD.
At the same time, the Young's modulus E is also reduced by O, which indicates a higher elasticity of the coatings through O incorporation. Fig. 7.15 shows the evolution of E with respect to O and Si for Al-O-N (blue rhombi) and for Al-Si-O-N (magenta dots). Again, a strong dependence on O is found and none on Si. The Al-O-N values of E are higher over the entire O range than for Al-Si-O-N. The HD dip observed for Al-O-N is not detected in E.

To assess the mechanical performance of a coating, HD and E should be considered in combination. A coating can, for example, have a high HD, but if its E value is high as well, the material will be inelastic and thus brittle. A desirable combination for a tough coating is a high HD with a moderate E. Lower E values are also advantageous to reduce the "eggshell effect". This phenomenon can occur in samples made of hard, inelastic films on softer, more elastic substrates. The coatings can then crack upon force, similar to the hard, rigid shell of an egg around its liquid content. In the samples for this project, the substrate Si(100) is with 13 GPa in HD[131] and 130-170 GPa in E[67] softer and more elastic than the Al-(Si-)O-N films. Adapting the coating elasticity to that of the substrate thus reduces the risk of failure. A useful parameter is the HD/E coefficient. A large HD/E signifies a high resilience and fracture toughness. HD/E versus O content in Al-O-N and Al-Si-O-N films is reported in section 3.6. Fig. 7.16 shows HD/E for Al-O-N (blue rhombi) and for Al-Si-O-N (magenta dots) versus O as well as Si contents in a 3D plot.

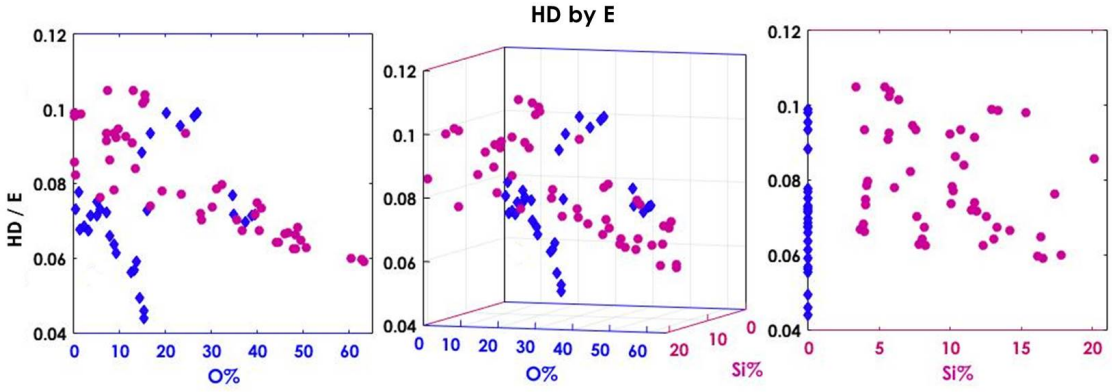

Figure 7.16: 3D diagram of HD/E versus O and Si contents in thin films of Al-O-N (blue rhombi) and Al-Si-O-N (magenta dots). The spread of n in Al-Si-O-N (on the right) is due to different O contents of the coatings.

Both material systems show again a dependence on O and none on Si. A trend can clearly be seen for Al-Si-O-N, where increasing O correlates with decreasing HD/E. In the region of 0-15%O, Al-Si-O-N performs better, reaching HD/E values up to 0.11. HD/E of Al-O-N with 8-16% O of regime (IIa) is affected by the dip in HD, leading to low HD/E values down to 0.04. For films with 16-30% O, Al-O-N belonging to the regimes (IIb) yields better HD/E values than Al-Si-O-N up to 0.1. From 30% O upwards, Al-O-N and Al-Si-O-N show the same HD/E trend with values decreasing from 0.08 to 0.06.

7.6 Residual stress

Cracks as residual stress consequence: Theoretical background

Tensile or compressive stress can cause cracks of regular, periodic patterns and striking appearance. When the compressive force in a film is stronger than the adhesion to the substrate, the film starts to buckle and delaminate, and eventually to crack. The "telephone cord", shown in fig. 7.17a), is an often observed fracture pattern that can be generated as soon as the film buckling stress is surpassed by a factor of four[179]. Thin

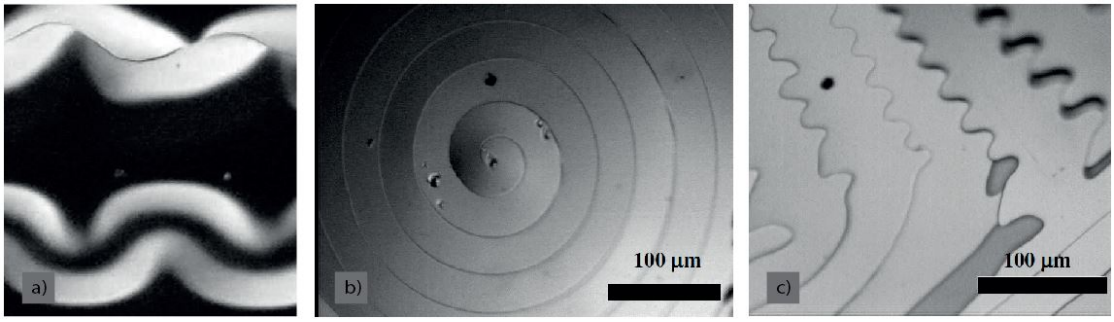

Figure 7.17: Crack patterns in stressed materials (adopted from[179]). a) shows an optical micrograph of a compressive "telephone cord" delamination in a W/Al/Cu system; b) and c) are optical images of tensile spiral and sinusoidal cracks, respectively, observed side by side in Mo/Si multilayers.

films can withstand higher stress loads of several GPa in compression, while they crack more easily under tension. Ornate tensile crack figures such as spirals in 7.17b) and sinusoidal cracks in c) can result. A more commonplace cracking behavior of tensilely stressed brittle films is termed "mud cracking" due to its similar appearance to drying earth, as shown in fig. 7.18. This type of cracking has been investigated by Thouless in a first approach in 1990[168]. The underlying assumption was a thermodynamically based minimum crack spacing that a simultaneously propagating crack pattern could adopt. It was concluded that cracks separated by more than eight times the film thickness were weakly interacting and that the maximum crack density was increasing with film stress and/or film thickness as soon as the necessary critical conditions for crack formation were exceeded. This model was revised shortly afterwards[169] by including that crack propagation is not an isochronic event but proceeds sequentially. The crack spacing in

the new considerations was controlled by the tensile strain, the fracture resistance and the elastic constants of the film and was found to be proportional to the square root of the film thickness. While thermodynamic energy-minimizations had laid the fundament for the initial approach, the following proposition focused on kinetics in terms of the nucleation and propagation of cracks and showed higher congruence with experimental observations. A further kinetic path was trod by Hutchinson and Suo[68], who assumed crack propagation - instead of vertically down from the film surface - as tunneling in parallel to the latter, in a process named "channeling". Beuth[10] distinguished between two different cracking modes. The crack tip could either stall in the film material somewhere along the cross section or propagate all the way down to the film-substrate interface. Criteria for the estimation of crack extension and substrate curvature change due to cracking were given. While all the deliberations made before by the authors above were based on identical elastic properties for both substrate and brittle film, Beuth elaborated stress intensity factors by making use of Dundurs parameters α and β[36,37]. These take into account different elastic properties of substrate and film and set their shear moduli and Poisson ratios (in the form of Muskhelishwili's constants) into mutual relation. Only β is dependent on the Poisson ratios, while being also linearly dependent on α[143], and is not relevant to the discussion here. α can be expressed as a relation of the Young's moduli of film and substrate. Positive α values (up to $+1$) represent systems in which the film is stiffer than the substrate; negative ones (down to -1) in turn are systems with stiffer substrates than films. For film and substrate of equal elastic quality, both α and β are zero. When film and substrate material are switched, α and β simply reverse their algebraic signs.

Figure 7.18: Drying earth layer (near Page, Arizona) that cracked open on a sandy background. The single patches are contracting and flexing upwards due to tensile stresses.

Shenoy *et al.*[149] developed further considerations for substrates and films of differing elastic characteristics, which represent most cases. They observed triangular patterns, displaying 120° and 60° angles between cracks, in gallium nitride (001) (GaN(001)) films on Si(111) wafers. They attributed this to a bursting along (100) planes, as these have the lowest surface energy. An important observation was that cracks belong to different generations: A first generation is deep (appearing dark and broad in a microscope picture) and widely spaced by around 15 times the film thickness. A second generation is thinner and of a finer nexus, with spacings of two to five times the film thickness. They modeled crack patterns by calculating crack depths and distances as functions of the Dundurs parameters, the crystal lattice mismatch stress between film and substrate and

the film thickness. Energy balancing and minimization (thermodynamics as in ref.[168]) as well as the driving force for lateral crack propagation (kinetics as in ref.[68] and in ref.[169]) were taken into account. This supported the proposition that supposedly both thermodynamics and kinetics contribute significantly to cracking. The results obtained by Shenoy *et al.* were sensitive to only the α Dundurs parameter. β did not show a large influence and was thus kept constant. The following two cases were distinguished:

- $\alpha>0$ (**film stiffer than substrate**):
  The stress intensity factor **in**creases (towards indefinitely large)
  when the crack approaches the film-substrate interface.

- $\alpha<0$ (**substrate stiffer than film**):
  The stress intensity factor **de**creases (towards zero)
  when the crack approaches the film-substrate interface.

The modeling by Shenoy *et al.* further suggested that a higher film stiffness compared to that of the substrate (higher α) resulted in a lower stress threshold for crack initiation, an increased spacing between cracks and in turn to a lower channeling driving force.
In summary, Shenoy *et al.* concluded that the stiffer a film is in comparison to the substrate, (1) the less force is needed for crack nucleation, (2) the more likely it is that the crack propagates through the entire film thickness into the substrate, and (3) the less dense the final crack network will be[149].

Residual stresses measured in Al-(Si-)O-N coatings

The residual stresses in Al-O-N coatings with varying O contents are reported in section 3.5. Fig. 7.19 shows the residual film stress of both Al-O-N (blue rhombi) and Al-Si-O-N (magenta dots) coatings versus O and Si contents in a 3D plot. Only the Al-O-N system shows a dependency of the residual stress on the chemical composition, while stresses in Al-Si-O-N are independent of both the Si and the O content. All stresses measured, whether tensile or compressive, are below 1 GPa in absolute value, and most films have a compressive residual stress between -0.2 GPa and -0.4 GPa. The relatively low stress level does not affect most of the films in terms of their optical appearance. They are featureless and show no stress induced damage.

The exception is Al-O-N in the crystalline solid solution regime (I) with of 1-8% O. The residual stress in such films is tensile and amounts to up to 0.72 GPa, which is high enough to lead to visible stress relaxation cracks (section 3.5). Fig. 7.20 shows optical microscope images of cracked films.

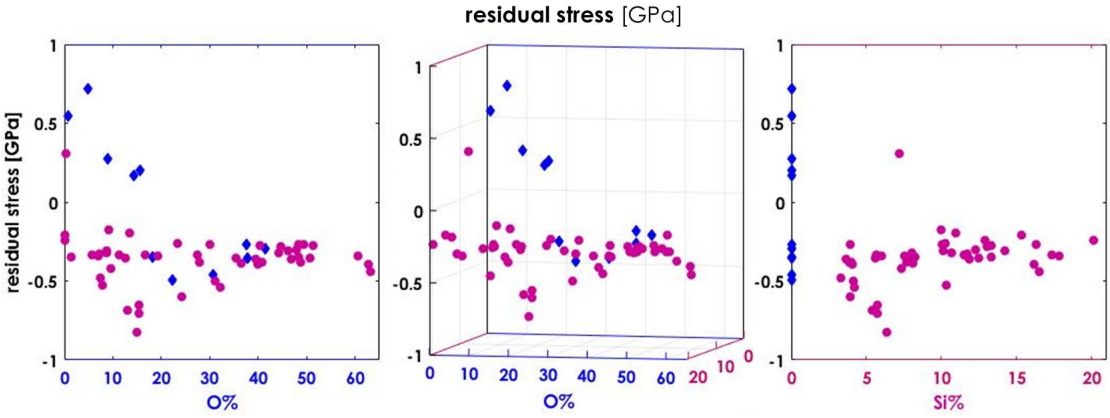

Figure 7.19: 3D diagram of the residual stress σ versus O and Si contents in thin films of Al-O-N (blue rhombi) and Al-Si-O-N (magenta dots).

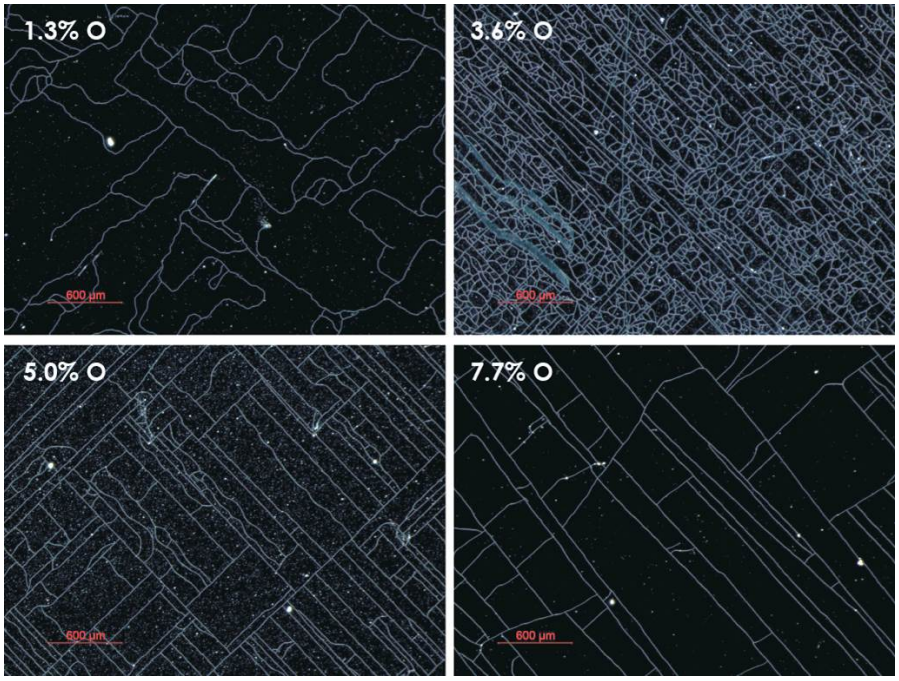

Figure 7.20: Cracks in Al-O-N films containing 1-8% O imaged with an optical microscope at 40x magnification (a scale bar of 600 μm is inserted in red). Brightness and contrast in the pictures were adapted to visualize the cracks. The individual film samples, containing 1.3%, 3.6%, 5.0% and 7.7% O, each show a different type of crack pattern.

The crack pattern varies with increasing O content. While AlN with an O content of around 0.5% shows no damage, cracks start to form from 1% O on. A film containing 1.3% O has a fine, winding crack pattern of low density. Often, the start or end of a crack line is at a pinhole defect, a phenomenon also observed by other authors[91]. Such a crack

pattern hints at a rather ductile material and moderate stress levels. Increasing the O content to 3.6% leads to broader, straight cracks of much higher density. This indicates that the film has become more brittle and the stress level higher. Upon increasing the O content further to 5.0% or 7.7%, the cracks remain straight, but the crack density continuously decreases due to decreased stress levels (figs. 3.5 and 7.19). Above 8% O, the cracks disappear completely. The residual tensile stress in Al-O-N with more than 8% O is around 0.2 GPa, low enough to allow the thin films to stay intact. The stress in Al-O-N becomes compressive above an O content of 16%. As has been shown in section 7.2, this crossover coincides with the loss of pure (002) texture due to the alignment of very small crystallites in all directions.
Crack hierarchy[149] is well visible in the Al-O-N films. Lower stress, as at 1.3% O, generates meandering cracks that form kinetically slowly and close to thermodynamic equilibrium. Higher stress leads to straight cracks that fracture quickly, far from equilibrium and thus with high energy release. At 5.0% O, two crack generations are clearly distinguished. There are rapid, long, straight cracks, from which finer, more curved and shorter cracks emanate. They terminate when another crack is encountered.

The films with an O content in the region of 1-8% consist of fiber textured wurtzite

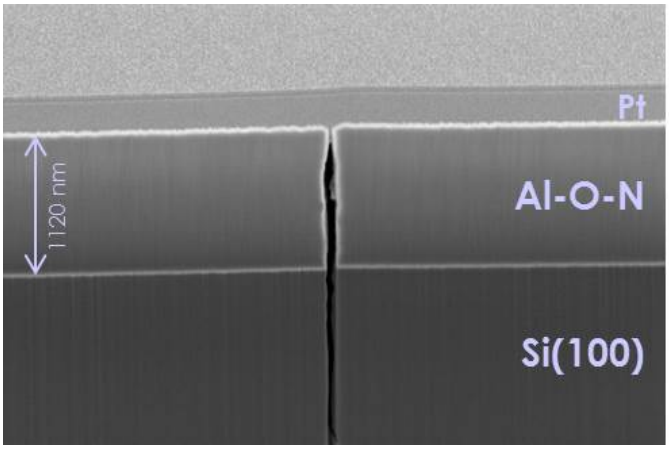

Figure 7.21: GaFIB-SEM cross section through a crack propagating in line of sight corresponding to the Si(100) plane. The Al-O-N film on the Si(100) substrate is covered by a Pt layer used for the GaFIB cut.

crystallites. Wurtzite belongs to the hexagonal crystal system having a sixfold symmetry, which however averages out in the plane of the coatings due to the fiber texture. The crystalline structure of the films is therefore not assumed to be connected to the film cracks. The crack pattern observed is rectangular with angles close to 90°, which relates them to the cubic Si(100) substrate. Crack propagation follows the (100) planes of the wafer, not the (110) planes (section 3.5). One reason for this is that the mismatch in the E from Al-O-N (around 330 GPa, as shown in fig. 7.15) to Si(100) (130 GPa) is larger than to Si(110) (169 GPa)[67]. The tensile force experienced on the Si(100) planes is thus stronger. Another reason is that the free surface energy of Si(100) with 1.36 Jm^{-2} is

lower than of Si(110) with 1.43 Jm^{-2}. These values were experimentally determined[40] and the trend confirmed by theoretical calculations[184,50]. Exposing a Si(100) plane to air due to a crack thus requires less surface energy than exposing a Si(110) plane.
The fractures transgress the film and propagate down into the substrate, as can be seen in the GaFIB-SEM cross section in fig. 7.21. This indicates that the adhesion of the film to the Si substrate is strong. If the adhesion were weak, the coating would peel off the substrate due to the tensile stress instead of cracking through the substrate surface. Moreover, the image in fig. 7.21 is consistent with the predication that for a stiff film on a compliant substrate (α>0), a tensile crack proceeds down into the latter[149].

The origin of residual stresses

Thin films deposited by PVD and other techniques often exhibit residual stress. The film growth morphology and composition and mismatches in the mechanical properties between substrate and coating contribute to this stress. Growth morphology types of polycrystalline thin films have been characterized in Structure Zone Models (SZM)[166,6,4]. The energy involved in the film growth largely determines the morphology. A useful parameter in SZMs is thus the "reduced temperature" $\frac{T_s}{T_m}$, *i.e.* the ratio of the deposition temperature (T_s) to the material melting temperature (T_m). Most SZM distinguish film growth modes into a "zone I" with $0<\frac{T_s}{T_m}<0.2$, a transition "zone T" with $0.2<\frac{T_s}{T_m}<0.4$ and a "zone II" with $0.4<\frac{T_s}{T_m}<1$ (see references for details).
As well as from temperature, the energy of a deposition process can also originate from the bombardment with energetic projectiles. A simplified approach in DC depositions is to use the particles sputtered from the target plus the sputter gases involved in the process. These components comprise of neutrals as well as ions, and potentially charged and uncharged clusters. At low pressure, these species can achieve a mean free path λ that is longer than the target to substrate distance, which allows them to fly unhindered towards the substrate and deliver energy upon impinging on it. If a higher flux rate of projectiles is required, ionized species can be guided towards the substrate via a magnetic field. The magnetic field can be generated by permanent magnets[186] or magnetic coils[127,172]. High Power Impulse Magnetron Sputtering (HiPIMS) can be used to enhance the ionization rate[97,98]. A bias can be set onto the substrates to increase the energy of impinging projectiles. These additional energy contributions direct film growth to generate coatings with a compressive stress state.

Within a given chemical composition, impurities such as O have been observed to favor compressive stress. This phenomenon has only partly been explained by invoking several mechanisms. These mechanisms describe the reaction of an impurity with deposited material to effect crystal growth termination, grain boundary formation, renucleation and hindrance of atom rearrangement[185].
The stress caused by a mechanical mismatch between substrate and film is enhanced if it is accompanied by a difference in the thermal expansion of the two materials. Films deposited via plasma experience a heat flux from the process, and often additional heat-

ing is applied. If substrate and film exhibit different thermal expansion coefficients, a thermal stress σ_T is present after cooling the system from deposition to room temperature. The larger the mismatch in the expansion coefficients of substrate and film, and the higher the process temperature, the greater the residual thermal stress will be.

An additional source of residual stress is that film growth proceeds in diverse phases, and these in turn have different influences on stress. Often a stress gradient throughout the film is established. Stress evolution during film growth and the mechanisms leading to stress have been studied in detail[79,1,74,21,185] and can be followed *in situ* via Multibeam Optical Stress Sensor (MOSS) measurements[148]. Nucleation initiates film growth. The first few atoms solidify on the substrate and subsequently grow into islands. When these islands expand enough to coalesce, a tensile stress is usually established. This is caused by attractive Van der Waals forces that induce a "zipping effect" between the island borders. Upon growing further, films deposited with low energy input remain tensile, and those deposited with high energy input become compressive.

According to SZM categorization, all crystalline films grown in this project clearly belong to zone I with $\frac{T_s}{T_m} \approx 0.1$ (with T_s=200°, T_m^{AlN}=2227°C[107,38] and $T_m^{Al_2O_3}$=2054°C[84]). However, films within the crystalline solid solution regime with higher O contents exhibit features of zone T. The columns become broader and adopt conical shape, indicating competitive crystallite growth as seen in SEM images (section 7.3). The influence of O on the film properties would thus be described as that of a dopant or "impurity"[185], promoting a film towards zone II. Energetic particles, present in the depositions carried out for this project as the target to substrate distance was kept below the mean free path λ of particles of the sputter flux[121], also influence the growth structure.
The impact of O on the film growth is also seen in the stress evolution measured for Al-O-N films (fig. 7.19), where O incorporation leads to a shift of the residual stress towards compressive.
σ_T in the Al-(Si-)-O-N films on Si(100) and glass is insignificant. According to the corresponding formula[117,12–20], σ_T amounts to 211 MPa (assuming a thermal expansion coefficient of $5{\cdot}10^{-6}$°C^{-1} for *e.g.* AlN and of $2.6{\cdot}10^{-6}$°C^{-1} for Si, and an E of 330 GPa and a Poisson ratio of 0.25 for AlN[189,152,165,121]).

8 Appendix B: Experimental details

8.1 RBS, ERDA and He-ERD for chemical compositions

Chemical compositions were determined by Rutherford Backscattering Spectrometry (RBS), heavy ion Elastic Recoil Detection Analysis (ERDA) and Helium Elastic Recoil Detection (He-ERD). The measurements were performed at the Laboratory of Ion Beam Physics (LIP) at the Swiss Federal Institute of Technology, Zürich (ETHZ). All evaluations of the results were done by or in collaboration with LIP.
For RBS, the thin films were irradiated by 2 and/or 4 and/or 5 MeV ^{4}He. The backscattered beam was analyzed by a Si PIN diode detector placed under 168°. For ERDA, the samples were bombarded by 13 MeV ^{127}I under 18° incidence angle, and recoiling ions were analyzed in an ERDA detector telescope developed at LIP. This detector consists of a Time-of-Flight (ToF) system coupled to a Gas Ionization Chamber (CIG)[82]. For He-ERD, the samples were bombarded by 2 MeV ^{4}He under a glancing incidence angle of 15°, and recoiling H was detected by a Si PIN diode detector under 30° using the absorber foil technique[112].
The compositional contents of Al, Si and the major e^- acceptor - either O or N - were determined by RBS. The minor e^- acceptor content was then refined via N/O ratio obtained from ERDA. This procedure was chosen, as ERDA has a higher sensitivity for light elements, while RBS has a better absolute accuracy for the determination of stoichiometries. He-ERD was used to measure the H contents.
The algorithm RUMP[35] was applied to simulate the spectra obtained with RBS. The derived stoichiometries have an error of +/- 4.5%. For ERDA, custom made analysis software has been used to determine elemental ratios. In cases where depth profiles of concentrations were needed, the DataFurnace code[76] was used to analyze the obtained ToF versus energy histograms. Pure ERDA data errors amount to +/- 7.0%. If the two techniques RBS and ERDA are combined, as for example in the more accurate determination of the minor e^- acceptor content, the error in the result is correlated and propagates to +/- 8.3% via $(4.5^2+7.0^2)^{\frac{1}{2}}$.

8.2 XRD for crystallinity

Crystallinity was assessed by X-Ray Diffraction (XRD). Three different diffractometers were used. The following angle conventions for the setup coordinates were applied: 2θ is the angle between X-ray beam and detector, θ or ω (depending on whether the movement of the detector is coupled to that of the sample or not, respectively) is that between beam and sample surface tilting towards the beam axis, ψ is that between beam and sample surface tilting around the beam axis, φ describes the rotation of the sample around its central surface normal, and τ is the angle between sample surface (congruent with wurtzite (002) planes for crystalline films in this project) and a specific plane family.
Symmetric θ-2θ XRD scans, rocking curves (RCs) and pole figures (PFs) were recorded on a standard Bruker D8 Discover with DaVinci Design (Bruker AXS GmbH, Karlsruhe, Germany). In-plane θ-2θ and asymmetric θ-2θ and 2θ scans measured on a Bruker D8 Discover with DaVinci Design, with a tube rotatable by 90° (Bruker AXS GmbH, Karlsruhe, Germany). High temperature *in situ* X-Ray Diffraction (HT*is*XRD) was carried out on a PANalytical Xpert Pro (Malvern PANalyical B.V., Almelo, Netherlands) equipped with an Anton Paar XRK900 heating stage (Anton Paar GmbH, Graz, Austria). All experiments were carried out using a Cu anode operated at 40 kV and 40 mA. Cu Kβ was suppressed down to 1% by a nickel (Ni) foil of 0.012 mm. For RCs, PFs, in-plane measurements, asymmetric XRD and HT*is*XRD, signals for combined Cu Kα_{1+2} (0.15418 nm) were evaluated. For symmetric XRD, Cu Kα_1 (0.154056 nm) components were extracted. Results were analyzed with software associated with the measurement devices and with Matlab (The MathWorks, Inc., Natick, USA).
Symmetric θ-2θ XRD scans yielded information about crystal planes parallel to the sample surface, *i.e.* (00z) planes. They were recorded with the beam in line-focus and parallelized by a primary Göbel mirror. A 0.6 mm slit and a 1.0 mm pinhole were used as beam reductors. The detector was opened to 9.0 mm and operated in 1D mode. The measured diffractograms were analyzed in the Diffrac.Eva Software for an initial overview. Cu Kα_2 subtraction in the latter is carried out using the Rachinger recursion formula. Thereafter, a detailed line profile analysis (LPA) according to Birkholz[11,p.85–101] was carried out. A pseudo-Voigt (pV) function was used for the fitting of wurtzite (002) peaks. Cu Kα_1 and Kα_2 were separated. The peak position of the Kα_1 component was converted into the c lattice spacing of the measured unit cells. The Kα_1 component was further deconvoluted into its Cauchy and Gauss share. The Cauchy share of the peak broadening yielded the crystallite size (CS) of the grains in the measured film, while the microstrain (MS) was calculated from the Gauss share. The instrumental broadening was accounted for via the Si(400) peak obtained from the wafer substrate.
For RCs, the maximum of the combined Cu Kα_{1+2} of the symmetric θ-2θ scans was fixed as 2θ, and ω was rocked from 0°-2θ. The detector was opened to 9.0 mm and operated in 0D mode. The FWHMs of RCs were recorded as a measure of the angular distribution of crystallite tilts.
For PFs, the tube was used in point-focus and Bragg Brentano Geometry. A 2 mm pinhole was used as beam reductor. The detector was opened to 9.0 mm and operated

in 1D mode. The "thinned" mesh function of the software was used with a delta of 2°, giving 5000 measurement spots distributed on 40 ϕ circles equidistantly spaced on the 0-80° Ψ radius.
In-plane θ2-θ and 2θ scans (with the scattering vector Q close to parallel to the sample surface) yielded information on the crystal planes perpendicular to the sample surface, *i.e.* (xy0) planes. They were recorded with the beam in line-focus and parallelized by a primary Göbel mirror. The beam source was rotated by 90°, so that the line dimension of the beam was parallel to the film surface. This allowed a higher sample volume to be probed and thus improved signal intensity. The beam was diverted into the film and transmitted parallel to the film surface via Snellius angle α. The detector was opened to 9.0 mm and operated in 1D mode.
θ-2θ scans asymmetric to the sample surface (with varying Q orientation towards the latter) yielded information about crystal planes aslope to the sample surface, *i.e.* (xyz) planes. They were recorded with the beam in line-focus and parallelized by a primary Göbel mirror. The detector was opened to 9.0 mm and operated in 1D mode.
HT*is*XRD was carried out under Ar flow. Samples were heated in 50°C steps, equilibrated at the corresponding temperature and measured *in situ*. Height variations due to thermal expansion of the sample holder were corrected by a stage positioner. The X-ray beam was in line-focus and parallelized by a primary Göbel mirror.
Fundamental theory on XRD is given in [102,11,141,87,88,28,83].

8.3 SEM and TEM for images of the cross-sectional film structure

A Transmission Electron Microscope (TEM) JEM-2200FS (Jeol USA, Inc., Peabody MA, USA) and a Scanning Electron Microscope (SEM) Hitachi S-4800 (Hitachi Ltd., Inc., Tokyo, Japan) were used to image cross sections of Al-O-N thin films.
For TEM, films on Si(100) were manually broken, shaped into a wedge by mechanical tripod polishing, and finally ion milled to e^- transparency. The wedge was contacted to a Cu ring with an inner diameter of 2 mm and then imaged in regions of 20-30 nm thickness. Conventional bright field (BF) and dark field (DF) images, high resolution (HR) images and electron diffraction (ED) patterns were recorded.
For SEM, the thin films on Si(100) were manually broken, clamped into stainless steel holders and contacted with Ag paste in areas that were not scanned. Beam voltages of 1.0-5.0 kV were applied.

8.4 XPS for chemical states

Chemical states were assessed using X-Ray Photoelectron Spectroscopy (XPS). The binding energy (BE) and the full width at half maximum (FWHM) of the photoelectron

(photo e^-) lines Al *2p*, Si *2p*, O *1s* and N *1s* were investigated and are referred to as $BE_{Al2p/Si2p/O1s/N1s}$ and $FWHM_{Al2p/Si2p/O1s/N1s}$ for specified elements. The spectrometer used, a PHI Quantum 2000 Scanning ESCA Microprobe System (Physical Electronics Incorporated (PHI), Chanhassen MN, USA) was operated with monochromatic Al Kα radiation of 1486.6 eV and a beam diameter of 150.0 μm. The energy scale of the spectrometer was calibrated with gold (Au), copper (Cu) and silver (Ag) via photo e^- lines Cu $2p_{3/2}$, Ag $3d_{5/2}$ and Au $4f_{7/2}$ at 932.62, 368.21 and 83.96 eV, respectively, to within +/- 0.1 eV [ISO 15472; 2010-05]. The FWHM of Au $4f_{7/2}$ were found to be 0.72, 0.93 and 1.57 eV for pass energies of 5.85, 29.35 and 117.4 eV, respectively. The base pressure inside the measurement chamber remained below $8{\cdot}10^{-9}$ mbar.
Upon exposure to atmosphere, thin Al-(Si-)O-N films become covered with a native oxide of 3-10 nm thickness and potentially carbonaceous contaminations. These layers were removed directly prior to detailed XPS measurements with an Ar ion bombardment at 1 kV during 600 s. In order to avoid charge buildups, the insulating samples were flooded by Ar ions and e^- of low energy. Additionally, molybdenum (Mo) clamps with a small opening of only 1 mm were used for sample fixation, so that charges could dissipate off from the measurement spot. Since a potential charge buildup still has to be taken into account, a procedure[124] was applied to survey, and if necessary correct, peak shifts caused by charging. For this, the Mo clamps had been coated with Au prior to being used. During the sputter removal of oxide, small amounts of Au were redeposited onto the samples. This allowed Au $4f_{7/2}$ to be recorded and used for the calibration.
Survey spectra on the samples were taken before sputter removal of the native oxide as well as afterwards on each sample. They were recorded between 1345.00 and -5.00 eV at a pass energy of 117.40 eV and in 0.5 eV increments. Detailed spectra for the lines under investigation were measured immediately after native oxide removal. The pass energy for these was 29.35 eV and the increments were 0.125 eV.
The spectra were processed using the software CasaXPS version 2.3.17PR1.1 (Casa Software Ltd, Teignmouth, UK). Relative sensitivity factors were adopted from the the system manufaturer PHI. Shirley backgrounds were applied. All singlet peaks were highly symmetric and could be fitted with a single component that consisted of a combined Gaussian-Lorentzian curve (GL(Gaussian percentage)). GL(30) for Al *2p* and Si *2p*, GL(40) for O *1s* and GL(60) for N *1s* were found to give the best fit. Some Al-(Si-)O-N samples exhibited a separate, second peak for the N *1s* photo e^- line which was best fitted with GL(20). Au *4f* and Ar *2p* lines consisted of doublets, which were each fitted with two GL(30) components.
XPS also reveals the chemical compositions, but they contain an error of +/- 10%, which is less accurate than compositions obtained by RBS/ERDA. XPS stoichiometries were thus only considered for validation. Additionally, the O content was difficult to determine with XPS due to a rapid O recontamination after sputter removal of the native oxide. Firstly, films containing less O re-oxidize more strongly and more quickly than those containing more O. Secondly, O recontamination is dependent on the chamber conditions. Slight variations in *e.g.* the base pressure can have a significant influence on the O_2 content in the chamber. Calibrating XPS with RBS/ERDA was therefore

unreliable. As a result of this, and since RBS combined with ERDA provide the most reliable technique available for compositional analysis, only RBS/ERDA data were used to determine stoichiometries.

BEs of core e^- reflect the chemical oxidation state of an atom species. Every element is characterized by an atom number. It corresponds to the number of e^- associated with the atom, and the e^- are counterbalanced by protons in the nucleus. If an atom is oxidized, it lacks valence e^-, such that the remaining e^- are attracted more strongly by the protons. As a consequence, the BE of the core e^- rises. The reverse applies for reduced species. These contain additional valence e^-, so that the attracting force of the nucleus is spread over more negative charges and the BE of each core e^- thus sinks. FWHMs of core e^- lines are influenced by three phenomena: (1) disorder broadening, caused by local variation of the chemical environment of atoms of the same element; (2) two or more chemical states, the core e^- BEs of which are too similar to be resolved into single peaks; and (3) the lifetime of a core hole, which is again affected by the chemical state of an atom species and to which the FWHM is inversely proportional. Concerning (1), a threshold defined by factor of 1.15 in FWHM has been found to signify the onset of significant disorder broadening[121,72,24]. When FWHM of a photo e^- line is multiplied by the factor 1.15 or more relative to a reference material in which the same species has one chemical state, this implies that the atom experiences significant disorder due to a a variation in the surrounding coordination. This threshold has been applied for the interpretation of Al-(Si-)O-N data in this project.
Fundamental knowledge and reference data on XPS are given in[178,181,147,134,146].

8.5 Ellipsometry for optical properties

An important "measuring device" for a first estimate of the quality of transparent films is the human eye. Phenomena such as undesirable colorations, tarnishing or defects can be seen, and the most straightforward way to detect these is through visual cognition. The aim of this project was to create coatings as imperceptible and featureless as possible.
For a further assessment of the optical properties of the films, a spectroscopic ellipsometer (M-2000 VI (J.A. Woollam, Lincoln MN, USA)) was used to determine the refractive index n of the thin films. In addition, the analysis yielded parameters such as film thickness and surface roughness. The linearly polarized beam with wavelengths in the visible range was set to irradiate coatings on Si(100) wafers under three angles of 50°, 60° and 70° and was measured in reflection.

The spectral dependence of the amplitude ratio $tan(\Psi)$ and the phase shift Δ in the elliptically polarized beam was simulated with a Cauchy model to reproduce the measurement results. An example of this is shown in fig. 8.1 for an Al-O-N coating containing 34.6% O. The recorded data for Ψ and Δ varying with wavelength is plotted in color, and the simulated fit generated via Cauchy model is shown with a dotted black line. The parameters obtained from the latter were used to extract the variation of the refractive index n (blue double line) and the absorption coefficient k (green single line)

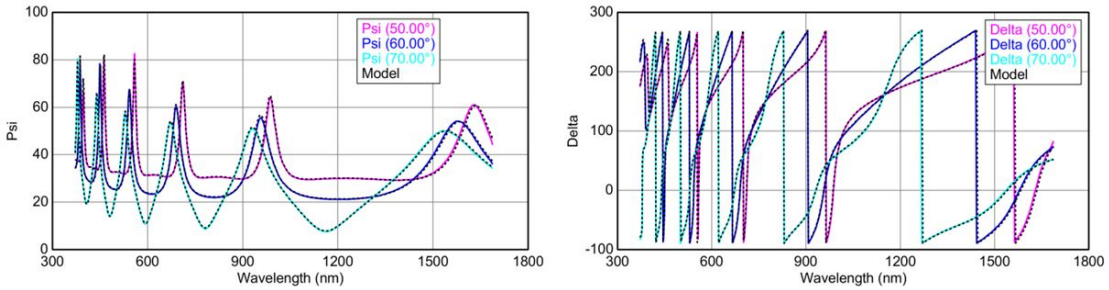

Figure 8.1: Ψ and Δ with varying wavelength recorded at three reflection angles of 50°, 60° and 70° shown as colored lines for a coating containing 34.6% O. The Cauchy simulation is plotted as black dotted line.

with wavelength, as shown in fig. 8.2.

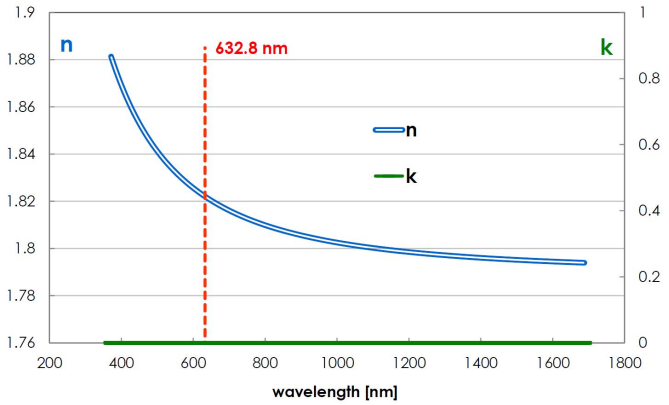

Figure 8.2: n (blue double line) and k (green single line) with varying wavelength as obtained from the Cauchy model. The red dotted line marks 632.8 nm.

The absorption band edge is at 300 nm. The value of n continuously decreases with increasing wavelength. k is optimized at 0 for the entire spectrum due to the transparency of the coating. The data analysis for this particular sample yielded a coating thickness of 755.8 nm and a surface roughness (Ra) of 3.0 nm. For comparison, a thickness of 759 nm was measured with contact profilometry. In general, good agreement between the film thicknesses measured with contact profilometry and those obtained from ellipsometry was observed, which corroborates the validity of ellipsometric data in this project.
For all Al-(Si-)O-N samples, n at the red wavelength 632.8 nm ($n_{632.8nm}$) was extracted. This wavelength corresponds to the emission line of a 85% helium and 15% neon gas laser and is often used as a reference (indicated with a red dotted line in fig. 8.2).

8.6 Nanoindentation for hardness and elasticity

A Nanoindenter Hysitron UbI 1 (Hysitron, Inc., Minneapolis MN, USA) equipped with a diamond Berkovich tip (SYNTON-MDP LTD, Port, Switzerland) was used to determine hardness (HD) and elasticity through Young's modulus (E) of the Al-(Si-)O-N coatings. Note that the general abbreviation for hardness in literature is "H"; H however is used for "hydrogen" in this project. The "Oliver and Pharr" method[118] was used to evaluate the results. Tip area calibrations on fused silica were regularly carried out in between measurement sequences of 10-15 samples. Indentation load forces were chosen so that the resulting indent depths did not exceed 10% of the coating thickness in order to avoid the "Indentation Size Effect" (ISE). 3 mN and/or 2 mN were found to be appropriate and were used in quadratic 3x3 indentation matrices in which the 9 single indents were spaced by 40 μm. Either both 2 and 3 mN matrices, or only the 2 mN matrix was used for evaluation depending on the thickness (800-1200 nm) and the HD of the coatings. Typical indentation depths were in the range of 60-100 nm. For samples on which the 3 mN matrix did not exceed the permissible indentation depth, no systematic difference between the 3 mN and the 2 mN matrix was found.

8.7 Profilometry and microscopy for residual stresses

To analyze the biaxial stress in Al-(Si-)O-N films, coatings were deposited onto extra thin substrates. Either round Si(100) wafers of 30 μm thickness and 5 mm diameter (University Wafer, South Boston VA, USA) or microscope cover glasses of 145 μm thickness and 30 mm diameter (Menzel-Gläser, Braunschweig, Germany) were used. These bend under the force of post-depositional residual film stress. Tensile stress imposes a bending of the substrate rim in the film direction and shapes it into a concave lens. Compressive stress, on the other hand, deforms the substrate convexly. The radius of curvature of the bent substrates was measured with a contact profilometer Bruker DektakXT (Bruker Germany, Karlsruhe, Germany) and an optical profilometer Leica DCM8 (Leica Microsystems (Schweiz) AG, Heerbrugg, Switzerland) and applied in the new Stoney equation[75] to yield the residual film stress. By definition, tensile stress is positive and compressive stress negative.

An optical microscope LEICA DFC420 (Leica Microsystems (Schweiz) AG, Heerbrugg, Switzerland) was used to image and magnify the appearance of the films and to follow the consequences of the post-depositional stress, such as for example crack formation. The optical microscope images were recorded on the commonly used thicker 350μm Si(100) substrates. Contrast and brightness of the images were adapted to emphasize features.

A Scanning Electron Microscope equipped with a Gallium Focused Ion Beam (GaFIB-SEM) FEI Helios NanoLab G3UC (FEI Company, Hillsboro OR, USA) was used to prepare and image cross sections through film cracks.

Extra thin substrates were needed for stress analysis for two reasons. Firstly, the thicker substrates are too rigid to show any systematic bending due to thin film stress. Instead, at a high enough stress level, the coating on them cracks as imaged with the optical microscope. Secondly, the curvature of a cracked film would yield a falsified stress result, since crack formation is concurrent with stress relief. Thin substrates are thus optimal for stress measurements as they bend without film cracking, while thick substrates are suitable to investigate the pattern of stress induced coating damage.

List of Abbreviations

α-Al_2O_3	α - aluminum oxide / sapphire
a-Al_2O_3	amorphous aluminum oxide
Ag	silver
Al	aluminum
Al-(Si-)(O-)N	aluminum (silicon) (oxy)nitride
AR coating	antireflective coating
Ar	argon
Au	gold
BE	binding energy
BF image	bright field image
C	carbon
CIG	Gas Ionization Chamber
CNC	Computerized Numerical Control
Cr	chromium
CS	crystallite size
Cu	copper
CVD	Chemical Vapor Deposition
DF image	dark field image
E	Young's modulus
e^-	electron
ED pattern	electron diffraction pattern
el.	elemental
ERDA	Elastic Recoil Detection Analysis
ETHZ	Swiss Federal Institute of Technology, Zürich
FWHM	full width at half maximum
G3 / G5	Gorilla glass of generation 3 / 5
GaFIB-SEM	Scanning Electron Microscope/y equipped with a Gallium Focused Ion Beam
GaN	gallium nitride
Ge	germanium
GL(%)	Gaussian-Lorentzian curve (Gaussian percentage)

H	hydrogen
HD	hardness
He-ERD	Helium Elastic Recoil Detection
HiPIMS	High Power Impulse Magnetron Sputtering
HR image	high resolution image
HT*is*XRD	high temperature *in situ* X-Ray Diffraction
ISE	Indentation Size Effect
k	absorption coefficient
K	potassium
LIP	Laboratory of Ion Beam Physics
LPA	line profile analysis
Mo	molybdenum
MOSS	Multibeam Optical Stress Sensor
MS	microstrain
N	nitrogen
n	refractive index
Na	sodium
O	oxygen
O(N)	an O in an N lattice position
PAS	Positron Annihilation Spectroscopy
PALS	Positron Annihilation Lifetime Spectroscopy
PC	polycarbonate
PEEK	polyether ether ketone
PF	pole figure
photo e^-	photoelectron
PTFE	polytetrafluoroethylene
PVD	Physical Vapor Deposition
Q	scattering vector
RBS	Rutherford Backscattering Spectrometry
RC	rocking curve
R-UCFDC-MS	Reactive Unbalanced Closed Field Direct Current Magnetron Sputtering

SEM	Scanning Electron Microscope/y
Si	silicon
Si(Al)	a Si in an Al lattice position
Sn	tin
SZM	Structure Zone Model
T	temperature
Ta	tantalum
TEM	Transmission Electron Microscope/y
TiN	titanium nitride
ToF	Time-of-Flight
V(Al)	a vacancy in an Al lattice position
W	tungsten
XRD	X-Ray Diffraction
1/2/3D	one/two/tree dimensional
χ	Pauling electronegativity
σ	residual stress

Bibliography

[1] G. Abadias, A. Michel, C. Tromas, C. Jaouen, and S. N. Dub. Stress, interfacial effects and mechanical properties of nanoscale multilayered coatings. *Surface & Coatings Technology*, 202(4-7):844–853, 2007. doi: 10.1016/j.surfcoat.2007.05.068.

[2] G. Abadias, E. Chason, J. Keckes, M. Sebastiani, G. B. Thompson, E. Barthel, G. L. Doll, C. E. Murray, C. H. Stoessel, and L. Martinu. Review Article: Stress in thin films and coatings: Current status, challenges, and prospects. *Journal of Vacuum Science & Technology A*, 36(2):020801, 2018. doi: 10.1116/1.5011790.

[3] J. Affinito and R. R. Parsons. Mechanisms of voltage controlled, reactive, planar magnetron sputtering of Al in Ar/N_2 and Ar/O_2 atmospheres. *Journal of Vacuum Science and Technology A*, 2(3):1275–1284, 1984. doi: 10.1116/1.572395.

[4] A. Anders. A structure zone diagram including plasma-based deposition and ion etching. *Thin Solid Films*, 518(15):4087–4090, 2010. doi: 10.1016/j.tsf.2009.10.145.

[5] H. Baránková, S. Berg, P. Carlsson, and C. Nender. Hysteresis effects in the sputtering process using two reactive gases. *Thin Solid Films*, 260(2):181–186, 1995. doi: 10.1016/0040-6090(94)06501-2.

[6] P. B. Barna and M. Adamik. Fundamental structure forming phenomena of polycrystalline films and the structure zone models. *Thin Solid Films*, 317:27–33, 1998. doi: 10.1016/S0040-6090(97)00503-8.

[7] W. Barthlott and C. Neinhuis. Purity of the sacred lotus, or escape from contamination in biological surfaces. *Planta*, 202:1–8, 1997.

[8] U. Beck, D. T. Smith, G. Reiners, and S. J. Dapkunas. Mechanical properties of SiO_2 and Si_3N_4 coatings: A BAM/NIST co-operative project. *Thin Solid Films*, 332(1-2):164–171, 1998. doi: 10.1016/S0040-6090(98)00989-4.

[9] S. Berg and T. Nyberg. Fundamental understanding and modeling of reactive sputtering processes. *Thin Solid Films*, 476(2):215–230, 2005. doi: 10.1016/j.tsf.2004.10.051.

[10] J. L. Beuth. Cracking of thin bonded films in residual tension. *International Journal of Solids and Structures*, 29(13):1657–1675, 1992. doi: 10.1016/0020-7683(92)90015-L.

[11] M. Birkholz. *Thin Film Analysis by X-ray Scattering*. WILEY-VCH Verlag GmbH & Co. KGaA, Weinheim, Germany, 2006. ISBN 3-527-31052-5. doi: 10.1002/3527607595.

[12] W. L. Bond and W. Kaiser. Interstitial versus substitutional oxygen in silicon. *Journal of Physics and Chemistry of Solids*, 16(1-2):44–45, 1960. doi: 10.1016/0022-3697(60)90069-X.

[13] J. Borges, F. Vaz, and L. Marques. AlN_xO_y thin films deposited by DC reactive magnetron sputtering. *Applied Surface Science*, 257(5):1478–1483, 2010. doi: 10.1016/j.apsusc.2010.08.076.

[14] J. Borges, E. Alves, F. Vaz, and L. Marques. Optical properties of AlN_xO_y thin films deposited by DC magnetron sputtering. *Proceedings of SPIE*, 8001: 80010F–1–8, 2011. doi: 10.1117/12.892038.

[15] J. Borges, N. Martin, N. P. Barradas, E. Alves, D. Eyidi, M. F. Beaufort, J. P. Riviere, F. Vaz, and L. Marques. Electrical properties of AlN_xO_y thin films prepared by reactive magnetron sputtering. *Thin Solid Films*, 520(21): 6709–6717, 2012. doi: 10.1016/j.tsf.2012.06.062.

[16] J. Borges, R. M.S. Pereira, M. S. Rodrigues, T. Kubart, S. Kumar, K. Leifer, A. Cavaleiro, T. Polcar, M. I. Vasilevskiy, and F. Vaz. Broadband Optical Absorption Caused by the Plasmonic Response of Coalesced Au Nanoparticles Embedded in a TiO_2 Matrix. *Journal of Physical Chemistry C*, 120(30): 16931–16945, 2016. doi: 10.1021/acs.jpcc.6b03684.

[17] K. R. Bray, R. L C Wu, S. Fries-Carr, and J. Weimer. Aluminum oxynitride dielectrics for multilayer capacitors with higher energy density and wide temperature properties. *Thin Solid Films*, 518(1):366–371, 2009. doi: 10.1016/j.tsf.2009.06.052.

[18] D. G. Cahill, S.-M. Lee, and T. I. Selinder. Thermal conductivity of κ-Al_2O_3 and α-Al_2O_3 wear-resistant coatings. *Journal of Applied Physics*, 83 (11):5783–5786, 1998. doi: 10.1063/1.367500.

[19] B. Chapman. *Glow Discharge Processes*. John Wiley & Sons, New Jersey, USA, 1980. ISBN 047107828X. doi: QC702.7.P6C48.

[20] M. W. Chase, Jr. *NIST-JANAF Thermochemical Tables*. ACS, AIP, New York, 4th edition, 1998. doi: citeulike-article-id:12140840.

[21] E. Chason, B. W. Sheldon, L. B. Freund, J. A. Floro, and S. J. Hearne. Origin of Compressive Residual Stress in Polycrystalline Thin Films. *Physical Review Letters*, 88(15):4, 2002. doi: 10.1103/PhysRevLett.88.156103.

[22] J. Cheng, D. Agrawal, and R. Roy. Microwave synthesis of aluminum oxynitride (ALON). *Journal of Materials Science Letters*, 18(24):1989–1990, 1999. doi: 10.1023/A:1006681732457.

[23] A. Chorfa, M. A. Madjoubi, M. Hamidouche, N. Bouras, J. Rubio, and F. Rubio. Glass hardness and elastic modulus determination by nanoindentation using displacement and energy methods. *Ceramics - Silikaty*, 54(3): 225–234, 2010.

[24] R. J. Cole, N. J. Brooks, and P. Weightman. Madelung Potentials and Disorder Broadening of Core Photoemission Spectra in Random Alloys. *Physical Review Letters*, 78(19):3777–3780, 1997. doi: 10.1103/PhysRevLett.78.3777.

[25] Corning. Gorilla glass product information sheet, 2017. URL http://www.corning.com/content/dam/corning/microsites/csm/gorillaglass/PI_Sheets/Corning_Gorilla_Glass_5_PI_Sheet_RevB.pdf.

[26] Corning. Gorilla glass 5, visited 03.04.2019. URL http://www.corning.com/gorillaglass/worldwide/en/glass-types/gorilla-glass-5.html.

[27] B. D. Darwent. Bond Dissociation Energies in Simple Molecules. *United States Department of Commerce, National Bureau of Standards*, (31):1–58, 1970. doi: 10.6028/NBS.NSRDS.31.

[28] R. Delhez, Th. H. de Keijser, E. J. Mittemeijer, and J. I. Langford. Size and strain parameters for peak profiles: Sense and nonsense. *Australian Journal of Physics*, 41:213–227, 1988. doi: 10.1071/PH880213.

[29] H. Demiryont, L. R. Thompson, and G. J. Collins. Optical properties of aluminum oxynitrides deposited by laser-assisted CVD. *Applied Optics*, 25: 1311, 1986. doi: 10.1364/AO.25.001311.

[30] D. Depla, X. Y. Li, S. Mahieu, and R. De Gryse. Determination of the effective electron emission yields of compound materials. *Journal of Physics D: Applied Physics*, 41(20):202003, 2008. doi: 10.1088/0022-3727/41/20/202003.

[31] D. Depla, S. Mahieu, and R. De Gryse. Magnetron sputter deposition: Linking discharge voltage with target properties. *Thin Solid Films*, 517(9):2825–2839, 2009. doi: 10.1016/j.tsf.2008.11.108.

[32] Diederik Depla, Stijn Mahieu, and R. De Gryse. *Reactive Sputter Deposition*, volume 109 of *Springer Series in Materials Science*. SpringerVerlag GmbH, Heidelberg, Germany, 2008. ISBN 978-3-540-76662-9. doi: 10.1007/978-3-540-76664-3.

[33] M. J. Dodge. Refractive properties of magnesium fluoride. *Applied Optics*, 23(12):1980–1985, 1984. doi: 10.1364/ao.23.001980.

[34] K. Domen and T. J. Chuang. Laser induced photodissociation and desorption. I. CH_2I_2 adsorbed on Al_2O_3. *The Journal of Chemical Physics*, 90(6): 3318–3331, 1989. doi: 10.1063/1.455886.

[35] L. R. Doolittle. A Semiautomatic Algortihm for Rutherford Backscattering Analysis. *Nuclear Instruments and Methods in Physics Research B*, 15:227–231, 1986. doi: 0168-583X/86.

[36] J. Dundurs. Effect of Elastic Constants on Stress in a Composite Under Plane Deformation. *Journal of Composite Materials*, 1(3):310–322, 1967. doi: 10.1177/002199836700100306.

[37] J. Dundurs. Discussion: Edge-Bonded Dissimilar Orthogonal Elastic Wedges Under Normal and Shear Loading. *Journal of Applied Mechanics*, 36(3):650–652, 1969. doi: 10.1115/1.3564739.

[38] C. Duquenne, P. Y. Tessier, M. P. Besland, B. Angleraud, P. Y. Jouan, R. Aubry, S. Delage, and M. A. Djouadi. Impact of magnetron configuration on plasma and film properties of sputtered aluminum nitride thin films. *Journal of Applied Physics*, 104(6):063301, 2008. doi: 10.1063/1.2978226.

[39] F. Dwikusuma and T. F. Kuech. X-ray photoelectron spectroscopic study on sapphire nitridation for GaN growth by hydride vapor phase epitaxy: Nitridation mechanism. *Journal of Applied Physics*, 94(9):5656–5664, 2003. doi: 10.1063/1.1618357.

[40] D. J. Eaglesham, A. E. White, L. C. Feldman, N. Moriya, and D. C. Jacobson. Equilibrium Shape of Si. *Physical Review Letters*, 70(11):1643–1646, 1993. doi: 10.1103/PhysRevLett.70.1643.

[41] G. Este and W. D. Westwood. Reactive deposition of low loss Al_2O_3 optical waveguides by modified dc planar magnetron sputtering. *Journal of Vacuum Science & Technology A*, 2(3):1238, 1984. doi: 10.1116/1.572502.

[42] T. H. Fang and W. J. Chang. Nanoindentation characteristics on polycarbonate polymer film. *Microelectronics Journal*, 35(7):595–599, 2004. doi: 10.1016/j.mejo.2004.02.004.

[43] E. Figueiredo, R. J. C. Silva, M. F. Araújo, and J. C. Senna-Martinez. Identification of ancient gilding technology and Late Bronze Age metallurgy by EDXRF, Micro-EDXRF, SEM-EDS and metallographic techniques. *Microchimica Acta*, 168(3):283–291, 2010. doi: 10.1007/s00604-009-0284-6.

[44] M. Fischer, M. Trant, K. Thorwarth, J. Patscheider, and H. J. Hug. A setup for arc-free reactive DC sputter deposition of Al-O-N. *Surface & Coatings Technology*, 362:220–224, 2019. doi: 10.1016/j.surfcoat.2019.01.082.

[45] C. Freysoldt, B. Grabowski, T. Hickel, J. Neugebauer, G. Kresse, A. Janotti, and C. G. Van De Walle. First-principles calculations for point defects in solids. *Reviews of Modern Physics*, 86(1):253–305, 2014. doi: 10.1103/RevModPhys.86.253.

[46] B. D. Gesner and P. G. Kelleher. Oxidation of bisphenol a polymers. *Journal of Applied Polymer Science*, 13(10):2183–2191, 1969. doi: 10.1002/app.1969.070131013.

[47] A. Gevaudan and J. Andrieu. Contact drying modelling of agitated porous alumina beads. *Chemical Engineering and Processing*, 30(1):31–37, 1991. doi: 10.1016/0255-2701(91)80006-B.

[48] S. N. Ghosh, I. O. Parm, S. K. Dhungel, K. S. Jang, S. W. Jeong, J. Yoo, S. H. Hwang, and J. Yi. Field-induced surface passivation of p-type silicon by using AlON films. *Renewable Energy*, 33(2):320–325, 2008. doi: 10.1016/j.renene.2007.05.030.

[49] V. G. Gilev. IR Spectra and Structure of Si-Al-O-N Phases Prepared by Carbothermal Reduction of Kaolin in Nitriding Atmosphere. *Inorganic Materials*, 37(10):1041–1045, 2001. doi: 10.1023/A:1012383211463.

[50] G. H. Gilmer and A. F. Bakker. Molecular dynamics simulations of steps at crystal surfaces. *Materials Research Society Symposium - Proceedings*, 209:135–145, 1991. doi: 10.1017/CBO9781107415324.004.

[51] Gorilla glass users. Reported Gorilla glass failures, visited 03.04.2019. URL https://www.reddit.com/r/explainlikeimfive/comments/37kx8v/eli5_why_does_gorilla_glass_shatter_so_easily/.

[52] H. Gleiter. Nanostructured materials: basic concepts and microstructure. *Acta Materialia*, 48(1):1–29, 2000. doi: 10.1016/S1359-6454(99)00285-2.

[53] S. Goedecker, M. Teter, and J. Hutter. Separable dual-space Gaussian pseudopotentials. *Physical Review B*, 54(3):1703–1710, 1996.

[54] S. Grainger and J. Blunt. *Engineering Coatings - Design and Application.* Abington Publishing, Abington, England, 2nd edition, 1989. ISBN 9781845698577.

[55] J. E. Greene. Review Article: Tracing the recorded history of thin-film sputter deposition: From the 1800s to 2017. *Journal of Vacuum Science & Technology A*, 35(5):05C204, 2017. doi: 10.1116/1.4998940.

[56] S. Gsell, T. Bauer, J. Goldfuss, M. Schreck, and B. Stritzker. A route to diamond wafers by epitaxial deposition on silicon via iridium/yttria-stabilized zirconia buffer layers. *Applied Physics Letters*, 84(22):4541, 2004. doi: 10.1063/1.1758780.

[57] M. Hagen and M. Finnis. Point defects and chemical potentials in ordered alloys. *Philosophical Magazine A: Physics of Condensed Matter, Structure, Defects and Mechanical Properties*, 77(2):447–464, 1998. doi: 10.1080/01418619808223764.

[58] F. Hanic, M. Hartmanová, G. G. Knab, A. A. Urusovskaya, and K. S. Bagdasarov. Real structure of undoped Y_2O_3 single crystals. *Acta Crystallographica Section B*, 40(2):76–82, 1984. doi: 10.1107/S0108768184001774.

[59] J. H. Harris, R. A. Youngman, and R. G. Teller. On the nature of the oxygen-related defect in aluminum nitride. *Journal of Materials Research*, 5 (08):1763–1773, 1990. doi: 10.1557/JMR.1990.1763.

[60] T.M Hartnett, S.D Bernstein, E.A Maguire, and R.W Tustison. Optical properties of ALON (aluminum oxynitride). *Infrared Physics & Technology*, 39(4):203–211, 1998. doi: 10.1016/S1350-4495(98)00007-3.

[61] R. Hauert, J. Patscheider, M. Tobler, and R. Zehringer. XPS investigation of the a-C:H/Al interface. *Surface Science*, 292(1-2):121–129, 1993. doi: 10.1016/0039-6028(93)90395-Z.

[62] M. K. Hedayati and M. Elbahri. Antireflective coatings: Conventional stacking layers and ultrathin plasmonic metasurfaces, a mini-review. *Materials*, 9 (6), 2016. doi: 10.3390/ma9060497.

[63] A. Hieke, V. Lieberman, and G. J. van der Kolk. *Hard Coatings and Coating Processes for the Automotive Industry*, pages 133–148. Springer International Publishing, New York, USA, 2015. ISBN 978-3-319-14771-0. doi: 10.1007/978-3-319-14771-0_7.

[64] K. Hirohata, Y. Nishi, N. Tsukamoto, N. Oka, Y. Sato, I. Yamamoto, and Y. Shigesato. Al-doped ZnO (AZO) films deposited by reactive sputtering with unipolar-pulsing and plasma-emission control systems. *Thin Solid Films*, 518(11):2980–2983, 2010. doi: 10.1016/j.tsf.2009.09.177.

[65] P. Hohenberg and W. Kohn. Inhomogeneous electron gas. *Physical Review*, 136(3B):B864–B871, 1964. doi: 10.1103/PhysRev.136.B864.

[66] H. Holleck. Material selection for hard coatings. *Journal of Vacuum Science & Technology A*, 4(6):2661–2669, 1986. doi: 10.1116/1.573700.

[67] M. A. Hopcroft, W. D. Nix, and T. W. Kenny. What is the Young's Modulus of Silicon? *Journal of Microelectromechanical Systems*, 19(2):229–238, 2010. doi: 10.1109/JMEMS.2009.2039697.

[68] J. W. Hutchinson and Z. Suo. Mixed Mode Cracking in Layered Materials. *Advances in Applied Mechanics*, 29:63–191, 1992. doi: 10.1016/S0065-2156(08)70164-9.

[69] J. Hutter, M. Iannuzzi, F. Schiffmann, and J. Vandevondele. Cp2k: Atomistic simulations of condensed matter systems. *Wiley Interdisciplinary Reviews: Computational Molecular Science*, 4(1):15–25, 2014. doi: 10.1002/wcms.1159. URL `http://www.cp2k.org/`.

[70] C. K. Hwangbo, L. J. Lingg, J. P. Lehan, H. A. Macleod, and F. Suits. Reactive ion assisted deposition of aluminum oxynitride thin films. *Applied Optics*, 28(14):2779–84, 1989. doi: 10.1364/AO.28.002779.

[71] N. J. Ianno, H. Enshashy, and R. O. Dillon. Aluminum oxynitride coatings for oxidation resistance of epoxy films. *Surface & Coatings Technology*, 155 (2-3):130–135, 2002. doi: 10.1016/S0257-8972(02)00051-8.

[72] D. A. Jaeger. *Interface Investigations on Titanium Nitride Bilayer Systems.* PhD thesis, École Polytechnique Fédérale de Lausanne, 2012.

[73] K. Jang, S. Jung, J. Lee, K. Lee, J. Kim, H. Son, and J. Yi. Optical and electrical properties of negatively charged aluminium oxynitride films. *Thin Solid Films*, 517(1):444–446, 2008. doi: 10.1016/j.tsf.2008.08.138.

[74] G. C. A. M. Janssen. Stress and strain in polycrystalline thin films. *Thin Solid Films*, 515(17):6654–6664, 2007. doi: 10.1016/j.tsf.2007.03.007.

[75] G. C. A. M. Janssen, M. M. Abdalla, F. van Keulen, B. R. Pujada, and B. van Venrooy. Celebrating the 100th anniversary of the Stoney equation for film stress: Developments from polycrystalline steel strips to single crystal silicon wafers. *Thin Solid Films*, 517(6):1858–1867, 2009. doi: 10.1016/j.tsf.2008.07.014.

[76] C. Jeynes, N.P. Barradas, P.K. Marriott, G. Boudreault, M. Jenkin, E. Wendler, and R. P. Webb. Elemental Thin Film Depth Profiles by Ion Beam Analysis Using Simulated Annealing - a New Tool. *Journal of Physics D: Applied Physics1*, 36(7):R97–R126, 2003.

[77] K. Johansson and E. Lewin. Influence of oxygen content on structure and material properties of reactively sputtered Al-Ge-O-N thin films. *Journal of*

Alloys and Compounds, 738:515–527, 2018. doi: 10.1016/j.surfcoat.2010.02.029.

[78] Y. W. Kim, H. C. Park, Y. B. Lee, K. D. Oh, and R. Stevens. Reaction sintering and microstructural development in the system Al_2O_3-AlN. *Journal of the European Ceramic Society*, 21(13):2383–2391, 2001. doi: 10.1016/S0955-2219(01)00200-X.

[79] R. Koch. Stress in Evaporated and Sputtered Thin Films - A Comparison. *Surface & Coatings Technology*, 204(12-13):1973–1982, 2010. doi: 10.1016/j.surfcoat.2009.09.047.

[80] J. Kohout, E. Bousser, T. Schmitt, R. Vernhes, O. Zabeida, J. Klemberg-Sapieha, and L. Martinu. Stable reactive deposition of amorphous Al_2O_3 films with low residual stress and enhanced toughness using pulsed dc magnetron sputtering with very low duty cycle. *Vacuum*, 124:96–100, 2016. doi: 10.1016/j.vacuum.2015.11.017.

[81] J. Kohout, J. Qian, T. Schmitt, R. Vernhes, O. Zabeida, J. Klemberg-Sapieha, and L. Martinu. Hard AlN films prepared by low duty cycle magnetron sputtering and by other deposition techniques. *Journal of Vacuum Science & Technology A*, 35:061505 1–9, 2017. doi: 10.1116/1.4999460.

[82] C. Kottler, M. Döbeli, F. Glaus, and M. Suter. A spectrometer for low energy heavy ion ERDA. *Nuclear Instruments and Methods in Physics Research B: Beam Interactions with Materials and Atoms*, 248(1):155–162, 2006. doi: 10.1016/j.nimb.2006.02.013.

[83] C. E. Krill and R. Birringer. Estimating grain-size distributions in nanocrystalline materials from X-ray diffraction profile analysis. *Philosophical Magazine A: Physics of Condensed Matter, Structure, Defects and Mechanical Properties*, 77(3):621–640, 1998. doi: 10.1080/01418619808224072.

[84] S. Krishnan, J. K. R. Weber, R. A. Schiffman, P. C. Nordine, and R. A. Reed. Refractive Index of Liquid Aluminum Oxide at 0.6328 μm. *Journal of the American Ceramic Society*, 74:881–883, 1991. doi: 10.1111/j.1151-2916.1991.tb06947.x.

[85] T. Krug and R. Tietema. *Decorative PVD Coatings on Automotive Plastic*, pages 215–230. Springer International Publishing, New York, USA, 2015. ISBN 978-3-319-14771-0. doi: 10.1007/978-3-319-14771-0_13.

[86] T. Laino and J. Hutter. Notes on "Ewald summation of electrostatic multipole interactions up to quadrupolar level" [J. Chem. Phys. 119, 7471 (2003)]. *Journal of Chemical Physics*, 129(7):074102, 2008. doi: 10.1063/1.2970887.

[87] J. I. Langford and A. J. C. Wilson. Scherrer after Sixty Years: A Survey and Some New Results in the Determination of Crystallite Size. *Journal of Applied Crystallography*, 11(2):102–113, 1978. doi: 10.1107/S0021889878012844.

[88] J. I. Langford, D. Louër, and P. Scardi. Effect of a crystallite size distribution on X-ray diffraction line profiles and whole-powder-pattern fitting. *Journal of Applied Crystallography*, 33:964–974, 2000. doi: 10.1107/S002188980000460X.

[89] A. M. Lejus. Sur la formation à haute température de spinelles non stoechiométriques et de phases derivées. *Revue internationale des hautes températures et des réfractaires*, t1:53–95, 1964.

[90] W. P. Leroy, S. Mahieu, R. Persoons, and D. Depla. Method to Determine the Sticking Coefficient of O_2 on Deposited Al During Reactive Magnetron Sputtering, Using Mass Spectrometry. *Plasma Processes and Polymers*, 6, 2009. doi: 10.1002/ppap.200932401.

[91] Y. Leterrier, L. Médico, F. Demarco, J. A. E. Månson, U. Betz, M. F. Escolà, M. Kharrazi Olsson, and F. Atamny. Mechanical integrity of transparent conductive oxide films for flexible polymer-based displays. *Thin Solid Films*, 460:156–166, 2004. doi: 10.1016/j.tsf.2004.01.052.

[92] E. Lewin and J. Patscheider. Structure and properties of sputter-deposited Al-Sn-N thin films. *Journal of Alloys and Compounds*, 682:42–51, 2016. doi: 10.1016/j.jallcom.2016.04.278.

[93] E. Lewin, M. Parlinska-Wojtan, and J. Patscheider. Nanocomposite Al–Ge–N thin films and their mechanical and optical properties. *Journal of Materials Chemistry*, 22(33):16761, 2012. doi: 10.1039/c2jm32815a.

[94] A. Leyland and A. Matthews. Design criteria for wear-resistant nanostructured and glassy-metal coatings. *Surface & Coatings Technology*, 177-178: 317–324, 2004. doi: 10.1016/j.surfcoat.2003.09.011.

[95] Y. Li, C. M. Lousada, and P. A. Korzhavyi. The nature of hydrogen in γ-alumina. *Journal of Applied Physics*, 115:203514, 2014. doi: 10.1063/1.4879897.

[96] H. M. Liao, R. N. S. Sodhi, and T. W. Coyle. Surface composition of AlN powders studied by x-ray photoelectron spectroscopy and bremsstrahlung-excited Auger electron spectroscopy. *Journal of Vacuum Science & Technology A*, 11(5):2681–2686, 1993. doi: 10.1116/1.578626.

[97] D. Lundin. *The HiPIMS Process*. PhD thesis, Linköping University, Sweden, 2010.

[98] D. Lundin and K. Sarakinos. An introduction to thin film processing using high-power impulse magnetron sputtering. *Journal of Materials Research*, 27(05):780–792, 2012. doi: 10.1557/jmr.2012.8.

[99] Y.-R. Luo. *Comprehensive Handbook of Chemical Bond Energies*. CRC Press, Boca Raton, Fl, USA, 2007. doi: 10.1201/9781420007282.

[100] S. Maniv, C. Miner, and W. D. Westwood. High rate deposition of transparent conducting films by modified reactive planar magnetron sputtering of Cd_2Sn alloy. *Journal of Vacuum Science & Technology*, 18(2):195, 1981. doi: 10.1116/1.570722.

[101] H. Mao and M. Selleby. Thermodynamic reassessment of the Si_3N_4-AlN-Al_2O_3-SiO_2 system - Modeling of the SiAlON and liquid phases. *Calphad: Computer Coupling of Phase Diagrams and Thermochemistry*, 31(2):269–280, 2007. doi: 10.1016/j.calphad.2006.11.002.

[102] W. Massa. *Kristallstrukturbestimmung*. Vieweg + Teubner Verlag, Leibzig, Germany, 7th edition, 2011. ISBN 978-3-8348-1726-6.

[103] J. Matsuoka, N. Kitamura, S. Fujinaga, T. Kitaoka, and H. Yamashita. Temperature dependence of refractive index of SiO_2 glass. *Journal of Non-Crystalline Solids*, 135(1):86–89, 1991. doi: 10.1016/0022-3093(91)90447-E.

[104] J. W. McCauley, P. Patel, M. Chen, G. Gilde, E. Strassburger, B. Paliwal, K. T. Ramesh, and D. P. Dandekar. AlON: A brief history of its emergence and evolution. *Journal of the European Ceramic Society*, 29(2):223–236, 2009. doi: 10.1016/j.jeurceramsoc.2008.03.046.

[105] F. Medjani, R. Sanjinés, G. Allidi, and A. Karimi. Effect of substrate temperature and bias voltage on the crystallite orientation in RF magnetron sputtered AlN thin films. *Thin Solid Films*, 515(1):260–265, 2006. doi: 10.1016/j.tsf.2005.12.145.

[106] J. P. Mercier, J. J. Aklonis, M. Litt, and A. V. Tobolsky. Viscoelastic behavior of the polycarbonate of bisphenol A. *Journal of Applied Polymer Science*, 9(2):447–459, 1965. doi: 10.1002/app.1965.070090206.

[107] B. P. Mikhailov, I. A. Rudnev, A. R. Kadyrbaev, A. B. Mikhailova, and P. V. Bobin. Effect of refractory nitride nanoadditives on the properties of $(Bi,Pb)_2Sr_2Ca_2Cu_3O_{10+\delta}$. *Inorganic Materials*, 43(3):268–276, 2007. doi: 10.1134/S0020168507030119.

[108] I. Montero, L. Galán, E. De la Cal, and J. M. Albella. Incorporation of -OH Radicals in Anodic Silicon Oxide Films Studied by Secondary-Ion Mass Spectroscopy, X-Ray Photoelectron Spectroscopy and IR Analysis. *Thin Solid Films*, 193/194:325–332, 1990. doi: 10.1002/clc.4960111015.

[109] V. Mortet, M. Nesladek, K. Haenen, A. Morel, M. D'Olieslaeger, and M. Vanecek. Physical properties of polycrystalline aluminium nitride films deposited by magnetron sputtering. *Diamond and Related Materials*, 13: 1120–1124, 2004. doi: 10.1016/j.diamond.2003.10.082.

[110] S. Mráz and J. M. Schneider. Energy distribution of O^- ions during reactive magnetron sputtering. *Applied Physics Letters*, 89(5):051502, 2006. doi: 10.1063/1.2266888.

[111] J. Musil and J. Vlček. Magnetron sputtering of hard nanocomposite coatings and their properties. *Surface & Coatings Technology*, 142-144:557–566, 2001. doi: 10.1016/S0257-8972(01)01139-2.

[112] M. A. Nastasi, J. W. Mayer, and Y. Wang. *Ion Beam Analysis: Fundamentals and Applications*. CRC Press by Taylor & Francis Group, Boca Raton, USA, 1st edition, 2014. ISBN 978-1-4398-4638-4.

[113] P. Neogi and G. Zahedi. Environmental stress cracking of glassy polymers. *Industrial and Engineering Chemistry Research*, 53(2):672–677, 2014. doi: 10.1021/ie403201a.

[114] E. D. Nicholson. The Ancient Craft of Gold Beating. *Gold Bulletin*, 12: 161–166, 1979. doi: 10.1007/BF03215119.

[115] R. S. Nowicki. Properties of rf-sputtered Al_2O_3 films deposited by planar magnetron. *Journal of Vacuum Science & Technology*, 14:127–133, 1977. doi: 10.1116/1.569103.

[116] M. E. O'Hern, R. H. Parrish, and W. C. Oliver. Evaluation of mechanical properties of TiN films by ultralow load indentation. *Thin Solid Films*, 181: 357–363, 1989. doi: 10.1016/0040-6090(89)90504-X.

[117] M. Ohring. *Materials Science of Thin Films: Deposition and Structure*. Academic Press, San Diego, USA, 1st edition, 2001.

[118] W. C. Oliver and G. M. Pharr. An improved technique for determining hardness and elastic modulus using load and displacement sensing indentation experiments. *Journal of Materials Research*, 7(6):1564–1583, 1992. doi: 10.1557/JMR.1992.1564.

[119] J. Patscheider, T. Zehnder, and M. Diserens. Structure-performance relations in nanocomposite coatings. *Surface & Coatings Technology*, 146: 201–208, 2001. doi: 10.1016/S0257-8972(01)01389-5.

[120] L. Pekker. Plasma chemistry model of DC magnetron reactive sputtering in Ar-O_2 gas mixtures. *Thin Solid Films*, 312(1-2):341–347, 1998. doi: 10.1016/S0040-6090(97)00716-5.

[121] A. Pélisson. *Al-Si-N Transparent Hard Nanostructured Coatings*. PhD thesis, University of Basel, Switzerland, 2009.

[122] A. Pélisson, M. Parlinska-Wojtan, H. J. Hug, and J. Patscheider. Microstructure and mechanical properties of Al–Si–N transparent hard coatings deposited by magnetron sputtering. *Surface & Coatings Technology*, 202(4-7): 884–889, 2007. doi: 10.1016/j.surfcoat.2007.05.094.

[123] A. Pélisson-Schecker, H. J. Hug, and J. Patscheider. Complex phase compositions in nanostructured coatings as evidenced by photoelectron spectroscopy: The case of Al–Si–N hard coatings. *Journal of Applied Physics*, 108(2):23508, 2010. doi: 10.1063/1.3460099.

[124] A. Pélisson-Schecker, H. J. Hug, and J. Patscheider. Charge referencing issues in XPS of insulators as evidenced in the case of Al-Si-N thin films. *Surface & Interface Analysis*, 44(1):29–36, 2012. doi: 10.1002/sia.3765.

[125] A. Pélisson-Schecker, H. J. Hug, and J. Patscheider. Morphology, microstructure evolution and optical properties of Al-Si-N nanocomposite coatings. *Surface & Coatings Technology*, 257:114–120, 2014. doi: 10.1016/j.surfcoat.2014.08.053.

[126] J. P. Perdew, K. Burke, and M. Ernzerhof. Generalized Gradient Approximation Made Simple. *Physical Review Letters*, 77(18):3865–3868, 1996. doi: 10.1103/PhysRevLett.77.3865.

[127] I. Petrov, F. Adibi, J. E. Greene, W. D. Sproul, and W. D. Munz. Use of an externally applied axial magnetic-field to control ion neutral flux ratios incident at the substrate during magnetron sputter deposition. *Journal of Vacuum Science & Technology a-Vacuum Surfaces and Films*, 10(5):3283–3287, 1992. doi: 10.1116/1.577812.

[128] I. Petrov, P. B. Barna, L. Hultman, and J. E. Greene. Microstructural evolution during film growth. *Journal of Vacuum Science & Technology A*, 21(5):S117–S128, 2003. doi: 10.1116/1.1601610.

[129] C. A. Pignedoli, D. Passerone, H. J. Hug, A. Pélisson-Schecker, and J. Patscheider. Role of negatively charged defects in the lattice contraction of Al-Si-N. *Applied Physics Letters*, 96(7):7–10, 2010. doi: 10.1063/1.3323093.

[130] H. K. Pulker. Stress, Adherence, Hardness, and Density of Optical Thin Films. *Optical Thin Films*, 0325:84–92, 1982. doi: 10.1117/12.933290.

[131] L. Qian, M. Li, Z. Zhou, H. Yang, and X. Shi. Comparison of nano-indentation hardness to microhardness. *Surface & Coatings Technology*, 195 (2-3):264–271, 2004. doi: 10.1016/j.surfcoat.2004.07.108.

[132] M. Raza, D. Cornil, J. Cornil, S. Lucas, R. Snyders, and S. Konstantinidis. Oxygen vacancy stabilized zirconia (OVSZ); a joint experimental and theoretical study. *Scripta Materialia*, 124:26–29, 2016. doi: 10.1016/j.scriptamat.2016.06.025.

[133] N. Reddy, P. Bera, V. R. Reddy, N. Sridhara, A. Dey, C. Anandan, and A. K. Sharma. XPS study of sputtered alumina thin films. *Ceramics International*, 40:11099–11107, 2014. doi: 10.1016/j.ceramint.2014.03.133.

[134] R. F. Reilman, A. Msezane, and S. T. Manson. Relative intensities in photoelectron-spectroscopy of atoms and molecules. *Journal of Electron Spectroscopy and Related Phenomena*, 8(5):389–394, 1976. doi: 10.1016/0368-2048(76)80025-4.

[135] M. Renninger. "Umweganregung", eine bisher unbeachtete Wechselwirkungserscheinung bei Raumgitterinterferenzen. *Zeitschrift für Physik*, 106 (3-4):141–176, 1937. doi: 10.1007/BF01340315.

[136] J. Rosén, E. Widenkvist, K. Larsson, U. Kreissig, S. Mráz, C.s Martinez, D. Music, and J. M. Schneider. Reducing the impurity incorporation from residual gas by ion bombardment during high vacuum magnetron sputtering. *Applied Physics Letters*, 88(19):191905, 2006. doi: 10.1063/1.2193044.

[137] E. Rossmanith. Approximate calculation of multiple-diffraction patterns based on Renninger's kinematical 'simplest approach'. *Journal of Applied Crystallography*, 33(3 II):921–927, 2000. doi: 10.1107/S0021889800002739.

[138] C. M. Rost, E. Sachet, T. Borman, A. Moballegh, E. C. Dickey, D. Hou, J. L. Jones, S. Curtarolo, and J. P. Maria. Entropy-stabilized oxides. *Nature Communications*, 6:1–8, 2015. doi: 10.1038/ncomms9485.

[139] I. Safi. Recent aspects concerning DC reactive magnetron sputtering of thin films: a review. *Surface & Coatings Technology*, 127(2-3):203–218, 2000. doi: 10.1016/S0257-8972(00)00566-1.

[140] M. Scherer and P. Wirz. Reactive high rate d.c. sputtering of oxides. *Thin Solid Films*, 119(2):203–209, 1984. doi: 10.1016/0040-6090(84)90535-2.

[141] P Scherrer. Bestimmung der Grösse und der inneren Struktur von Kolloidteilchen mittels Röntgenstrahlen. *Nachrichten von der Gesellschaft der Wissenschaften zu Göttingen, Mathematisch-Physikalische Klasse*, pages 98–100, 1918. doi: 10.1007/978-3-662-33915-2.

[142] S. Schiller, U. Heisig, K. Steinfelder, J. Strümpfel, R. Voigt, R. Fendler, and G. Teschner. On the investigation of d.c. plasmatron discharges by optical emission spectrometry. *Thin Solid Films*, 96(3):235–240, 1982. doi: 10.1016/0040-6090(82)90247-4.

[143] S. Schmauder, M. Meyer, and H. F. Fischmeister. Correlation Between Dundurs ' Parameters and Elastic Constants. *Zeitschrift für Metallkunde*, 83(1): 524–528, 1992.

[144] J. Schulte and G. Sobe. Magnetron sputtering of aluminium using oxygen or nitrogen as reactive gas. *Thin Solid Films*, 324(1-2):19–24, 1998. doi: 10.1016/S0040-6090(97)01197-8.

[145] H. Schulz and K. H. Thiemann. Crystal structure refinement of AlN and GaN. *Solid State Communications*, 23(11):815–819, 1977. doi: 10.1016/0038-1098(77)90959-0.

[146] J. H. Scofield. Hartree-Slater subshell photoionization cross-sections at 1254 and 1487 eV. *Journal of Electron Spectroscopy and Related Phenomena*, 8 (2):129–137, 1976. doi: 10.1016/0368-2048(76)80015-1.

[147] M. P. Seah and W. A. Dench. Quantitative electron spectroscopy of surfaces: A standard data base for electron inelastic mean free paths in solids. *Surface and Interface Analysis*, 1(1):2–11, 1979. doi: 10.1002/sia.740010103.

[148] B. W. Sheldon, A. Rajamani, A. Bhandari, E. Chason, S. K. Hong, and R. Beresford. Competition between tensile and compressive stress mechanisms during Volmer-Weber growth of aluminum nitride films. *Journal of Applied Physics*, 98(4):043509, 2005. doi: 10.1063/1.1994944.

[149] V. B. Shenoy, A. F. Schwartzman, and L. B. Freund. Crack patterns in brittle thin films. *International Journal of Fracture*, 103(1):1–17, 2000. doi: 10.1023/A:1007673320058.

[150] A. B. Sinani, N. K. Dynkin, L. A. Lytvinov, P. V. Konevsky, and E. P. Andreev. Sapphire hardness in different crystallographic directions. *Bulletin of the Russian Academy of Sciences: Physics*, 73(10):1380–1382, 2009. doi: 10.3103/S1062873809100177.

[151] G. A. Slack. Nonmetallic crystals with high thermal conductivity. *Journal of Physics and Chemistry of Solids*, 34(2):321–335, 1973. doi: 10.1016/0022-3697(73)90092-9.

[152] Glen A. Slack and S. F. Bartram. Thermal expansion of some diamondlike crystals. *Journal of Applied Physics*, 46:89–98, 1975. doi: 10.1063/1.321373.

[153] Glen A. Slack, R. A. Tanzilli, R. O. Pohl, and J. W. Vandersande. The intrinsic thermal conductivity of AIN. *Journal of Physics and Chemistry of Solids*, 48(7), 1987. doi: 10.1016/0022-3697(87)90153-3.

[154] G. V. Soares, K. P. Bastos, R. P. Pezzi, L. Miotti, C. Driemeier, I. J R Baumvol, C. Hinkle, and G. Lucovsky. Nitrogen bonding, stability, and transport in AION films on Si. *Applied Physics Letters*, 84(24):4992–4994, 2004. doi: 10.1063/1.1763230.

[155] G. Soto, W. De La Cruz, and M. H. Farías. XPS, AES, and EELS characterization of nitrogen-containing thin films. *Journal of Electron Spectroscopy and Related Phenomena*, 135(1):27–39, 2004. doi: 10.1016/j.elspec.2003.12.004.

[156] A. G. Spencer, R. P. Howson, and R. W. Lewin. Pressure stability in reactive magnetron sputtering. *Thin Solid Films*, 158(1):141–149, 1988. doi: 10.1016/0040-6090(88)90310-0.

[157] W. D. Sproul. High-rate reactive DC magnetron sputtering of oxide and nitride superlattice coatings. *Vacuum*, 51(4):641–646, 1998. doi: 10.1016/S0042-207X(98)00265-6.

[158] W. D. Sproul and J. R. Tomashek. U.S. Patent 4,428,811: Rapid Rate Reactive Sputtering of a Group IVB Metal, 1984.

[159] W. D. Sproul, D. J. Christie, and D. C. Carter. Control of reactive sputtering processes. *Thin Solid Films*, 491(1-2):1–17, 2005. doi: 10.1016/j.tsf.2005.05.022.

[160] C. Stampfl and C. G. Van de Walle. Theoretical investigation of native defects, impurities, and complexes in aluminum nitride. *Physical Review B - Condensed Matter and Materials Physics*, 65(15):1552121–15521210, 2002. doi: 10.1103/PhysRevB.65.155212.

[161] N. C. Stephenson and R. S. Roth. Structural systematics in the binary system Ta_2O_5–WO_3. V. The structure of the low-temperature form of tantalum oxide L-Ta_2O_5. *Acta Crystallographica Section B, Structural Crystallography and Crystal Chemistry*, 27(5):1037–1044, 1971. doi: 10.1107/S056774087100342X.

[162] P. Tabary and C. Servant. Thermodynamic Reassessment of the AlN-Al_2O_3 System. *Calphad: Computer Coupling of Phase Diagrams and Thermochemistry*, 22(2), 1998.

[163] P. Tabary and C. Servant. Crystalline and microstructure study of the AlN-Al_2O_3 section in the Al-N-O system. II. ϕ - and δ-AlON spinel phases.

Journal of Applied Crystallography, 32(2):253–272, 1999. doi: 10.1107/S0021889898012497.

[164] P. Tabary and C. Servant. Crystalline and microstructure study of the AlN–Al_2O_3 section in the Al–N–O system. I. Polytypes and γ-AlON spinel phase. *Journal of Applied Crystallography*, 32(2):241–252, 1999. doi: 10.1107/S0021889898012485.

[165] Y. Taniyasu, M. Kasu, and N. Kobayashi. Lattice parameters of wurtzite $Al_{1-x}Si_xN$ ternary alloys. *Applied Physics Letters*, 79(26):4351–4353, 2001. doi: 10.1063/1.1428768.

[166] J. A. Thornton. Influence of apparatus geometry and deposition conditions on the structure and topography of thick sputtered coatings. *Journal of Vacuum Science & Technology*, 11(4):666–670, 1974. doi: 10.1116/1.1312732.

[167] J. A. Thornton. The microstructure of sputter-deposited coatings. *Journal of Vacuum Science & Technology A*, 4(6):3059–3065, 1986. doi: 10.1116/1.573628.

[168] M. D. Thouless. Crack spacing in brittle films on elastic substrates. *Journal of the American Ceramic Society*, 73(7):2144–2146, 1990. doi: 10.1016/0956-7151(92)90429-I.

[169] M. D. Thouless. Cracking of Brittle Films on Elastic Substrates. *Acta Metallurgica et Materialia*, 40(6):1287–1292, 1992. doi: 10.1016/0956-7151(92)90429-I.

[170] H. Tillborg, A. Nilsson, B. Hernnäs, N. Mårtensson, and R. E. Palmer. X-ray and UV photoemission studies of mono-, bi- and multilayers of physisorbed molecules: O_2 and N_2 on graphite. *Surface Science*, 295(1-2):1–12, 1993. doi: 10.1016/0039-6028(93)90180-R.

[171] Y.S. Touloukian, R.W. Powell, C.Y. Ho, and P.G. Klemens. *Thermophysical Properties of Matter - The TPRC Data Series. Volume 1: Thermal Conductivity*. IFI/Plenum, New York, 1970.

[172] M. Trant, M. Fischer, K. Thorwarth, S. Gauter, J. Patscheider, and H. J. Hug. Tunable ion flux density and its impact on AlN thin films deposited in a confocal DC magnetron sputtering system. *Surface & Coatings Technology*, 348:159–167, 2018. doi: 10.1016/j.surfcoat.2018.04.091.

[173] M. H. Tsai and J. W. Yeh. High-entropy alloys: A critical review. *Materials Research Letters*, 2(3):107–123, 2014. doi: 10.1080/21663831.2014.912690.

[174] N. Tsukamoto, N. Oka, and Y. Shigesato. In-situ analyses on the reactive sputtering process to deposit Al-doped ZnO films using an Al-Zn alloy target. *Thin Solid Films*, 520(10):3751–3754, 2012. doi: 10.1016/j.tsf.2011.08.031.

[175] J. Turkevich, G. Garton, and P. C. Stevenson. The color of colloidal gold. *Journal of Colloid Science*, 9:26–35, 1954. doi: 10.1016/0095-8522(54)90070-7.

[176] S. Veprek and M. G. J. Veprek-Heijman. The formation and role of interfaces in superhard nc-MenN/a-Si_3N_4 nanocomposites. *Surface & Coatings Technology*, 201(13):6064–6070, 2007. doi: 10.1016/j.surfcoat.2006.08.112.

[177] S. Veprek, M. G. J. Veprek-Heijman, P. Karvankova, and J. Prochazka. Different approaches to superhard coatings and nanocomposites. *Thin Solid Films*, 476(1):1–29, 2005. doi: 10.1016/j.tsf.2004.10.053.

[178] J. C. Vickerman and J. S. Gilmore. *Surface Analysis– The Principal Techniques*. John Wiley & Sons, Ltd., Chichester, UK, 2nd edition, 2009. ISBN 978-0-470-01763-0.

[179] A. A. Volinsky, N. R. Moody, and D. C. Meyer. Stress-induced periodic fracture patterns in thin films. *International Congress on Fracture*, pages 1–5, 2005.

[180] P. W. Wang, J. Ch. Hsu, Y. H. Lin, and H. L. Chen. Nitrogen bonding in aluminum oxynitride films. *Applied Surface Science*, 256(13):4211–4214, 2010. doi: 10.1016/j.apsusc.2010.02.004.

[181] J. F. Watts and J. Wolstenholme. *An Introduction to Surface Analysis by XPS and AES*. John Wiley & Sons, Ltd., Chichester, UK, 2003. ISBN 978-0-470-84713-1.

[182] W. D. Westwood. *Sputter Deposition*. AVS, New York, USA, 2003. ISBN 0-7354-0105-5.

[183] K. W. Whitten, R. E. Davis, L. M. Peck, and G. G. Stanley. *Chemistry*. Thomson Brooks/Cole, Belmont, USA, 8th edition, 2007. ISBN 0-495-01448-6.

[184] J. H. Wilson, J. D. Todd, and A. P. Sutton. Modelling of silicon surfaces: a comparative study. *Journal of Physics: Condensed Matter*, 2(51):10259–10288, 1990. ISSN 09538984. doi: 10.1088/0953-8984/2/51/004.

[185] H. Windischmann. Intrinsic Stress in Sputter-Deposited Thin Films. *Critical Reviews in Solid State and Materials Sciences*, 17(6):547–596, 1992. doi: 10.1080/10408439208244586.

[186] B. Window and N. Savvides. Charged particle fluxes from planar magnetron sputtering sources. *Journal of Vacuum Science & Technology A*, 4(2):196–202, 1986. doi: 10.1116/1.573470.

[187] W. Xiao and X. Jiang. Optical and mechanical properties of nanocrystalline aluminum oxynitride films prepared by electron cyclotron resonance plasma enhanced chemical vapor deposition. *Journal of Crystal Growth*, 264(1-3): 165–171, 2004. doi: 10.1016/j.jcrysgro.2004.01.019.

[188] G. Yamaguchi and H. Yanagida. Study on the Reductive Spinel—A New Spinel Formula AlN–Al_2O_3 instead of the Previous One Al_3O_4. *Bulletin of the Chemical Society of Japan*, 32:1264–1265, 1959. doi: 10.1246/bcsj.32.1264.

[189] W. M. Yim and R. J. Paff. Thermal expansion of AlN, sapphire, and silicon. *Journal of Applied Physics*, 45(3):1456–1457, 1974. doi: 10.1063/1.1663432.

[190] P. Zaumseil. High-resolution characterization of the forbidden Si 200 and Si 222 reflections. *Journal of Applied Crystallography*, 48:528–532, 2015. ISSN 16005767. doi: 10.1107/S1600576715004732.

[191] S. Zhang and W. Zhu. TiN coating of tool steels: a review. *Journal of Materials Processing Technology*, 39(1-2):165–177, 1993. doi: 10.1016/0924-0136(93)90016-Y.

[192] S. Zhang, H. L. Wang, S.-E. Ong, D. Sun, and X. L. Bui. Hard yet Tough Nanocomposite Coatings – Present Status and Future Trends. *Plasma Processes and Polymers*, 4(3):219–228, 2007. doi: 10.1002/ppap.200600179.

Curriculum Vitae

Name:	Maria Ruth Fischer
Date and place of birth:	May 19, 1987
Nationality:	Swiss

1994 - 1999	**Primary school**
	Primarschule Mägenwil, CH
1999 - 2003	**Secondary school**
	Bezirksschule Mellingen, CH
2003 - 2007	**High school**
	Neue Kantosschule Aarau, CH
2007 - 2008	**Office assistant**
	Fischer Bettwaren AG, Au ZH, CH
	Alpiq - Hydraulic Production, Olten, CH
2008 - 2012	**Bachelor in Chemistry (minor Biochemistry)**
	University of Zurich (UZH), CH
2011 - 2013	**Master in Chemistry (minor Physics)**
	University of Zurich (UZH), CH
2012 - 2013	**Master thesis**
	Paul Scherrer Institute (PSI), Villigen, CH
2014 - now	**PhD thesis**
	Empa, Swiss Federal Laboratories
	for Materials Science and Technology, Dübendorf, CH

List of scientific contributions

Oral communications

Challenges in Depositing AlO_xN_y Films by Reactive Direct Current Magnetron Sputtering; Maria Fischer, Mathis Trant, Kerstin Thorwarth, Hans J. Hug, Jörg Patscheider; *79. Jahrestagung der Deutschen Physikalischen Gesellschaft (DPG), Berlin DE*, **2015**.

TeQuAlON: Sputter deposited thin films of an up-and-coming material system; Maria Fischer, Mathis Trant, Kerstin Thorwarth, Hans J. Hug, Jörg Patscheider; *Empa Lab203 visit, Dübendorf CH*, **2015**.

Aluminum oxynitride in TeQuAlON: Sputter deposited thin films of an up-and-coming material system; Maria Fischer, Mathis Trant, Kerstin Thorwarth, Hans J. Hug, Jörg Patscheider; *Invited talk at the Laboratory for Ion Beam Physics (LIP) at the Swiss Federal Institute of Technology, Zürich (ETHZ), CH*, **2016**.

Aluminum Oxynitride Thin Films by Reactive DC Magnetron Sputter Depostition; Maria Fischer, Mathis Trant, Kerstin Thorwarth, Hans J. Hug, Jörg Patscheider; *43^{rd} International Conference on Metallurgical Coatings and Thin Films (ICMCTF), San Diego CA, USA*, **2016**.

Ternary and Quaternary Aluminum Oxynitride Thin Films by Reactive DC Magnetron Sputter Deposition; Maria Fischer, Mathis Trant, Kerstin Thorwarth, Hans J. Hug, Jörg Patscheider; *Empa PhD Students' Symposium, Dübendorf CH*, **2016**.

Vacancies as Stabilizers in Ternary and Quaternary Thin Films of Al, Si, O and N; Maria Fischer, Daniele Scopece, Carlo A. Pignedoli, Mathis Trant, Kerstin Thorwarth, Hans J. Hug, Daniele Passerone, Jörg Patscheider; *44^{th} ICMCTF, San Diego CA, USA*, **2017**.

Vacancies & Thermodynamics in Al-O/Si-N; Maria Fischer, Daniele Scopece, Carlo A. Pignedoli, Mathis Trant, Kerstin Thorwarth, Daniele Passerone, Hans J. Hug; *Empa Lab203 visit, Dübendorf CH*, **2017**.

Vacancies & Thermodynamics in Al-O/Si-N; Maria Fischer, Daniele Scopece, Carlo A. Pignedoli, Mathis Trant, Kerstin Thorwarth, Daniele Passerone, Hans J. Hug; *16th International Conference on Reactive Sputter Deposition, Pilsen, CZ*, **2017**.

Vacancies & Thermodynamics in Al-O/Si-N; Maria Fischer, Daniele Scopece, Carlo A. Pignedoli, Z. Balogh-Michels, Mathis Trant, Kerstin Thorwarth, Daniele Passerone, Hans J. Hug; *PhD Seminars in Empa Department ´Materials meet life´, St. Gallen, CH*, **2018**.

Vacancies & Thermodynamics in Al-O/Si-N; Maria Fischer, Daniele Scopece, Carlo A. Pignedoli, Mathis Trant, Kerstin Thorwarth, Daniele Passerone, Hans J. Hug; *45th ICMCTF, San Diego CA, USA*, **2018**.

Vacancies & Thermodynamics in Al-O/Si-N; Maria Fischer, Daniele Scopece, Carlo A. Pignedoli, Mathis Trant, Kerstin Thorwarth, Daniele Passerone, Hans J. Hug; *16th International Conference on Plasma Surface Engineering (PSE), Garmisch-Partenkirchen DE*, **2018**.

Posters

Aluminum Oxynitride (Al-O-N) Thin Films by Reactive Closed Field Direct Current Magnetron Sputtering (R-CFDC-MS); Maria Fischer, Mathis Trant, Kerstin Thorwarth, Hans J. Hug, Jörg Patscheider; *78th IUVSTA Workshop, Braga PT*, **2015**.

Aluminum Oxynitride (Al-O-N) Thin Films by Reactive Closed Field Direct Current Magnetron Sputtering (R-CFDC-MS); Maria Fischer, Mathis Trant, Kerstin Thorwarth, Hans J. Hug, Jörg Patscheider; *Empa PhD Students' Symposium, Dübendorf CH*, **2015**.

Aluminum Oxynitride Thin Films Deposited by Reactive Closed Field Magnetron Sputtering; Maria Fischer, Mathis Trant, Kerstin Thorwarth, Hans J. Hug, Jörg Patscheider; *32nd Swiss Working Group for Surface and Interface*

Science (SAOG) Meeting, Freiburg CH, **2016**.

Properties Evolution in Al-O-N Thin Films; Maria Fischer, Mathis Trant, Kerstin Thorwarth, Hans J. Hug, Jörg Patscheider; *15th PSE, Garmisch-Partenkirchen DE*, **2016**.

Vacancies in Al-Si/O-N; Maria Fischer, Daniele Scopece, Carlo A. Pignedoli, Mathis Trant, Kerstin Thorwarth, Daniele Passerone, Hans J. Hug; *Competence Centre for Materials Science and Technology, Materials Day (CCMX-Marvel) / Annual Meeting, Dübendorf CH*, **2017**.

Vacancies in Al-Si/O-N Crystallites; Maria Fischer, Daniele Scopece, Carlo A. Pignedoli, Z. Balogh-Michels, Mathis Trant, Kerstin Thorwarth, Daniele Passerone, Hans J. Hug; *45th ICMCTF, San Diego CA, USA*, **2018**.

Publications

Polysiloxane Nanotubes; Ana Stojanovic, Sandro Olveira, Maria Fischer, Stefan Seeger; *Chemistry of Materials, 25, 2787-2792*, **2013**.

A novel methylation derivatization method for δ^{18}O analysis of individual carbohydrates by gas chromatography/pyrolysis– isotope ratio mass spectrometry; Marco M. Lehmann, Maria Fischer, Jan Blees, Michael Zech, Rolf T. W. Siegwolf, Matthias Saurer; *Rapid Communications in Mass Spectrometry, 30, 221-229*, **2016**.

Tunable ion flux density and its impact on AlN thin films deposited in a confocal DC magnetron sputtering system; Mathis Trant, Maria Fischer, Kerstin Thorwarth, S. Gauter, Jörg Patscheider, Hans Josef Hug; *Surface & Coatings Technology, 348, 159-167*, **2018**.

A setup for arc-free reactive DC sputter deposition of Al-O-N; Maria Fischer, Mathis Trant, Kerstin Thorwarth, Jörg Patscheider, Hans Josef Hug; *Surface & Coatings Technology, 362, 220-224*, **2019**.

Understanding the microstructural evolution and mechanical properties of transparent Al-(Si-)(O-)N films; Maria Fischer, Mathis Trant, Kerstin Thorwarth, Rowena Crockett, Jörg Patscheider, Hans Josef Hug; submitted to *Surface & Technology of Advanced Materials*, **2019**.

Acknowledgments

Just as important as the topic and the experiments one works on during a PhD thesis are the people around. It is their simple presence, their infectious enthusiasm and their confirming support that form the environment to unfold ideas into projects and transform them into scientific achievements.

Cordial thanks to everybody around me during the time of my thesis! All my coworkers of Lab203, I'd like to thank for the chats, the laughter and the RTCs we shared in good as in harder times. Those were encouraging when work went well, and they helped to detach and contemplate problems with rested eyes when things got tough. Heartfelt thanks also to all colleagues of other Empa labs, departments and sites. It was a pleasure to meet you, be it for work or personal!

Special thanks go to Prof. Dr. Hans Josef Hug, supervisor of this PhD thesis. Your fascination for science is catching! Thanks for the numerous scientific discussions, which amplified my insight into physics a lot. You invested much time and energy in correcting and improving this thesis, publications and presentations. Thanks to your approval and contributions, I had plenty of opportunities to take part in conferences and take our work out into the world. You took over and led our group on when gaps came up, and you keep supporting everybody in our lab until their projects are accomplished. Thank you for all of that!

Special thanks go as well to Dr. Rowena Crockett, who supervised the finalization of this project. From one day to the next, you took on the work of finishing this thesis, reading and correcting a myriad of pages in no time and with an admirable easiness. Your support was so crucial! The improvements your suggestions brought were huge, and discussing and working with you was great fun. You ac-

celerated the completion of this project incredibly, and without you, I'd probably still be in the middle of things. Thank you so much for helping me out!

Special thanks go to Dr. Kerstin Thorwarth, who supervised a considerable part of this project. Your scientific as well as your personal backing were of great support. Your vast knowledge and experience in all aspects of our field - in the lab, in writing and in the network of people - were essential. Thanks for taking a lot of time in reading and improving many texts and contributing to many projects. And thank you for the moral support and the comfort you provided to everybody, wherever and whenever needed!

Cordial thanks go to Prof. Dr. Ernst Meyer, co-examiner of this thesis. I am very grateful that you agreed to take on this assignment, even though this was on rather short notice, and the topic of this project is rather far from your research field. Thank you for this flexibility!

Many thanks also go to Prof. Dr. Martino Poggio, who immediately agreed to preside my defense.

Many thanks go to Dr. Jörg Patscheider for initiating the TeQuAlON project and supervising it in the first half. Your broad knowledge on whatever this world bears in mystery was enriching! It was great to share the chemical point of view on material science tasks ahead. You were always and immediately helping with words and deeds whenever needed. Thank you for all the freedom and trust you gave us for our work, and for supporting us in participating in many events within the scientific community.

Cordial thanks to Dr. Max Döbeli and the entire team at IBP for the innumerable measurements done for us. Thank you for the insight you gave me into your facilities and your enormous knowledge in the field of RBS/ERDA, and for letting me participate in evaluations. Data discussions with you belong to the most precious hours I had during my PhD time. Thank you for the x-axis in almost every graph in this thesis!

Likewise I thank Dr. Erwin Hack from Lab405 for countless ellipsometric measurements and their sophisticated evaluation. You resumed and repeated those with never-ending patience, and you did not get tired of explaining the complex mathematical theory behind it to a clueless chemist. Be it in German or Italian! Without your expertise, no ellipsometric result - and they were crucial! - would have made it into this thesis.

Cordial thanks go to Prof. Dr. Jochen Schneider, Prof. Dr.Christian Mitterer and all their students and coworkers, for the enriching meetings, the organization of those and for accommodating us during all of them.

Special thanks go to my office mates, whom I spent hours and hours with over these years of my PhD. Thank you, (very-soon-to-be Dr.) Mathis Trant, for your ever supporting and relaxed composure. I was as lucky as I could be that you were working on the same project! Thanks to Dr. Johannes Schwenk, for your infinite fascination and ingenious experience you shared. Thank you, (soon-to-be Dr.) Aarati Chacko, for your caring, sensitive ways to deal with everybody and everything. Chats with you were endlessly up-cheering! Dr. Clara Barker, thank you for the diversity and color (and ponies) you brought into our everyday life. Thanks go to Dr. Oguz Yildirim, ever calm and balanced, and at the same time lots of fun to talk to and always supportive!

Many people in our and other Empa Labs were more than just colleagues working alongside. I relied on their help and support daily. Thank you, Dr. Claudia Cancellieri, for your support and sharing your vast knowledge in XRD with me. While fixing our dear, delicate D8 often was laborious, it was great fun doing it with you! Thank you, Dr. Ueli Müller, for your infinite support in the labs, with the XPS, for the stunning scientific discussions, for being firm as a rock no matter how wild things go, and for your Swissness. The Ueli-Grössenordnung will forever stay a universal unit to me! Thank you, Saśa Vranjkovic, for your numerous crazy constructions that turned the seemingly impossible into reality! You assisted us in hours and hours of lab work and found the most creative and sound solutions

for every last single thing. Thanks to Günther Hobi, for your Bündner originality and your unlimited Swiss exactitude in everything you touch. I learned so many tricks and electrical facts from you, and insulating band will never be anything but decoration to me again!

Thanks go to Dr. Daniele Scopece, Dr. Carlo Pignedoli and Dr. Daniele Passerone for the calculations and interpretations, and for the patience and endurance in carrying projects through. Thanks to Dr. Zoltán Balogh-Michels, Prof. Dr. Antonia Neels and Prof. Dr. Alex Dommann for the specialized measurements that boosted the basic results we had until then, and for sharing profound experience in the field of XRD. Thank you, Arndt Remhof, for the many HT*is*XRD measurements we did together and the fascinating data discussions. Thanks go to Dr. Yucheng Zhang for introducing me to the art of TEM sample preparation and the following imaging, and to Michael Stiefel for SEM imaging and for providing his knowledge that made many of our images a lot better. Thank you, Hans Jürgen Schindler, Laura Conti and Lukas Rotach, for providing your ovens, equipment and assistance to bring our samples up to insane temperatures. Many thanks go to Dr. James Best and Dr. Gaurav Mohanty, who explained and helped so much in plenty of nanoindentation sessions in Thun. Thanks go to Dr. Thomas Geiger for the optical profilometry measurements and their processing.

Finally, but very importantly, I thank my family, my partner and my friends with all my heart. You gave me the freedom and the possibility to move in any direction I chose to go, without ever questioning or obstructing any decision. Your love and endorsement have always been unconditional. That was the most precious gift you could give me for my life.

Thank you, all of you, for the time we shared!